



**HAL**  
open science

# A flexible coil array for high resolution magnetic resonance imaging at 7 Tesla

Roberta Kriegl

► **To cite this version:**

Roberta Kriegl. A flexible coil array for high resolution magnetic resonance imaging at 7 Tesla. Other [cond-mat.other]. Université Paris Sud - Paris XI; Medizinische Universität Wien, 2014. English. NNT : 2014PA112425 . tel-01127308

**HAL Id: tel-01127308**

**<https://theses.hal.science/tel-01127308>**

Submitted on 7 Mar 2015

**HAL** is a multi-disciplinary open access archive for the deposit and dissemination of scientific research documents, whether they are published or not. The documents may come from teaching and research institutions in France or abroad, or from public or private research centers.

L'archive ouverte pluridisciplinaire **HAL**, est destinée au dépôt et à la diffusion de documents scientifiques de niveau recherche, publiés ou non, émanant des établissements d'enseignement et de recherche français ou étrangers, des laboratoires publics ou privés.



Comprendre le monde,  
construire l'avenir®



UNIVERSITE PARIS-SUD

ÉCOLE DOCTORALE

Sciences et Technologie de l'Information, des Télécommunications  
et des Systèmes

Laboratoire d'Imagerie par Résonance Magnétique Médicale et Multi-Modalités (IR4M)

*DISCIPLINE : Physique*

THÈSE DE DOCTORAT

Soutenance prévue le 17/12/2014

par

**Roberta KRIEGL**

**A flexible coil array for high resolution magnetic  
resonance imaging at 7 Tesla**

**Composition du jury :**

*Directeur de thèse :*

*Co-directeur de thèse :*

*Examineurs :*

Jean-Christophe Ginefri

Ewald MOSER

Wolfgang DREXLER

Elmar LAISTLER

HDR, IR4M, Université Paris Sud

Professeur, CMPBME, Université médicale de Vienne

Professeur, CMPBME, Université médicale de Vienne

Chercheur, CMPBME, Université médicale de Vienne



# Abstract

Magnetic resonance imaging (MRI), among other imaging techniques, has become a major backbone of modern medical diagnostics. MRI enables the non-invasive combined, identification of anatomical structures, functional and chemical properties, especially in soft tissues. Nonetheless, applications requiring very high spatial and/or temporal resolution are often limited by the available signal-to-noise ratio (SNR) in MR experiments. Since first clinical applications, image quality in MRI has been constantly improved by applying one or several of the following strategies: increasing the static magnetic field strength, improvement of the radiofrequency (RF) detection system, development of specialized acquisition sequences and optimization of image reconstruction techniques.

This work is concerned with the development of highly sensitive RF detection systems for biomedical ultra-high field MRI. In particular, auto-resonant RF coils based on transmission line technology are investigated. These resonators may be fabricated on flexible substrate which enables form-fitting of the RF detector to the target anatomy, leading to a significant SNR gain.

The main objective of this work is the development of a flexible RF coil array for high-resolution MRI on a human whole-body 7 T MR scanner. With coil arrays, the intrinsically high SNR of small surface coils may be exploited for an extended field of view. Further, parallel imaging techniques are accessible with RF array technology, allowing acceleration of the image acquisition. Secondly, in this PhD project a novel design for transmission line resonators is developed, that brings an additional degree of freedom in geometric design and enables the fabrication of large multi-turn resonators for high field MR applications.

This thesis describes the development, successful implementation and evaluation of novel, mechanically flexible RF devices by analytical and 3D electromagnetic simulations, in bench measurements and in MRI experiments.

# Résumé

L'imagerie par résonance magnétique (IRM) est un outil d'investigation majeur donnant accès de manière non invasive à des nombreuses informations quantitatives et fonctionnelles. La qualité des images obtenues (rapport-signal-sur-bruit, RSB) est cependant limitée dans certaines applications nécessitant des résolutions spatiales et/ou temporelles poussées. Afin d'améliorer la sensibilité de détection des équipements d'IRM, diverses orientations peuvent être suivies telles qu'augmenter l'intensité du champ magnétique des imageurs, améliorer les performances des systèmes de détection radiofréquence (RF), ou encore développer des séquences d'acquisition et des techniques de reconstruction d'images plus efficaces.

La thématique globale dans laquelle s'inscrit cette thèse concerne le développement des systèmes de détection RF à haute sensibilité pour l'IRM à haut champ chez l'homme. En particulier, des antennes auto-résonantes basées sur le principe des lignes de transmission sont utilisées parce qu'elles peuvent être réalisées sur substrat souple. Cette adaptabilité géométrique du résonateur permet d'ajuster précisément sa forme aux spécificités morphologiques de la zone anatomique observée, et ainsi d'augmenter le RSB.

La première visée technologique de ce projet concerne le développement, de la conception jusqu'à la mise en œuvre dans un appareil 7 T corps entier, d'un système de détection RF flexible à haute sensibilité, utilisant des antennes miniatures associées en réseau. L'utilisation d'un réseau d'antennes miniatures permet d'obtenir des images sur un champ de vue élargi tout en conservant la haute sensibilité inhérente à chaque antenne miniature. De plus, la technologie de l'imagerie parallèle devient accessible, ce qui permet d'accélérer l'acquisition des images. De surcroît, un nouveau schéma de résonateur de ligne transmission avec un degré de liberté supplémentaire est introduit, ce qui permet de réaliser de grands résonateurs multi-tours pour l'IRM à haut champ.

Cette thèse décrit le développement, la mise en œuvre et l'évaluation des nouveaux systèmes de détection RF au moyen de simulations analytiques et numériques, et des études expérimentales.

# Kurzfassung

Die Magnetresonanztomographie (MRT) zählt zu den wichtigsten diagnostisch-bildgebenden Verfahren und ermöglicht eine nicht-invasive Erfassung vielfältiger quantitativer und funktioneller Informationen aus dem Inneren des menschlichen Körpers. Die Bildqualität wird dabei vom erreichbaren Signal-zu-Rausch-Verhältnis (SNR) bestimmt; insbesondere bei Anwendungen, die hohe räumliche und/oder zeitliche Auflösung verlangen, ist eine hohe Sensitivität des Messprozesses erforderlich. Verschiedene Möglichkeiten zur Verbesserung des SNR sind durch die Erhöhung des statischen Magnetfelds, die Verbesserung der Sensitivität von verwendeten Hochfrequenz (HF)-Spulen und effizientere Pulssequenzen gegeben.

Diese Dissertation beschäftigt sich vorrangig mit der Entwicklung hochsensitiver HF Spulen für biomedizinische Hochfeld-MRT. Dabei kommen insbesondere autoresonante Spulen basierend auf dem Transmissionsleitungsprinzip (TL) zum Einsatz. Durch die Verwendung flexibler Substratmaterialien können diese Spulen optimal an die anatomische Form der zu untersuchenden Körperregion angepasst werden, um dadurch die Sensitivität zu verbessern.

Oberstes technologisches Ziel ist die Entwicklung eines flexiblen HF Spulenarrays, welches in einem 7 T Ganzkörper MR-Scanner eingesetzt werden kann. Die Kombination mehrerer Spulen zu einem Array erlaubt die Ausweitung des Sichtfeldes, während gleichzeitig die hohe Empfindlichkeit der einzelnen kleinen Spulenelemente bewahrt werden kann. Außerdem ermöglichen Spulenarrays den Einsatz von paralleler Bildgebung, wodurch die MR Messungen deutlich beschleunigt werden können. Darüber hinaus wird in dieser Dissertation ein neues Design für Spulen nach dem TL-Prinzip vorgestellt, welches durch einen zusätzlichen Freiheitsgrad erstmals die Entwicklung großer TL-Spulenelemente mit mehreren Windungen für hohe Magnetfeldstärken ermöglicht.

In dieser Dissertation werden die Entwicklung und Implementierung neuartiger HF Systeme beschrieben, sowie die Evaluierung ihrer Funktionsweise durch analytische und numerische Simulationen und durch Experimente im und außerhalb des MR Scanners.

# Acknowledgments

Many people have helped me along the way of studying for a PhD. I would like to thank the following in particular:

First and foremost I thank my supervisors Jean-Christophe Ginefri, Elmar Laistler and Ewald Moser for their scientific support and advice. Also, without their great administrative efforts, the joint PhD program between the Medical University of Vienna and Université Paris Sud, which was launched with the presented thesis, could not have been established.

I thank Luc Darrasse for welcoming me at IR4M and for his inspiring scientific comments, Albine Pinseel for providing some desperately needed insights in the French administration system, and my co-workers at IR4M, Marie Poirier-Quinot and Zhoujian Li for helpful discussions and interesting experiments. I thank all other members of IR4M for making my year in Paris unforgettable, especially Maya, Khaoula, Hong-Chen, Marion, George, Jean-Pierre, Xavier, Geneviève, and Ludovic.

I thank my colleagues at the RF lab in Vienna, Sigrun Goluch, André Kühne, Lucia Navarro de Lara, Jürgen Sieg, and Michael Pichler, without whom my understanding of RF coil engineering would be much less. Further, I acknowledge all other members of the MR Center in Vienna from the Physics and the Radiology department, who made work as well as coffee breaks pleasant and entertaining, but who are way too numerous to be mentioned without forgetting anybody.

Finally, I thank my parents, Marianne and Reinhart, who always supported me and encouraged me to take every chance live offers, and Albert for motivating/challenging me to pursue ambitious goals.

I acknowledge financial support from Université Paris Sud (Contrat doctoral, 2011-2014), the French/Austrian MAEE/OeAD project PHC/WTZ Amadée FR08/2013, and the Austrian BMWFJ FFG project Nr. 832107, “Research Studio for Ultra-High Field MR Applications”.

“Lifetime’s music, arriving all at once. Boundaries between noise and sound are conventions, I see now. All boundaries are conventions, national ones too. One may transcend any convention, if only one can first conceive of doing so.”

– from *Cloud Atlas*  
by David Mitchell



# Table of Contents

Abstract.....	3
Résumé.....	4
Kurzfassung .....	5
Acknowledgments.....	6
Introduction.....	13
Thesis Outline .....	15
Chapter I Theoretical Background.....	16
I.1. Nuclear Magnetic Resonance .....	17
I.1.1. Spins and magnetic moments.....	17
I.1.2. Nuclear polarization.....	19
I.1.3. Larmor precession.....	21
I.1.4. Relaxation phenomena.....	23
I.2. Principles of magnetic resonance imaging .....	27
I.2.1. Spin echo and gradient echo .....	27
I.2.2. Localization of signals .....	29
I.2.3. Slice selection .....	29
I.2.4. Frequency encoding.....	30
I.2.5. Phase encoding.....	31
I.2.6. k-space .....	32
I.2.7. Parallel imaging techniques .....	34
I.3. Signal and Noise in NMR experiments .....	36
I.3.1. The Reciprocity Principle .....	36
I.3.2. Noise mechanisms .....	37
I.3.3. Signal-to-noise ratio.....	39
Chapter II RF Coils and their Characterization.....	41
II.1. Basic principles.....	42
II.1.1. Resonant circuits.....	42
II.1.2. Transmit and receive field of an RF coil.....	43

II.1.3.	Specific absorption rate (SAR) .....	44
II.1.4.	High frequency effects .....	45
II.2.	NMR probe design .....	47
II.2.1.	Volume probes .....	47
II.2.2.	Surface coils.....	48
II.2.2.1.	Conventional surface coils.....	49
II.2.2.2.	Monolithic transmission line resonators.....	50
II.2.3.	Array probes.....	51
II.2.3.1.	Mutual decoupling in coil arrays .....	52
II.3.	Relating the RF probe to the MR scanner.....	54
II.3.1.	Power matching and noise matching .....	54
II.3.2.	Capacitive matching.....	55
II.3.3.	Inductive matching.....	56
II.3.4.	Baluns and common mode current blocking .....	59
II.3.5.	Receive-only probes.....	60
II.3.6.	Additional hardware.....	61
II.3.6.1.	The preamplifier .....	61
II.3.6.1.	Transmit/Receive switching .....	61
II.3.6.2.	Splitting the transmit power .....	62
II.4.	Numerical and analytical RF coil modeling .....	64
II.4.1.	Full-wave electromagnetic simulation.....	64
II.4.2.	Principles of FDTD.....	64
II.4.3.	Combining FDTD and circuit co-simulation .....	66
II.4.4.	Modeling of TLRs.....	68
II.4.4.1.	Analytical Model for TLRs .....	69
II.4.4.2.	FDTD simulation of TLRs .....	71
II.5.	Experimental characterization of RF coils.....	72
II.5.1.	Bench measurements .....	72
II.5.1.1.	Network analyzer.....	72
II.5.1.2.	S-Parameters .....	72
II.5.1.3.	Double-loop probe method.....	73
II.5.1.4.	Single-loop probe method .....	74
II.5.2.	MR Imaging Experiments.....	75

II.5.2.1.	MR scanners .....	75
II.5.2.2.	Imaging sequences.....	76
Chapter III	Development, Implementation and Evaluation of a Flexible TLR Array .....	78
III.1.	Abstract .....	79
III.2.	Introduction.....	80
III.3.	Methods.....	84
III.3.1.	Design and Simulation .....	84
III.3.1.1.	Novel Decoupling Technique for TLR Arrays .....	84
III.3.1.2.	Matching Networks .....	84
III.3.1.3.	Decoupling Performance .....	86
III.3.1.4.	Specific Absorption Rate.....	87
III.3.1.5.	Simulation Tools.....	87
III.3.2.	Hardware and Phantoms.....	88
III.3.3.	Bench Measurements .....	90
III.3.3.1.	Decoupling Performance.....	90
III.3.3.2.	Form-fitting .....	90
III.3.3.3.	Pickup Loop Noise Factor.....	90
III.3.3.4.	Influence of the Decoupling Annexes .....	91
III.3.4.	MRI Experiments .....	91
III.3.4.1.	Preparatory Measurements.....	91
III.3.4.2.	Noise Correlation and Parallel Imaging Performance.....	92
III.3.4.3.	High Resolution MRI.....	92
III.4.	Results.....	93
III.4.1.	Coil Geometries and Matching Setup .....	93
III.4.2.	Choice of the Array Design.....	95
III.4.3.	Specific Absorption Rate.....	97
III.4.4.	Performance of the Flexible TLR Array .....	98
III.5.	Discussion and Conclusions .....	102
Chapter IV	Additional information about the developed TLR array .....	106
IV.1.	Introduction.....	107

IV.2.	Preparatory study: Mutual inductance between TLRs .....	108
IV.2.1.	Analytical modeling .....	108
IV.2.2.	Bench measurements.....	109
IV.3.	Geometry of the individual array elements.....	113
IV.3.1.	Resonance frequency analysis.....	113
IV.3.2.	Noise contribution from the decoupling annexes.....	114
IV.4.	High-resolution MRI with the flexible array .....	115
IV.4.1.	MR imaging of a pepper fruit.....	115
IV.4.2.	MR imaging of a sheep knee.....	116
Chapter V	Other Advances with TLR Coils.....	118
V.1.	Introduction.....	119
V.2.	Alternative capacitive matching scheme .....	120
V.2.1.	Investigated matching networks .....	120
V.2.2.	Simulations .....	120
V.2.3.	Bench tests .....	122
V.3.	Active detuning for TLRs .....	123
V.3.1.	Matching and detuning circuit .....	123
V.3.2.	Experimental evaluation .....	124
V.4.	MTMG TLRs - Proof-of-principle at 4.7 T .....	126
V.4.1.	Multi-turn multi-gap TLR principle.....	126
V.4.2.	Analytical modeling.....	127
V.4.3.	Bench measurements .....	128
V.4.4.	MR imaging .....	128
V.5.	MTMG TLRs at 7 T.....	130
V.5.1.	Coil design .....	130
V.5.2.	Bench evaluation of MTMG TLRs at 7 T.....	131
V.5.3.	EM field simulation and $B_1$ mapping.....	132
Chapter VI	Discussion, Conclusions and Perspectives.....	135
VI.1.	Flexible TLR array.....	136
VI.1.1.	Summary .....	136

VI.1.2.	Ways to improve the developed TLR array.....	136
VI.1.3.	Potential applications for flexible TLR arrays .....	138
VI.2.	Multi-turn multi-gap TLRs for MRI.....	140
VI.3.	Conclusion .....	142
Appendix.....		143
Bibliography .....		154
List of Figures .....		164
List of Tables.....		167
Publication List .....		168
Curriculum Vitae.....		169

# Introduction

This PhD thesis emerges from an international collaboration between the Laboratoire d'Imagerie par Résonance Magnétique Médicale et Multi-Modalités (IR4M) at Université Paris Sud (France) and the Center for Medical Physics and Biomedical Engineering at the Medical University of Vienna (Austria). It concerns the development of novel RF hardware technology for high-resolution magnetic resonance imaging (MRI) at ultra-high static magnetic field strength.

The development of a prototype of a flexible RF coil array has been published as a full article in the journal *Magnetic Resonance in Medicine* (Kriegl, R., Ginefri, J.C., Poirier-Quinot, M., Darrasse, L., Goluch, S., Kuehne, A., Moser, E., Laistler, E., *Novel inductive decoupling technique for flexible transceiver arrays of monolithic transmission line resonators*. *Magn Reson Med*, 2014, doi: 10.1002/mrm.25260). Figures and text fragments of this paper are reproduced in this manuscript with kind permission of the publisher John Wiley and Sons.

Other results of this thesis have been presented to the MR community at international scientific meetings organized by the ESMRMB (European Society for Magnetic Resonance in Medicine and Biology) and ISMRM (International Society for Magnetic Resonance in Medicine) between October 2012 and May 2014. The conference abstracts are cited throughout the manuscript and can be found in the bibliography as well as in the publication list at the end of the document.

Apart from the main projects of this thesis (flexible TLR array, novel single-element TLR design), the author was involved in the development of a form-fitted  $^{31}\text{P}/^1\text{H}$  calf coil in Vienna, which has also been published in *Magnetic Resonance in Medicine* (Goluch, S., Kuehne, A., Meyerspeer M., Kriegl, R., Schmid A.I., Herrmann, T., Mallow, J., Hong, S.-M., Cho, Z.H., Bernading, J., Moser, E., Laistler, E., *A form-fitted three channel  $^{31}\text{P}$ , two channel  $^1\text{H}$  transceive coil array for calf muscle studies at 7 T*. *Magn Reson Med*, doi: 10.1002/mrm.25339). Several calf muscle studies have already been successfully performed with this coil, and it will be used in ongoing and future investigations.

MRI is a non-invasive imaging technique used primarily in medical environment to produce high quality images of the inside of the human body. MRI is based on the principle of nuclear magnetic resonance (NMR). It uses the magnetic properties of the atomic nuclei of the investigated material for imaging.

The image quality in MRI examinations depends on the achievable signal-to-noise ratio (SNR). In NMR research, several strategies to improve the SNR of MRI experiments are known: increasing the static magnetic field strength, improvement of the radiofrequency (RF) detection system, development of specialized acquisition sequences, and optimization of image reconstruction techniques. This thesis is concerned with the development of highly sensitive RF detectors for biomedical ultra-high field MRI. In particular, auto-resonant RF coils based on transmission line technology are investigated. These resonators may be fabricated on mechanically flexible substrate which enables form-fitting of the RF coil to the target anatomy, resulting in a significant SNR gain.

The main objective of this work is the development of a flexible RF coil array for high-resolution MRI on a human whole-body 7 T MR scanner. With coil arrays, the intrinsically high SNR of small surface coils may be exploited for an extended field of view. Further, arrays provide access to parallel imaging techniques which enable an acceleration of MR image acquisition, and parallel RF transmission which may be used to homogenize the transmit RF field, in particular at ultra-high field (UHF). This thesis describes the development, implementation and evaluation of the first flexible RF coil array composed of monolithic transmission line resonators (TLRs).

Secondly, in this work a novel TLR design is presented, the multi-turn multi-gap TLR design. The novel design expands the parameter space for optimizing the TLR geometry. This way, high-field MRI applications requiring a large FOV, like most biomedical applications, can be addressed by multi-turn TLR (MTLR) technology, which was not possible up to now.

# Thesis Outline

The presented thesis is subdivided into six chapters.

In Chapter I the basic principles of MRI are summarized. Starting from the phenomenon of NMR, the fundamentals of contrast and image formation in MRI are revised, and the origins of signal and noise detected in NMR experiments are described.

Chapter II provides an overview over state-of-the-art RF coil technology, introduces the TLR principle, and describes the methods to characterize and optimize these coils. Simulation methods, including analytical modeling and FDTD simulation are detailed; techniques for bench measurements and tests in the MR scanner are presented.

Chapter III describes the design, implementation and performance evaluation of a flexible TLR array. This chapter is a reproduction of the original article about the flexible TLR array (Kriegel, R., et al., Magn Reson Med, 2014, doi: 10.1002/mrm.25260).

In Chapter IV, data concerning the flexible TLR array is presented, which was not published in the article including additional high-resolution MR imaging results.

In Chapter V, studies concerning single TLR coils are presented. The proof-of-principle for the novel multi-turn multi-gap TLR design, which was established at 4.7 T, and its application at 7 T, are described. Further, an active detuning scheme is presented, which permits the use of TLRs as receive-only probes.

Chapter VI presents a general discussion and the most important conclusions of the performed studies. Further, it gives some perspectives for follow-up projects and future work.

The appendix of this thesis contains information on the derivation of the resonance condition for TLRs, and the individual steps needed for TLR fabrication. At the end of the manuscript all references, figures and tables are listed. A publication list and CV of the author are given.



# **Chapter I    Theoretical Background**

## I.1. Nuclear Magnetic Resonance

### I.1.1. Spins and magnetic moments

Atomic nuclei have a magnetic moment  $\mathbf{m}$  that originates from their intrinsic angular momentum  $\mathbf{I}$  called spin. The electromagnetic and mechanical properties of the nucleus are related to each other via the gyro-magnetic ratio  $\gamma$ , which is a nucleus-dependent constant.

$$\mathbf{m} = g_I \mu_N \frac{\mathbf{I}}{\hbar} = \gamma \mathbf{I} \quad \text{I.1}$$

$g_I$  is the nuclear g-factor which corrects the classically expected values for quantum mechanical and relativistic effects,  $\hbar$  is the Planck constant over  $2\pi$  and  $\mu_N$  is the nuclear magneton.

$$\mu_N = \frac{m_e}{m_p} \mu_B \quad \text{where} \quad \mu_B = \frac{e\hbar}{2m_e} \quad \text{I.2}$$

$m_e$  and  $m_p$  are the masses of the electron and the proton, respectively,  $e$  is the elementary charge, and  $\mu_B$  is the Bohr magneton. Due to the large mass of the proton and the neutron compared to the electron mass, magnetic moments from nucleon spins are approximately by a factor of 1836 smaller than those from electron spins.

A nucleus' spin may have positive or negative sign (corresponding to two rotational directions), and both the absolute value  $|\mathbf{I}|$  and the component  $I_z$  parallel to an external magnetic field (per convention along the z-direction) are quantized.

$$|\mathbf{I}| = \sqrt{I(I+1)}\hbar \quad \text{with} \quad I = 0, \frac{1}{2}, 1, \frac{3}{2}, \dots \quad \text{I.3}$$

$$I_z = m_I \hbar \quad \text{with} \quad m_I = -I, -I+1, \dots, I-1, I \quad \text{I.4}$$

$I$  is called the (nuclear) spin quantum number, and  $m_I$  is the magnetic quantum number.

Both, the proton and the neutron have spin quantum number  $I = 1/2$ , which results in two possibilities for the magnetic quantum number  $m_I = \pm 1/2$ . Depending on the mass number  $A$  and atomic number  $Z$  of a nucleus, it can have either an integer or a half-integer nuclear spin quantum number  $I$ .

It should be mentioned that the coupling of the nucleon spins to the spin of the compound nucleus is not straight-forward, especially for nuclei with a large number of protons. In that case also the orbital motion of the protons within the nucleus has to be taken into account, in addition to the spins of all nucleons. Thus, for large nuclei the spin quantum number often has to be determined by experimental methods.

Table I.1 lists the gyromagnetic ratios of some nuclei used in biomedical magnetic resonance. The table also contains the respective spin quantum numbers, as well as the natural abundance, i.e. the abundance among all natural isotopes of the chemical element.

$^A\text{Nucleus}$	Nuclear spin quantum number $I$	Gyrom. Ratio $\gamma$ (MHz/T)	Natural Abundance (%)
$^1\text{H}; ^2\text{H}$	$1/2, 1$	42.58; 6.54	99.985, 0.015
$^{13}\text{C}$	$1/2$	10.71	1.1
$^{14}\text{N}; ^{15}\text{N}$	$1, 1/2$	3.08; -4.31	99.6, 0.4
$^{17}\text{O}$	$5/2$	-5.77	0.04
$^{19}\text{F}$	$1/2$	40.08	100
$^{23}\text{Na}$	$3/2$	11.27	100
$^{31}\text{P}$	$1/2$	17.25	100

Table I.1 Nuclei relevant for NMR and their properties

## I.1.2. Nuclear polarization

In the absence of an external magnetic field, the nuclear magnetic moments in a sample are randomly oriented. When a magnetic field  $\mathbf{B}_0$  (typically along the z-direction) is applied to the system, the magnetic moments align either parallel or anti-parallel to the applied field.

The component of the magnetic moment  $\mathbf{m}$  along  $\mathbf{B}_0$  is then

$$m_z = \gamma m_l \hbar \quad \text{I.5}$$

For a spin- $1/2$  system, e.g. the proton, there are two possible values for  $m_z$ .

$$m_z = \begin{cases} +\frac{1}{2}\gamma\hbar & \mathbf{m} \text{ aligned with } \mathbf{B}_0 \\ -\frac{1}{2}\gamma\hbar & \mathbf{m} \text{ aligned against } \mathbf{B}_0 \end{cases} \quad \text{I.6}$$

The potential energy of a magnetic moment in an external magnetic field is given by

$$E = -\mathbf{m} \cdot \mathbf{B}_0 \quad \text{I.7}$$

This indicates that the spins aligned parallel to the external field are in a lower energy state than the spins oriented anti-parallel to the field (Figure I.1).

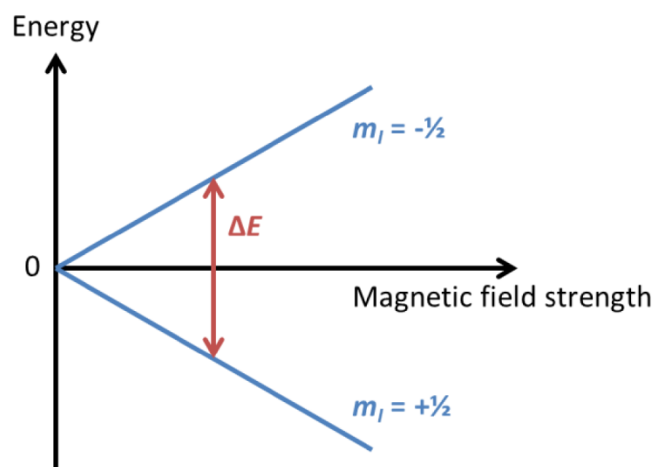


Figure I.1 Energy difference between spin states as function of the magnetic field strength

The energy difference between the two states increases linearly with the field strength  $B_0$ .

$$\Delta E = \gamma \hbar B_0 \quad \text{I.8}$$

The splitting of energy levels in the presence of a magnetic field is called Zeeman effect. By emission or absorption of photons with energy  $\hbar\omega = \Delta E$  transitions between the two levels can occur. The angular resonance frequency of this transition is the so-called Larmor frequency times  $2\pi$ ,  $\omega_L = 2\pi f_L$ .

$$\omega_L = \gamma B_0 \quad \text{I.9}$$

The energy difference between the two states leads to an imbalance in the spin populations ( $N_{-1/2}$  and  $N_{+1/2}$ ), which can be described by Boltzmann statistics.

$$\frac{N_{-1/2}}{N_{+1/2}} = \exp\left(-\frac{\gamma \hbar B_0}{k_B T}\right) \quad \text{I.10}$$

$k_B$  is the Boltzmann constant and  $T$  is the absolute temperature. Equation I.10 implies that more spins will occupy the state of lower energy than the state of higher energy. This gives rise to a net magnetization  $\mathbf{M}_0$  of the spin system. At room temperature and intermediate static magnetic field strength (1 - 3 T), however, the thermal energy  $k_B T$  is much larger than the magnetic energy  $\gamma \hbar B_0$ . Therefore the Boltzmann factor is dominated by  $k_B T$ , resulting in a very low net magnetization, for instance at  $B_0 = 3$  T:

$$\frac{N_{-1/2}}{N_{+1/2}} \approx \frac{1}{10^5} \quad \text{I.11}$$

In a typical NMR experiment the number of nuclei is very large; therefore, the resulting magnetization is still detectable. The total magnetization is proportional to the difference in population of the lower and the higher energy state  $\Delta N = N_{-1/2} - N_{+1/2}$ .

$$\Delta N = N \cdot \tanh\left(\frac{\gamma \hbar B_0}{2k_B T}\right) \approx \frac{N \gamma \hbar B_0}{2k_B T} \quad \text{for } k_B T \gg \gamma \hbar B_0 \quad \text{I.12}$$

$N = N_{-1/2} + N_{+1/2}$  is the total number of spins in the system.

$$M_0 = \Delta n \cdot m_z \approx \frac{N\gamma\hbar B_0}{2k_B T} \cdot m_z \quad \text{I.13}$$

This way the whole spin system can be characterized in terms of the macroscopic magnetization, which can be described by classical physics instead of quantum mechanics.

### I.1.3. Larmor precession

When exposed to a magnetic field  $\mathbf{B}$ , the magnetic moment  $\mathbf{m}$  is subject to a torque  $\mathbf{T}$ , which forces it in the direction parallel to the external field.

$$\mathbf{T} = \mathbf{m} \times \mathbf{B} \quad \text{I.14}$$

The angular momentum of the magnetic moment counteracts this force.

$$\mathbf{T} = \frac{d\mathbf{l}}{dt} \quad \text{I.15}$$

The combination of equations I.14, I.15, and I.1 yield the equation of motion for the magnetic moment  $\mathbf{m}$ .

$$\frac{d\mathbf{m}}{dt} = \gamma \cdot \mathbf{m} \times \mathbf{B} \quad \text{I.16}$$

It can be extended to the total magnetization  $\mathbf{M}$ , which is given by the sum over all magnetic moments in the sample. This then yields the Bloch equation [1].

$$\frac{d\mathbf{M}}{dt} = \gamma \cdot \mathbf{M} \times \mathbf{B} \quad \text{I.17}$$

For the static magnetic field  $\mathbf{B}_0$  along the z-direction, the equations of motion for the individual components of  $\mathbf{M}$  yield

$$\frac{dM_x}{dt} = \gamma \cdot M_y B_0 \quad \frac{dM_y}{dt} = \gamma \cdot M_x B_0 \quad \frac{dM_z}{dt} = 0 \quad \text{I.18}$$

The solutions describe a precession of the magnetization vector about the z-axis with the Larmor frequency  $\omega_L$ .

$$\begin{aligned}
 M_x(t) &= M_{x0} \cdot \cos(\omega_L t) + M_{y0} \cdot \sin(\omega_L t) \\
 M_y(t) &= -M_{x0} \cdot \sin(\omega_L t) + M_{y0} \cdot \cos(\omega_L t) \\
 M_z(t) &= M_{z0}
 \end{aligned}
 \tag{I.19}$$

When in addition to  $\mathbf{B}_0$  a radio frequency (RF) field  $\mathbf{B}_1$  is applied, which is perpendicular to the static magnetic field and rotates with the Larmor frequency  $\omega_L$  about the z-axis, the equations of motion for the components of  $\mathbf{M}$  become

$$\begin{aligned}
 \frac{dM_x}{dt} &= \gamma \cdot (M_y B_0 - M_z B_{1y}) \\
 \frac{dM_y}{dt} &= \gamma \cdot (-M_x B_0 + M_z B_{1x}) \\
 \frac{dM_z}{dt} &= \gamma \cdot (M_x B_{1y} - M_y B_{1x})
 \end{aligned}
 \tag{I.20}$$

These are the Bloch equations in the laboratory frame in the absence of relaxation. The solutions are given by

$$\begin{aligned}
 M_x(t) &= M_0 \cdot \sin(\omega_1 t) \cdot \sin(\omega_L t) \\
 M_y(t) &= M_0 \cdot \sin(\omega_1 t) \cdot \cos(\omega_L t) \\
 M_z(t) &= M_0 \cdot \cos(\omega_1 t)
 \end{aligned}
 \tag{I.21}$$

where  $\omega_1 = \gamma B_1$  and  $M_0$  is the magnitude of the magnetization vector  $\mathbf{M}$ .

With the RF field applied in addition to the static magnetic field, the magnetization vector precesses about the sum of the two fields  $\mathbf{B} = \mathbf{B}_0 + \mathbf{B}_1$ . At  $t = 0$  the magnetization is parallel to the z-axis, at  $t = \pi/2\omega_1$  the magnetization vector lies completely in the xy-plane.  $M_x(t)$  reaches the maximum value  $M_0$  only if  $M_y(t)$  is zero and vice versa.

In a typical NMR experiment, an RF field at the resonance frequency is applied for a short time, i.e. an RF pulse, in addition to a static magnetic field. This RF pulse tips the

magnetization away from its equilibrium position along the z-axis into the transverse plane. The angle by which the magnetization vector is tipped is called the flip angle, and depends on the amplitude of the applied  $B_1$  field and the pulse duration  $\tau$ .

$$\alpha = \int_0^{\tau} \gamma B_1(t) dt \quad 1.22$$

For a rectangular pulse profile this can be reduced to

$$\alpha = \gamma B_1 \tau \quad 1.23$$

### **1.1.4. Relaxation phenomena**

After the perturbation by an on-resonance RF pulse the spin system will return to the equilibrium state. This process is called relaxation. Relaxation can be described by two independent processes when viewing longitudinal and transverse magnetization as separate entities. While the longitudinal magnetization is recovering, the transverse magnetization is decaying.

During the recovery of the longitudinal magnetization energy is released to the molecular lattice; therefore this process is called longitudinal or spin-lattice relaxation. The rate of recovery is given by the time constant  $T_1$  (Figure I.2). The system's rate of return towards equilibrium is proportional to the deviation from the equilibrium. Mathematically, this can be described by the following equation

$$\frac{dM_z}{dt} = -\frac{M_z - M_0}{T_1} \quad 1.24$$

The solution of this differential equation is given by

$$M_z(t) = M_0 \cdot (1 - e^{-\frac{t}{T_1}}) + M_z(0_+) \cdot e^{-\frac{t}{T_1}} \quad 1.25$$

$M_z(0_+)$  is the z-magnetization immediately after excitation.



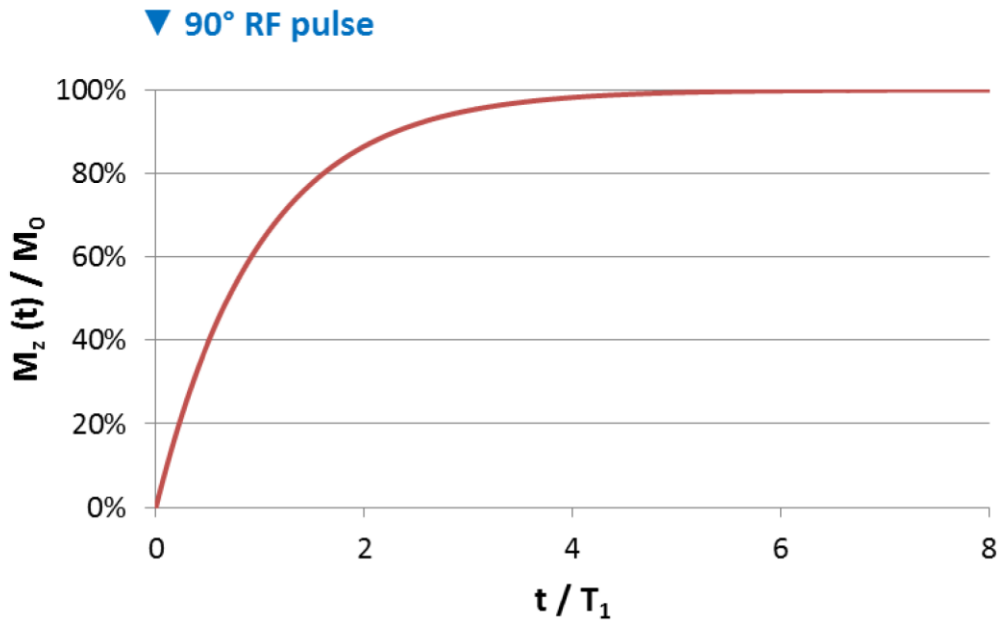


Figure I.2 T<sub>1</sub> relaxation

Simultaneously to the recovery of the longitudinal magnetization, the transverse magnetization decays due to the so-called spin-spin relaxation. It is caused by the exchange of energy among the spins themselves, leading to a decrease in phase coherence and to a reduction in NMR signal.

Spin-spin relaxation is an exponential decay process as well, and is characterized by the time constant  $T_2$  (Figure I.3).

$$\frac{dM_{x,y}}{dt} = -\frac{M_{x,y}}{T_2} \quad 1.26$$

$$M_{x,y}(t) = M_{x,y}(0) \cdot e^{-\frac{t}{T_2}} \quad 1.27$$

T<sub>1</sub>- and T<sub>2</sub>-relaxation take place independently from each other. The first is due to the exchange of energy between the spin system and the lattice, while the second reflects signal loss due to randomization of spin orientation. Although energy is exchanged within the spin system, spin-spin relaxation does not represent energy loss from the system. T<sub>2</sub>-relaxation is

an entropy-process, as there is no net energy transfer from or to the spin system; only global entropy is increased.

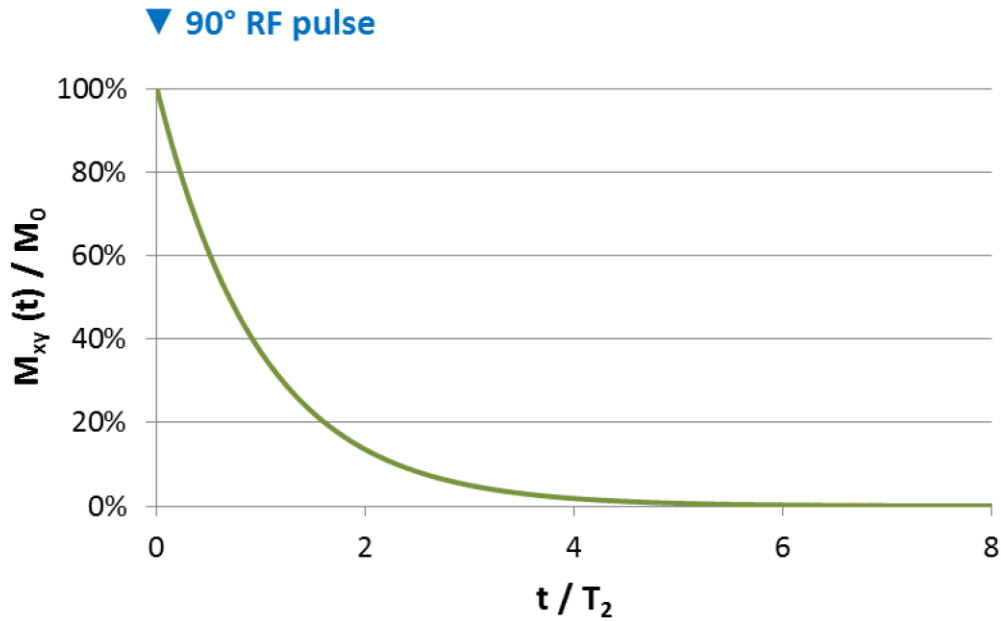


Figure I.3  $T_2$  relaxation

Different tissue types have different relaxation times  $T_1$  and  $T_2$ , which is exploited for obtaining image contrast in anatomical MRI (Table I.2, [2]).

Tissue	$T_1$ (ms)	$T_2$ (ms)
Gray matter	950	100
White matter	600	80
Cerebrospinal fluid	4500	2200
Muscle	900	50
Fat	250	60
Blood	1200	100 - 200

Table I.2 Representative values for  $T_1$  and  $T_2$  relaxation times of various tissues at 1.5 T

Experimentally, the NMR signal decays faster than predicted by  $T_2$ -relaxation. Inhomogeneities in the static magnetic field  $B_0$  cause slight variations in local resonance frequency, which leads to an additional dephasing of the spins. The accelerated decay rate is called  $T_2^*$ .

$$\frac{1}{T_2^*} = \frac{1}{T_2} + \frac{1}{T_2'} \quad 1.28$$

$T_2'$  accounts for  $B_0$  inhomogeneities. These inhomogeneities originate mainly from susceptibility differences between the different sample tissues and the air in the scanner bore, as well as from technical imperfections.

The simplest NMR experiment is the generation of a Free Induction Decay (FID). The sample is positioned in a uniform static magnetic field  $B_0$ ; therefore, the net macroscopic sample magnetization is initially aligned parallel to the external field. An RF coil, which may create an oscillating field  $B_1$  at the Larmor frequency, is placed in the vicinity of the sample. An RF pulse is used to flip the magnetization into the transverse plane; then the RF source is switched off. While the magnetization rotates in the transverse plane, it induces an electromotive force (emf) in the RF coil that decays exponentially with time constant  $T_2^*$  due to the different relaxation processes; this is the FID signal as shown in Figure I.4.

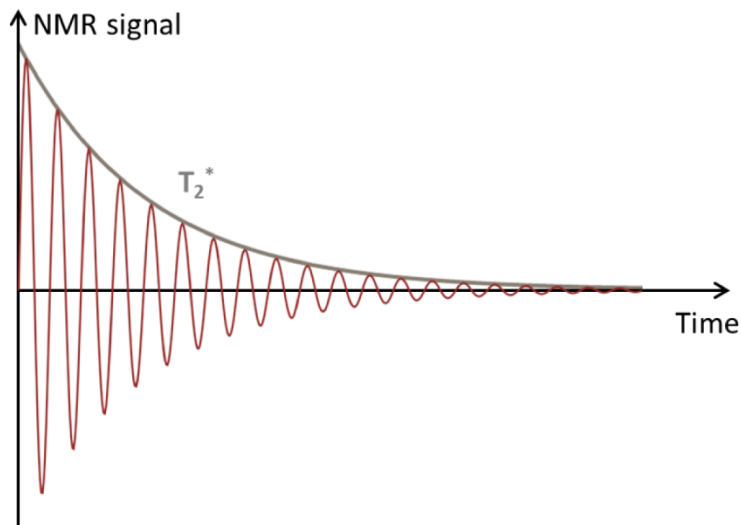


Figure I.4 Free induction decay

## I.2. Principles of magnetic resonance imaging

### I.2.1. Spin echo and gradient echo

Generally, in MRI not the FID signal is sampled, but an echo. The FID signal decays rapidly as the transverse magnetization decays with  $T_2^*$ . An echo can be generated by refocusing the transverse magnetization either by the spin echo or the gradient echo technique.

In order to generate a spin echo [3], the sample magnetization is rotated into the transverse plane by a  $90^\circ$  RF pulse. Initially, the nuclear spins precess coherently about  $B_0$ , but  $T_2^*$  effects will cause them to steadily dephase as described in section I.1.4, which leads to a decay of the detectable NMR signal. Applying a  $180^\circ$  pulse which flips the magnetization about the y-axis, for instance, reverts the sign of the phase shift. A spin that had been precessing fast (slow), and acquired a positive (negative) phase shift, will then experience a negative (positive) phase shift. However, the local field inhomogeneities causing the initial dephasing of the spins are constant in space and are not affected by the  $180^\circ$  pulse. Therefore, the spin will tend to catch up (slow down) back to zero phase shift. This way the transverse sample magnetization is restored resulting in a detectable NMR signal, the so-called spin-echo (Figure I.5).

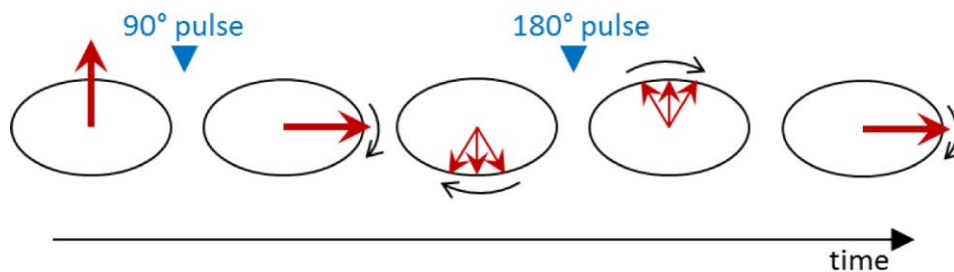


Figure I.5 Generation of a spin echo

If the 180 degree pulse is switched behind the 90 degree excitation pulse after the time  $\tau$ , the echo is generated at echo time  $T_E = 2\tau$ . When several 180 degree pulses are following each other, several spin echoes appear. The amplitudes of the spin echoes then decrease with the time constant  $T_2$  [4] (Figure I.6).

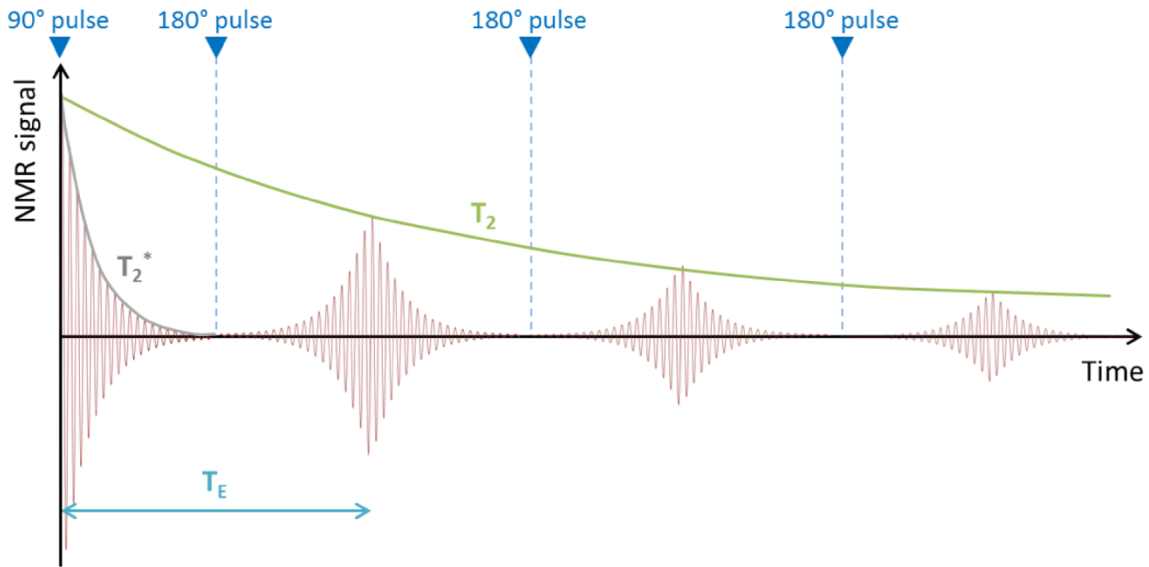


Figure I.6 Spin echo train

Another way to create an echo is the gradient-echo technique [5]. A magnetic field gradient switched across the sample directly after the RF pulse artificially dephases the spins more quickly than  $T_2^*$  decay since it causes different precession frequencies at different locations (Equation I.9). By applying a reversed field gradient the spins will be in phase again (Figure I.7). An echo, the so-called gradient echo, can be measured during this re-phasing. The gradient echo technique is faster than the spin-echo technique, since the signal is destroyed and built up within the  $T_2^*$  time.

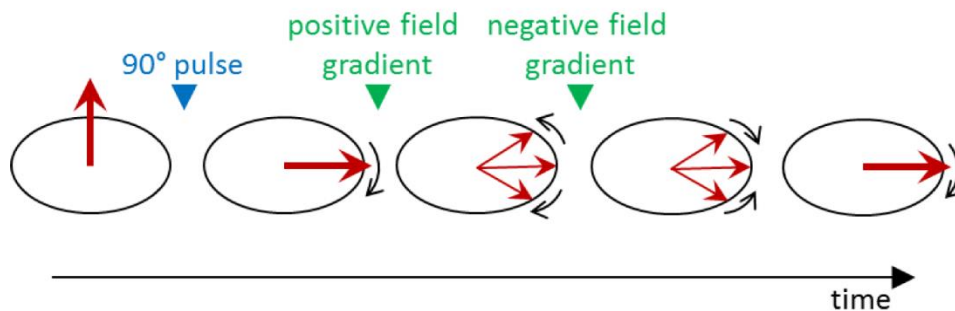


Figure I.7 Generation of a gradient echo

A spin echo refocuses dephasing due to susceptibility or field inhomogeneities and can be used to give  $T_2$  contrast. A gradient echo, on the other hand, gives  $T_2^*$  contrast.

### I.2.2. Localization of signals

To create an image of a sample it is necessary to localize the NMR signal. This is achieved by superimposing a (small) magnetic field gradient onto the main magnetic field  $B_0$  in a way that the resonance frequency becomes a function of the position in space [6].

An MR scanner is typically equipped with three orthogonal gradient coils, each designed to generate a magnetic field gradient  $G_x$ ,  $G_y$  or  $G_z$  that varies linearly along its axis within a restricted area.

$$\mathbf{G} = G_x \hat{\mathbf{x}} + G_y \hat{\mathbf{y}} + G_z \hat{\mathbf{z}} \quad 1.29$$

The total magnetic field at position  $\mathbf{r}$  is then

$$\mathbf{B}(\mathbf{r}) = (B_0 + \mathbf{G} \cdot \mathbf{r}) \hat{\mathbf{z}} \quad 1.30$$

This spatially variable magnetic field can be used either to selectively excite the spins [7], or to spatially encode the NMR signal that is emitted by the sample after excitation. Typically, a combination of these two concepts is applied: A single slice is selectively excited, and then the signal originating from this slice is spatially encoded.

### I.2.3. Slice selection

By applying a slice selective magnetic field gradient simultaneously with an RF pulse it is possible to achieve the excitation of one particular slice (Figure I.8). In order to select a slice parallel to the  $xy$ -plane, a magnetic field gradient orthogonal to this plane, i.e. in  $z$ -direction, has to be applied. The strength of the slice selection gradient and the bandwidth of the applied RF pulse determine the location and the thickness of the slice in which the resonance condition is met. Outside of the slice, the spins are not excited by the RF pulse; a transverse magnetization and therefore the MR signal is only generated within the selected slice. The shape of the excitation pulse determines the slice profile. For small flip angles the slice profile in the frequency domain is given by the Fourier Transform (FT) of the RF pulse envelope. For example, an ideal, infinitely long a sinc-shaped ( $\text{sinc}(x) = \sin(x)/x$ ) excitation pulse results in a rectangular profile of the selected slice.

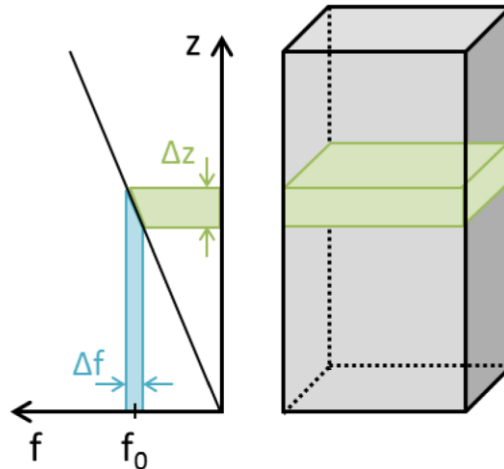


Figure I.8 Slice selection

The principle of slice selection can be extended in a way to excite an arbitrary region of the sample. This can be achieved by carefully designing the RF pulse envelopes [8,9]. Finally, parallel transmission techniques, e.g. Transmit SENSE [10], which uses multiple RF transmit channels, give additional degrees of freedom in pulse design; this can be employed to shorten spatially selective RF pulses.

#### I.2.4. Frequency encoding

Applying an RF pulse together with the slice selection gradient excites the spins in a certain region of the sample from which the MR signal will emerge. To generate an image, it is necessary to distinguish signals from different points in the excited volume, i.e. spatial encoding is needed. There are two ways to encode the signal: frequency encoding and phase encoding.

Frequency encoding exploits the same principle as slice selection, but with the magnetic field gradient applied during image readout rather than during excitation. This way the precession frequency of the spins that have been excited before, is modified (Figure I.9). For example, the slice selection gradient  $G_z$  is applied along the z-direction. If during readout of a gradient  $G_x$  along the x-direction is applied, the precession frequency becomes a function of the position along the x-direction.

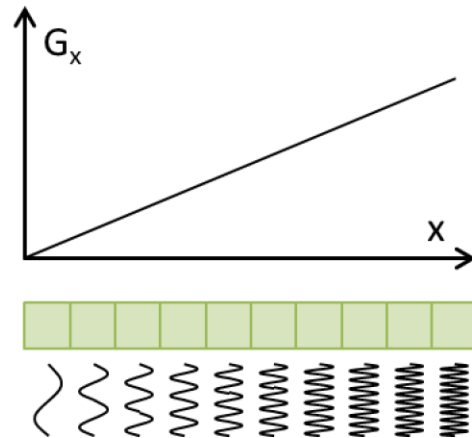


Figure I.9 Frequency encoding

The MR signal is then a mixture of frequencies along the x-direction. The signal contribution of each frequency component can be determined by discrete Fourier transformation of the signal. This will re-allocate a portion of the spectrum with a certain bandwidth to a spatial location on the x-axis to reconstruct the image. The readout bandwidth depends on the total field of view (FOV) to be covered, the strength of the gradient  $G_x$ , and the number of sampled points.

### 1.2.5. Phase encoding

Frequency encoding allows spatial encoding only along one dimension. Applying the same method on two dimensions will result in ambiguity with respect to the relationship of frequency and spatial position.

Another possibility for spatial encoding of the signal is to make its phase a function of position. This is achieved by applying another gradient  $G_y$  along the y-direction (when frequency encoding is done along x-direction) briefly before the readout of the signal [11]. As a result, the spins at different y-positions will precess with slightly different frequencies for a short time. During readout  $G_y$  is switched off. Then all spins again precess with the same frequency but with different phase which is a function of the position along the y-direction (Figure I.10). In order to fully encode an image, phase encoding has to be repeated for each data point along the frequency encoding direction.



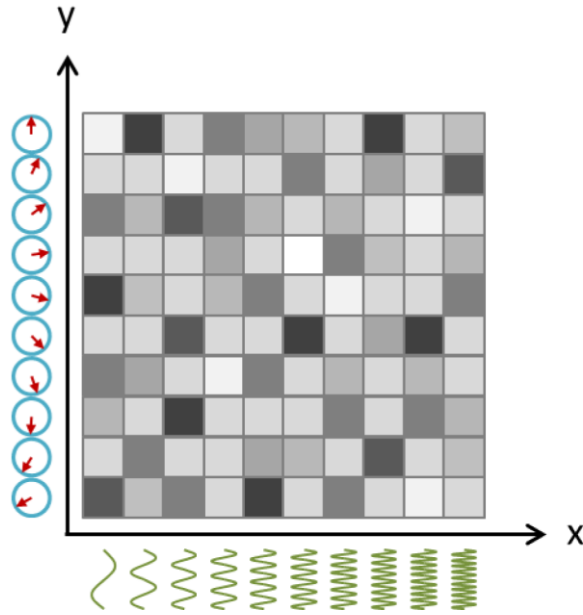


Figure I.10 Image formation by phase and frequency encoding

The combination of slice selection, frequency encoding and phase encoding is the basis for most common 2D MR imaging sequences. In 3D MR imaging, the whole volume of interest is excited at once instead of using slice selective excitation. Then, phase encoding along the third dimension is applied in addition to the phase and frequency encodings used in 2D imaging.

### 1.2.6. k-space

By frequency and phase encoding a raw data matrix is filled line by line in reciprocal image space, which is called k-space in MRI [12,13]. k-space is related to normal image space via Fourier transformation.

After the excitation pulse (at  $t = 0$ ), image readout is determined by the applied gradient wave forms, corresponding to readout trajectories through k-space.

$$\mathbf{k}(t) = \gamma \int_0^t \mathbf{G}(t') dt' \quad \text{I.31}$$

The signal timecourse is then

$$S(t) \propto \int_{\text{sample}} |\mathbf{M}| e^{-i\mathbf{k}(t) \cdot \mathbf{r}} d\mathbf{r} \quad \text{I.32}$$

where  $S$  and  $|\mathbf{M}|$  constitute a Fourier pair.

During frequency encoding, data points are recorded along lines in k-space, while during phase encoding the location in k-space is altered by applying a gradient without sampling the signal, resulting in sudden jumps in the trajectory. To sample a complete image, it is necessary that the k-space trajectory covers the whole k-space; in practice, it is not possible to cover the whole k-space but only a subset of discrete points depending on the bandwidth, the FOV, and the desired resolution. The center of k-space determines low spatial frequencies, i.e. large image structures, and the image contrast, while higher spatial frequencies, i.e. edges and fine details, are sampled further out. The k-space formalism in combination with pulse sequence diagrams, that show the timing of the applied RF pulses and gradients, is a powerful tool to describe MR imaging sequences.

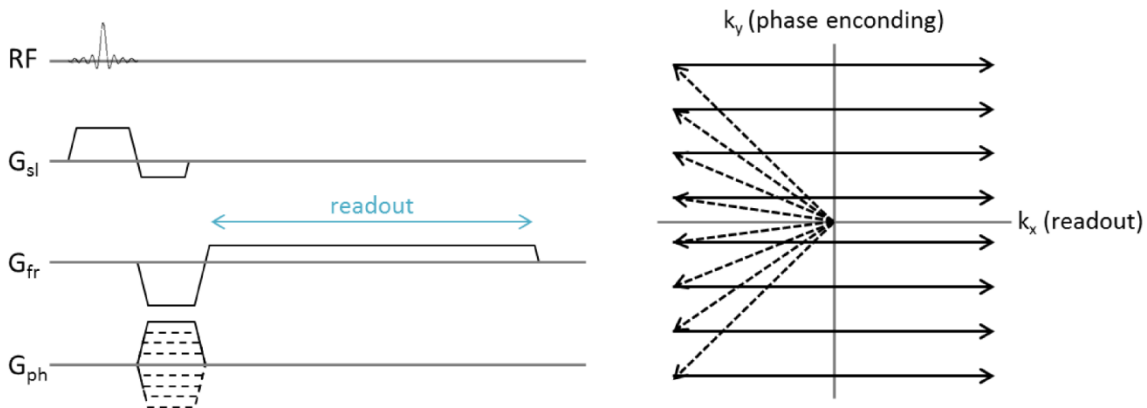


Figure I.11 Spin warp sequence, pulse sequence diagram and k-space trajectory

Figure I.11 shows the spin warp sequence [5] as an example for a basic MR imaging sequence. A slice selection gradient  $G_{sl}$  is applied simultaneously to the  $90^\circ$  excitation pulse. This gradient dephases the spins within the slice. Therefore, an additional gradient of opposite polarity and approximately half the area (area = amplitude  $\times$  duration) is applied to

compensate for this effect. The negative lobe of  $G_{fr}$ , and  $G_{ph}$  (solid line) set the start of the k-space trajectory to the upper left corner of k-space. During readout of the signal only the gradient  $G_{fr}$  is applied causing a sweep of  $\mathbf{k}$  along  $k_x$  (from left to right). This procedure has to be repeated with repetition time  $T_R$  for different  $G_{ph}$  (dashed lines) until all k-space lines are filled. The acquired k-space data is the Fourier transformed in 2D to generate the final image.

### **1.2.7. Parallel imaging techniques**

Conventional MR imaging methods rely on magnetic field gradients for spatial encoding, and sample the data sequentially using a single RF coil. In particular, phase encoding limits the image acquisition rate, since a separate echo has to be acquired for each phase encoding step. The number of phase encoding steps required for image formation can be reduced by parallel imaging techniques [14,15]. Parallel imaging can be implemented when receiver coil arrays [16], i.e. assemblies of several coils used in parallel, are used. Each coil in the array is placed at a different location in space and therefore provides different spatial information. The first clinically applicable parallel imaging methods were SMASH (SiMultaneous Acquisition of Spatial Harmonics) [17] and SENSE (SENSitivity Encoding) [18].

Both, SENSE and SMASH require a prior estimation of the individual coil sensitivities of the receiver array, also called  $B_1$  maps. The basic concept of SMASH is that a linear combination of these sensitivity profiles can be used to generate missing phase-encoding steps. For that purpose, the sensitivity values are combined with appropriate linear weights to generate composite sensitivity profiles with sinusoidal spatial sensitivity variations. These spatial harmonics reproduce the same effect in the acquired data as phase encoding gradients. This way, several phase encoding steps may be reconstructed from a single, parallel acquisition.

SMASH has been extended by auto-calibration techniques, which do not require a prior estimation of the coil sensitivity profiles. AUTO-SMASH [19] uses a small number of additional auto-calibration signals (ACS), i.e. k-space lines acquired during the actual scan, which are used to automatically derive the weights for channel combination. The reconstruction procedure of the AUTO-SMASH approach was improved by the concept of

variable-density (VD)-AUTO-SMASH [20], which uses multiple ACS lines in the center of k-space, and finally by GRAPPA (GeneRalized Autocalibrating Partially Parallel Acquisitions) [21]. The GRAPPA method provides uncombined single coil images, instead of composite sensitivity profiles. These individual images can then be combined using a magnitude reconstruction technique (e.g. sum-of-squares). This has been shown to significantly improve the SNR, especially at low reduction factors  $R$  [22]. Further, GRAPPA may be applied with arbitrary coil configurations.

While SMASH-based methods perform the reconstruction in k-space, SENSE reconstructs the data in image space. With SENSE, k-space is undersampled in the phase encoding direction, which causes Nyquist aliasing in image space. Using knowledge of the sensitivity profiles of all receive array elements, aliased images may be unfolded and combined to generate a single, fully sampled image. The total acquisition time is shortened because the number of phase encoding steps is reduced by undersampling each channel. SENSE has been extended to 2D-SENSE [23], and it has been shown that it can be applied to arbitrary k-space trajectories [24]. Like GRAPPA, SENSE can be used with arbitrary coil configurations; however, it relies on highly accurate sensitivity maps, which can pose a problem for in-vivo applications.

The achievable SNR is inevitably reduced by undersampling an image. In comparison to a fully encoded image, the SNR is reduced by the square root of the acceleration factor  $R$  and by the geometry factor  $g$ , which accounts for coil-dependent noise amplification across the image volume.

$$SNR_{acc} = \frac{SNR_{full}}{g \cdot \sqrt{R}} \quad 1.33$$

The  $g$ -factor varies throughout the sample volume, and should ideally be close to one. A  $g$ -factor  $g = 1$  could only be achieved when the coils have completely uncorrelated sensitivity profiles along the phase-encoding direction. Likewise, high  $g$ -factors occur when coils have very similar sensitivities, with  $g$  going to infinity for identical sensitivity profiles.

## I.3. Signal and Noise in NMR experiments

### I.3.1. The Reciprocity Principle

Signal and noise detected in NMR experiments can be quantified using the Reciprocity Principle [25,26]. This principle means that the receive sensitivity of a coil is proportional to its transmit field, i.e. that the electromagnetic force *emf* induced in an RF coil by a rotating magnetic dipole  $\mathbf{m}$  at a given point in space is proportional to the magnetic field  $\mathbf{B}_1$  produced at the same point by a current  $I$  circulating in the coil. The  $B_1$ -field generated by the coil is generally strong in close vicinity to the coil, and becomes weaker with increasing distance; therefore, the *emf* induced by the rotating magnetic dipole  $\mathbf{m}$  located close to the coil is higher than the *emf* that would be induced by the same dipole located further away. It can be shown that the *emf* induced by  $\mathbf{m}$  is given by

$$emf = -\frac{\partial \mathbf{B}_1 \cdot \mathbf{m}}{\partial t} \frac{1}{I} \quad 1.34$$

For a sample volume  $V$  with the sample magnetization  $\mathbf{M}_0$  flipped into the  $xy$ -plane by a  $90^\circ$  RF pulse the *emf* induced in the coil is given by

$$emf = -\int_{\text{sample}} \frac{\partial \mathbf{B}_1 \cdot \mathbf{M}_0}{\partial t} \frac{1}{I} dV \quad 1.35$$

$\mathbf{B}_1$  and  $\mathbf{M}_0$  are both rotating in the  $xy$ -plane at the Larmor frequency  $\omega_0$ . Assuming that the  $B_1$  field is homogeneous over the sample volume (which is reasonable for typical voxel sizes of several cubic millimeters), and neglecting phase, it can be shown [25] that equation 1.35 yields

$$emf = \omega_0 \frac{B_{1,xy}}{I} M_0 V \cos(\omega_0 t) \quad 1.36$$

where  $B_{1,xy}$  is the transverse component of the  $B_1$  field.

A rigorous mathematical description of the application of the Reciprocity Principle for calculation of the NMR signal strength can be found in an article by D. Hoult [26].

Since both,  $\omega_0$  (Equation I.9) and  $M_0$  (Equation I.13) are proportional to  $B_0$ , it follows that the  $emf$  induced in the coil is proportional to the square of the static magnetic field.

$$emf \propto B_0^2 \quad \text{I.37}$$

### I.3.2. Noise mechanisms

The data quality in NMR experiments is mainly restricted by different types of noise superimposed on the MR signal. Following reciprocity in form of the Fluctuation Dissipation Theorem [27], noise sources are powered by thermal agitation in dissipating media [28]. An equivalent resistance  $R_{eq}$  can be defined as the sum over the equivalent resistances associated with respective dissipation rates in the coil material, the sample, and other involved media.

The noise voltage associated with thermal noise is

$$v = \sqrt{4k_B T_{eq} R_{eq} \Delta f} \quad \text{I.38}$$

where  $k_B$  is the Boltzmann constant, and  $\Delta f$  is the receiver bandwidth.  $T_{eq}R_{eq}$  is the equivalent temperature-weighted sum of resistances according to the respective dissipation rates and local temperatures in the different media.

The two significant noise sources contributing to  $R_{eq}$  in an MR experiment are the RF coil ( $R_C$ ) and the sample itself ( $R_S$ ).

$$R_{eq} = R_C + R_S \quad \text{I.39}$$

Coil noise originates from ohmic losses in the coil material, which are increased at high frequencies due to the skin effect. The skin effect reduces the current penetration in conducting media, and therefore decreases the effective cross sectional area of conductors. This results in a slight increase of coil resistance with increasing static field strength [25].

$$R_C \propto \sqrt{B_0} \quad \text{I.40}$$

In addition, noise is coupled to the coil from the volume of the sample that is penetrated by the  $B_1$  field of the RF coil. Sample noise depends on the conductivity (approximately 0.7 S/m for biological tissues at 300 MHz [29]) and temperature of the sample, and can be classified into three different mechanisms: magnetically coupled noise, capacitively coupled noise, and spin noise.

Magnetically coupled noise originates from induced eddy currents and thermally agitated electric charges within conductive samples, e.g. biological tissues. Circular components of the Brownian motion of these charges induce a voltage in the RF coil which cannot be distinguished from the MR signal and, therefore, results in random fluctuation of the measured signal.

Capacitively coupled noise is caused by potential differences between electrical ground and other circuit parts reaching high potential values during RF excitation. These potential differences evoke alternating electric fields which penetrate the sample and induce dielectric losses. Inversely, thermally fluctuating dipoles on the sample surface induce noise in the RF coil. This noise is not coupled to the coil via the magnetic induction pathway and can therefore be reduced by means of coil design, e.g. by using distributed series capacitors, in a way to equilibrate the electric potential with respect to the sample [30].

Spin noise originates from the nuclear spin system itself and is caused by fluctuating transverse magnetic moments [31]. Spin noise plays a less important role for MRI experiments because they do not rely on high spectral resolution (typically in the kHz range), however, it may spoil MR spectroscopy experiments using linewidths of approximately 1 Hz.

Therefore, for MRI experiments with a coil design that minimizes capacitively coupling of sample noise, magnetic coupling is the dominant noise pathway. The magnetic coupling between coil and sample increases linearly with frequency, which increases the sample noise at higher static field strength [32].

$$R_S \propto \nu_S^2 \propto B_0^2 \quad 1.41$$

### I.3.3. Signal-to-noise ratio

The signal-to-noise ratio (SNR) is defined as the ratio of the electro-motive force *emf* induced in the coil over the noise voltage. From equations I.36 and I.38 an expression for the SNR in an elementary volume  $V$  with a transverse magnetization component  $M_T$  can be derived [25,33].

$$\text{SNR} \approx F^{-\frac{1}{2}} \frac{\omega_0(B_1/I)}{\sqrt{4k_B T_{\text{eq}} R_{\text{eq}} \Delta f}} V M_T \sqrt{t_{\text{acq}}} \quad \text{I.42}$$

$F$  is a noise factor which accounts for noise induced by the scanner electronics, and  $t_{\text{acq}}$  is the acquisition time.

The contribution of the RF coil is characterized by the coil sensitivity factor  $S_{\text{RF}}$ , which represents the SNR of the coil in time-domain for given imaging parameters.

$$S_{\text{RF}} = \frac{\omega_0(B_1/I)}{\sqrt{4k_B T_{\text{eq}} R_{\text{eq}}}} \quad \text{I.43}$$

The coil sensitivity linearly depends on the magnetic coupling coefficient  $B_1/I$ , i.e. the amplitude of the magnetic field produced by the coil per unit current. Using Biot-Savart's law to calculate the  $B_1$  field of a circular loop at distance  $a$  along its axis, it can be shown that this factor decreases with increasing coil radius  $r$ .

$$\frac{B_1}{I} = \frac{\mu_0}{2} \frac{r^2}{(r^2 + a^2)^{3/2}} \quad \text{I.44}$$

where  $\mu_0$  is the vacuum permeability. Thus, a small coil has higher sensitivity in the region close to the coil than a larger coil.

The combination of equations I.37, I.40, and I.41 yield the following relationship between SNR and  $B_0$  [32,34].



$$\text{SNR} \propto \frac{B_0^2}{\sqrt{B_0^2 + \alpha\sqrt{B_0}}} \quad \text{I.45}$$

The factor  $\alpha$  depends on the ratio of  $R_c$  to  $R_s$ , and can be used to define the boundary between the coil noise domain and the sample noise domain. Ideally, an NMR experiment should be carried out in the sample noise domain, where the SNR is only limited by the noise originating from the sample itself. Contrarily, in the coil noise dominated regime the losses due to internal coil noise are the limiting factors for the achievable sensitivity. In this case, the SNR can be improved by reducing the internal coil noise, e.g. by means of using cooled or even superconducting RF coils.

For a given field strength, the size of the coil has to be greater than a certain critical value in order to operate in the sample noise domain; this critical coil size decreases with increasing  $B_0$  [33]. Therefore, high-field MRI benefits not only from a higher induced signal but also from the possibility to use miniaturized RF coils in the sample noise domain. In practice, however, the coil size is often determined by the application for which the RF coil is designed and the required field of view (FOV). A compromise between high coil sensitivity and coverage of a large sample surface can be found by using coil arrays, which are discussed in the next section.

## **Chapter II RF Coils and their Characterization**

## II.1. Basic principles

### II.1.1. Resonant circuits

During an MRI experiment, RF signals are transmitted and detected by the NMR probe. An NMR probe is composed of one or several RF coils, the coupling network(s) and the coil housing, which isolates all electronic parts from the patient and provides mechanical stability. RF coils used in NMR are resonant structures. This helps the detection of the relatively small NMR signal because the electromotive force induced in the coil is multiplied by the resonator's quality factor  $Q$  at the output [35].

$$Q = 2\pi \cdot \frac{\text{stored energy}}{\text{dissipated energy per cycle}} = \omega \cdot \frac{\text{stored energy}}{\text{power loss}} = \frac{\omega L}{R} \quad \text{II.1}$$

The coil itself is an inductor with inductance  $L$ . Since the coil wire also exhibits resistive losses  $R$ , energy is not only stored but also dissipated via Ohmic losses.

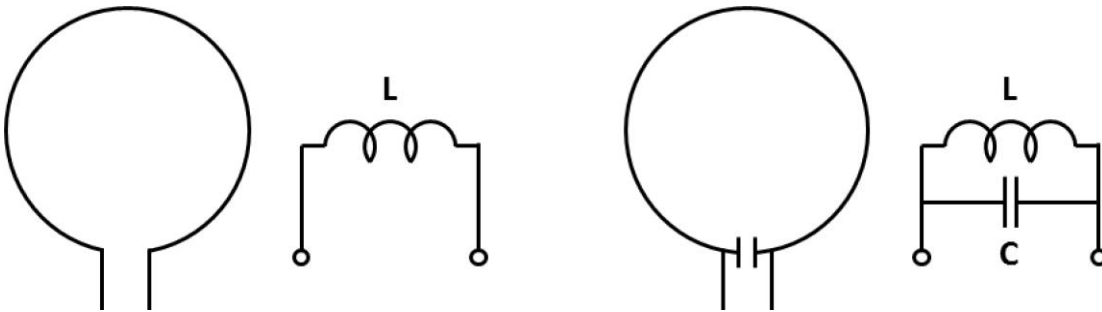


Figure II.1 Basic RF coil and corresponding equivalent circuit

Tuning the coil is generally achieved by placing a capacitor with capacitance  $C$  in parallel to the coil inductor (Figure II.1).  $L$  and  $C$  are selected in a way that the circuit's resonance frequency  $\omega_0$  matches the Larmor frequency  $\omega_L$  of the respective NMR experiment.

$$\omega_0 = \frac{1}{\sqrt{LC}} \quad \text{II.2}$$

The coil's Q-factor can be measured in terms of the width of the resonance peak

$$Q = \frac{f_0}{\Delta f} \quad \text{II.3}$$

where  $f_0$  is the resonance frequency and  $\Delta f$  is the -3 dB bandwidth of the resonance peak. For example, a simple loop coil for 7 T (10 cm diameter, 1.5 mm thick copper wire) has a  $Q$  of approximately 150 when unloaded. The Q-factor may drop by a factor of five or more when the coil is loaded by the sample ( $R = R_C + R_S$ ). A high drop indicates that sample losses strongly dominate over internal coil losses, and that the sensitivity of the NMR experiment cannot be increased by reducing coil noise [36]. Therefore, both the unloaded and loaded  $Q$  should be stated to characterize an RF probe.

### II.1.2. Transmit and receive field of an RF coil

According to Ampere's law, a current passing through a wire generates a magnetic field  $\mathbf{B}_1$ .

$$\int_S \mathbf{J} d\mathbf{S} = \frac{1}{\mu_0} \int_C \mathbf{B}_1 d\mathbf{l} \quad \text{II.4}$$

The  $\mathbf{B}_1$  field of an NMR coil is responsible for tilting the nuclear magnetization into the transverse plane, and determines the sensitivity of the coil in a particular location, according to the principle of reciprocity.  $\mathbf{B}_1$  can be decomposed into the component  $B_{1z}$ , and into two circularly polarized transverse components  $B_1^+$  and  $B_1^-$ , rotating clockwise and counter-clockwise with respect to the static magnetic field  $\mathbf{B}_0$ .

$$B_1^+ = \frac{B_{1x} + iB_{1y}}{2} \quad \text{II.5}$$

$$B_1^- = \frac{B_{1x}^* - iB_{1y}^*}{2}$$

Because the magnetization is only influenced by a magnetic field rotating in the same sense as its precession, only the  $B_1^+$  component of the total  $\mathbf{B}_1$  field causes spin nutation during RF transmission. In contrast, the received signal depends on the counter-rotating field  $B_1^-$  [26]. It

should be noted that the  $B_1^+$  and the  $B_1^-$  field are in general not equal to each other, especially at high frequencies [37].

### II.1.3. Specific absorption rate (SAR)

During transmission a significant amount of the emitted RF power is absorbed by the sample, where it is dissipated in form of heat. Tissue heating is potentially dangerous and is legally constrained for safety reasons. However, it is very complicated to monitor the exact temperature change in the patient tissue during an MRI examination. Therefore, the specific absorption rate (SAR) is used as an approximation to the actual temperature change. SAR is defined as

$$\text{SAR} = \frac{\text{total RF energy dissipated in the sample}}{\text{exposure time} \times \text{sample weight}} \quad \text{II.6}$$

The power dissipated in the sample is given by

$$P = \int \frac{\sigma(\mathbf{r})|\mathbf{E}(\mathbf{r})|^2}{2} d\mathbf{r} \quad \text{II.7}$$

where  $\sigma$  is the electric conductivity of the sample and  $\mathbf{E}$  is the electric field produced by the RF coil. The SAR can then be calculated as

$$\text{SAR} = \frac{\tau}{2T_R} \int \frac{\sigma(\mathbf{r})|\mathbf{E}(\mathbf{r})|^2}{\rho(\mathbf{r})} d\mathbf{r} \quad \text{II.8}$$

where  $\tau/T_R$  is the RF duty cycle, i.e. the fraction of total scan time for which the RF field is present, and  $\rho$  is the mass density of the sample tissue.

Maximum allowable global and local SAR values are stated in the International Electrotechnical Commission (IEC) guideline 60601-2-33. The maximum SAR directly limits the applicable power and therefore poses a limit for the employed RF pulses.

### II.1.4. High frequency effects

The behavior of magnetic and electric fields inside the human body can be computed by solving Maxwell's equations. Maxwell's equations in the Lorenz gauge in a medium with conductivity  $\sigma$ , relative permittivity  $\epsilon$ , and permeability  $\mu$  yield a damped wave equation for magnetic field  $\mathbf{B}$ , electric field  $\mathbf{E}$ , vector potential  $\mathbf{A}$ , and scalar potential  $\phi$ , of the form

$$\nabla^2\Psi + k^2\Psi = 0 \quad \text{II.9}$$

where  $\Psi$  is a general variable, and  $k$  is the complex wave number

$$k^2 = \omega^2\mu\mu_0\epsilon\epsilon_0 - i\omega\mu\mu_0\sigma \quad \text{II.10}$$

Clearly,  $k$  increases with frequency, which can be used to define “low frequency” ( $|ka| \ll 1$ ) and “high frequency” ( $|ka| \gtrsim 1$ ) domain, where  $a$  is the radius of the sample.

For biological samples, the permeability can be assumed to be approximately one ( $\mu \approx 1$ ), and therefore plays a less important role in equation II.10. However, both, the permeability and the conductivity contribute to  $k$ , where the relative contributions are frequency dependent. For example, at 7 T (i.e. 300 MHz for  $^1\text{H}$  nuclei) the wave number  $k = 60 - i20$ , for approximately tissue equivalent relative permittivity ( $\epsilon \approx 80$ ), and electrical conductivity ( $\sigma \approx 1 \text{ S/m}$ ). This shows that neither of the two terms in equation II.10 entirely dominates, and that therefore, both,  $\epsilon$  and  $\sigma$  have to be taken into account to derive the distributions of  $\mathbf{B}_1$  and  $\mathbf{E}$  within the sample [38].

The dielectric permittivity causes the wave length to decrease in dielectric samples, e.g. the human body. At 300 MHz, the wave length in the tissue may be reduced to 10 – 15 cm, which is comparable to the dimensions of most organs of interest in the human body.

$$\lambda_{\text{tissue}} = \frac{1}{\sqrt{\epsilon\mu}} \lambda_{\text{freespace}} \quad \text{II.11}$$

Due to the reduced wave length, the  $\mathbf{B}_1$  field generated inside the sample by the RF coil is greatly inhomogeneous. The symmetry of most commonly used volume probe designs (e.g.

birdcage coil) leads to so-called field-focusing, also referred to as central brightening artifact [39,40], which causes the field at the center of a spherical sample to be much stronger than at the edge. This focusing effect is dampened by the conductivity of the sample. With increasing conductivity, the field at the sample edge rises further and further until it is much greater at the sample surface than at the center, which is a manifestation of the so-called skin effect [38]. The latter condition is, however, not encountered with biological samples within the currently used range of field strengths (whole body scanners up to 10.5 T).

At ultra-high field strength, also the problem of tissue heating becomes more important since SAR increases proportionally to  $B_0^2$  [41]. In addition, the EM fields generated by the RF coil at short wavelength may lead to so-called SAR 'hot spots', and therefore, concentrate the heating effect over a small volume.

## II.2. NMR probe design

Since the field of biomedical NMR is very wide and includes many target anatomies to be investigated in various MR scanners at different field strengths, a large variety of NMR probe designs exists. An NMR probe can be optimized, for example, either to give high detection sensitivity, or to produce a very homogeneous  $B_1$  field during excitation. Also, during the construction of the coil care should be taken that the used materials do not disturb the static magnetic field  $B_0$  and that mechanical stability of the probe is ensured for the respective application [42].

### II.2.1. Volume probes

Volume probes, i.e. probes where the sample is inserted into the probe volume, are widely used for applications which require a very homogeneous RF field, e.g. for well-defined flip-angles over a large ROI. In early NMR experiments, simple loop coils have been wrapped around the sample as RF probes [43], progressing later to solenoids [36] or the saddle coil design [44].

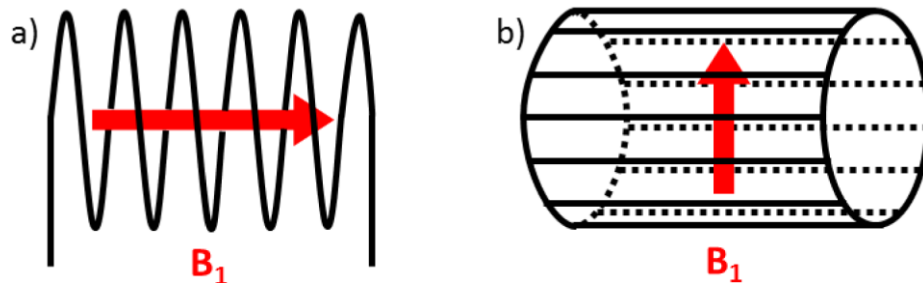


Figure II.2 Commonly used volume coils, a) solenoid, b) birdcage

The solenoid coil is a simple volume probe that is still frequently used, especially for MR microscopy applications. It creates a  $B_1$  field parallel to the coil axis; therefore, the coil has to be placed perpendicular to the static magnetic field  $B_0$  in order to create the required transverse  $B_1$  field. Solenoids are easy to build and they produce an approximately 2-3 fold higher  $B_1$  per unit current in comparison to the saddle [25] or the birdcage coil [45], which is described below. However, solenoids are rarely used for biomedical high field MR



applications, because their self-resonance frequency is too low due to their high inductance and parasitic capacitance across the windings. Further, in most clinical MR systems, the patient is positioned inside the scanner along the  $B_0$  field. In this case, the perpendicular placement of a solenoid coil is problematic, with the exception of smaller anatomical structures that can be positioned accordingly, such as the finger [46], for instance.

One of the most commonly used volume coils in biomedical MRI is the so-called birdcage coil [47]. In contrast to solenoid coils, it provides a transverse  $B_1$  field; therefore, the coil axis should be placed along the static magnetic field  $B_0$  to achieve efficient RF excitation and detection. A birdcage coil has the shape of a cylinder, where rings of wire are placed at the top and the bottom end. These rings are connected to each other by several straight wires, so-called legs, distributed over the cylinder surface. The coil is tuned via discrete capacitors. The way these capacitors are placed on the coil conductors can be used to distinguish three different types of birdcages: the high-pass, the low-pass, and the bandpass. In the high-pass design, the capacitors are placed solely along the end-rings, the low-pass birdcage has its capacitors along the legs, while in the bandpass design capacitors are placed on both, end-rings and legs. The achievable homogeneity of the generated RF field depends on the ratio between length and diameter of the coil cylinder, as well as the number of legs (typically 12 - 24). Practical limitations for the optimization of  $B_1$  homogeneity are the inductive coupling between neighboring legs, which increases with decreasing distance, and that the cylinder surface has to remain transparent for RF flux [42].

### **II.2.2. Surface coils**

Already in early NMR research, it has been reported that the achievable SNR in MRI experiments with a restricted ROI can be increased in comparison to large volume coils by using RF surface coils, which match the size and shape of the investigated anatomical structure [48]. The sensitivity improvement originates from the fact that due to their smaller diameter the received signal amplitude from a sample region close to the surface coil is higher than for a whole-body coil or a large volume coil. Additionally, less noise is coupled to the coil since the surface coil is only loaded by a sub-volume of the sample. However, the

$B_1$  field produced by a surface coil is usually less homogeneous than that of a volume coil, diminishing with increasing distance along the coil axis.

Coil miniaturization is a way to increase the sensitivity of an RF coil as long as sample noise is the dominant noise mechanism (see section I.3.3). This principle has been exploited in several studies, which describe SNR gains using miniaturized RF coils at intermediate and high magnetic field strength [49,50].

In the coil noise domain, SNR can be improved by reducing the internal coil noise. This can be achieved by using cooled copper coils or even superconducting RF coils employing high-temperature superconductors like yttrium-barium-copper compounds ( $YBa_2Cu_3O_{7-\delta}$ ), [33,51]. Most studies have been performed at low or intermediate field strength, as the coil size defining the threshold between sample and coil noise domain decreases with increasing frequency. The superconducting NMR coils themselves are typically self-resonant and consist of a set of inductive loops and interdigitated or distributed capacitance fabricated in monolithic fashion without lumped elements. These coils can be fine-tuned and matched contactless via moveable inductive coupling loops, see section II.3.3.

#### **II.2.2.1. Conventional surface coils**

A conventional surface coil consists of a circular or rectangular copper winding with one or several capacitors distributed around its circumference. The coil inductance is determined by the coil size, which is chosen according to the MR application, the conductor cross-section, and the number of turns. Tuning to the Larmor frequency is achieved by insertion of capacitors. Often several distributed capacitors are used in order to produce a more even current distribution along the loop, and hence, produce a more uniform  $B_1$  field [36]. Distributing capacitors along the loop also equilibrates the coil with respect to conservative electric field. As a rule of thumb, the loop should be segmented by capacitors into sections not longer than one twentieth of the respective wave length.

### II.2.2.2. Monolithic transmission line resonators

This work is concerned with monolithic transmission line resonators (TLRs), also referred to as parallel-plate split ring resonators, which have long been used as NMR surface coils [52,53]. They are composed of two circular conducting bands with either a single turn or multiple turns [54] deposited on both sides of a low-loss dielectric substrate (Figure II.3). Diagonally opposite gaps on the two conductors alter the normal current flow along the transmission line, rendering the whole structure as if it was composed of two closely coupled coils. TLRs are auto-resonant with the possibility of tuning via the coil geometry, where the windings set an equivalent inductance and the capacitive effect is integrated within the substrate.

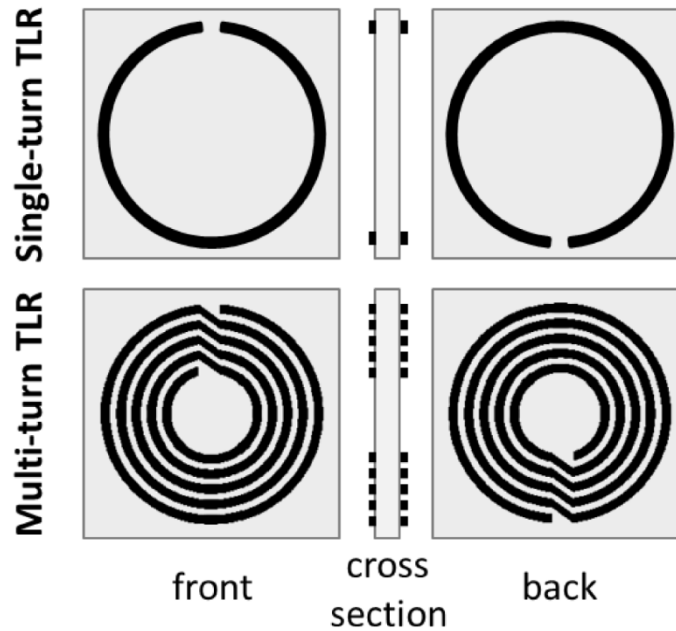


Figure II.3 Single- and multi-turn TLR design

TLRs are fabricated from copper plated dielectric substrates by photolithographic etching. Various types of raw material, i.e. substrates with metal and photo-resistive layer, are commercially available. The selected substrate material should have an electrical conductivity  $\sigma$  very close to zero, a high breakdown voltage, and low dielectric losses, characterized by the loss tangent  $\tan(\delta)$ .

$$\tan \delta = \frac{\varepsilon'}{\varepsilon''} \quad \text{II.12}$$

$$\varepsilon = \varepsilon' + i\varepsilon'' \quad \text{II.13}$$

$\varepsilon'$  and  $\varepsilon''$  are the real and imaginary part of the relative permittivity  $\varepsilon$ , respectively.

In this work, Polytetrafluoroethylene (PTFE, “Teflon”) was used as substrate material for all investigated TLR coils. It has a relative permittivity of 2.0 - 2.2 depending on the particular manufacturing process, a loss tangent of 0.0008 at 1 MHz, and a breakdown voltage greater than 45 kV/mm [55]. Further, Teflon is biocompatible, flexible and light weight, which makes it especially favorable for biomedical MRI. Other frequently used substrate materials for TLRs are FR4, Kapton, and sapphire for superconducting TLRs, for instance.

### II.2.3. Array probes

When large areas are to be covered with small coils, multiple coils in parallel, i.e. phased arrays, can be used [16]. The signal from the individual coils is then combined either as magnitude image, i.e. after the removal of phase information, or in a phase-corrected manner.

As indicated in section I.3.3, small surface coils have higher sensitivity in the vicinity of the coil than a larger coil. This intrinsically higher sensitivity of small coils may be exploited for an extended FOV by using coil arrays [16]. In addition, RF coil arrays permit the use of parallel imaging techniques, which can be employed to speed up MRI acquisitions [17,18], as outlined in section I.2.7. Finally, if the transmit amplitude and phase of each coil element in the array can be adjusted individually,  $B_1^+$  shimming is enabled [56,57]. This can be used, for instance, to achieve a more homogeneous  $B_1^+$  field, and therefore, a more even flip angle distribution in the ROI. Theoretically, RF pulses generating user-defined excitation profiles could also be realized with a single transmit channel; however, in practice, the required RF pulses would be unrealistically long. Parallel transmission techniques [10,58] such as Transmit SENSE provide a way to shorten the spatially selective RF pulses by using multiple transmit coils.

### II.2.3.1. Mutual decoupling in coil arrays

A major technical challenge in coil array design is to keep the individual array elements isolated from each other. Two resonators placed in close vicinity couple strongly to each other. This can be quantified by the mutual impedance. The mutual impedance  $Z_{ij}$  is defined as the voltage  $V_i$  induced in coil element  $i$  by the current  $I_j$  flowing in coil element  $j$ .

$$Z_{ij} = \frac{V_i}{I_j} = R_{ij} + iX_{ij} \quad \text{II.14}$$

Like self-impedance, mutual impedance is composed of a resistive ( $R_{ij}$ ) and a reactive ( $X_{ij}$ ) part. For NMR coils the reactive part is usually inductive. The mutual inductance between coils may induce peak splitting in the resonance spectrum (Figure II.4), which causes sensitivity loss at the Larmor frequency. The mutual resistance introduces noise correlation between the coil elements which leads to an SNR reduction [59].

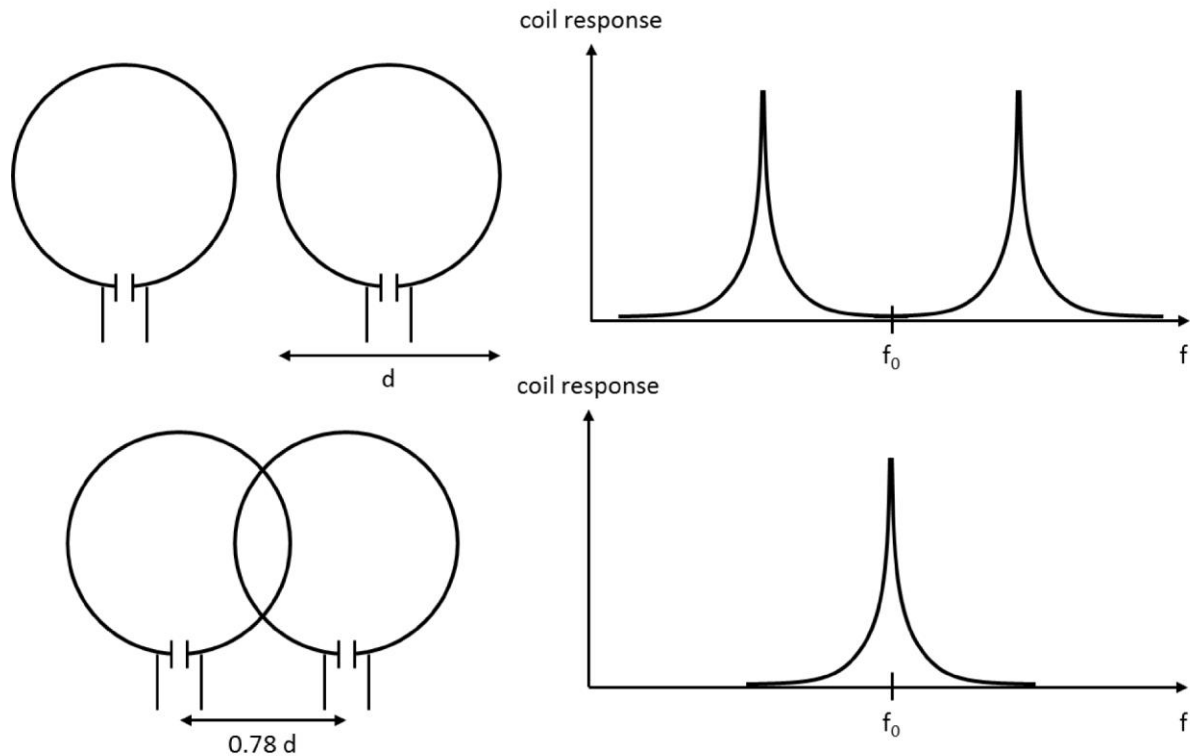


Figure II.4 Mutual decoupling by geometrical overlap

The mutual inductance between loop elements can be canceled by finding the correct overlap for which the net magnetic flux shared by the two coils is zero [16] (Figure II.4). This simple method is frequency independent, and can be applied for nearest neighbor elements in transmit and receive arrays. However, the mutual coupling between next-nearest neighbor coils may still be significant and cannot be canceled by geometric overlap.

An alternative approach to reduce the mutual coupling between coil elements is to reduce the current in each loop and this way the shared magnetic flux. This can be achieved by transforming the input impedance of the preamplifier in a way that it appears as an infinite series resistance in the coil circuit, while at the same time the coil impedance is transformed in a way to achieve noise matching at the preamplifier input [16,60]. This decoupling technique is not limited by the positioning of the coil elements and is widely used for receive arrays, it is, however, not applicable in transmit mode. In transmit arrays the mutual coupling can be reduced with the current source RF amplifier method [61,62], although it is currently not implementable on most commercial MR scanners.

The inductive coupling between array elements can also be reduced by placing LC-components between the elements [63–65]. This concept has been generalized to show that an  $n$ -element array can be mutually decoupled with a suitable  $2n$ -port passive network [66]. A drawback of these decoupling networks is that the achieved decoupling level may strongly depend on the loading of the coil. Nonetheless, this technique is widely used as it does not restrict the relative geometric placement of the individual array elements, and it is applicable in receive as well as in transmit mode.

Several other sophisticated but less frequently used decoupling techniques have been developed for applications where the presented conventional approaches are not applicable. A method that provides a high degree of freedom regarding placement and operation of coil elements is to place a shielding around each coil. This technique is also applicable for other than loop-type coils as for instance strip line elements. However, the unloaded to loaded  $Q$  ratio and also the transmit efficiency can be significantly reduced with this decoupling method [67].

## II.3. Relating the RF probe to the MR scanner

### II.3.1. Power matching and noise matching

MRI experiments are based on the transmission and detection of RF signals via the RF probe. Therefore, it is necessary to connect the RF probe to the power amplifier, and to the receive chain of the MR scanner. In both cases typically coaxial cables with a characteristic impedance of  $50 \Omega$  are used.

During RF transmission, it is important that maximum power is transferred to the NMR coil, and as little power as possible is reflected back into the power amplifier. Maximum power transfer can be achieved if the transmitter, the coil, and the cable have the same impedance  $Z_0$  (typically  $50 \Omega$ ); this is called power matching. A mismatch is undesirable because it makes the transmit chain less efficient, and because the potentially reflected power must be dissipated somewhere.

In the receive case, the signal induced in the coil has to be transferred to the preamplifier without degrading the SNR. The preamplifier itself may add noise to the signal, which can be characterized by its noise factor  $F$ .  $F$  is defined as the relative SNR degradation during signal transfer or amplification [68].

$$F = \frac{SNR_{\text{input}}}{SNR_{\text{output}}} \quad \text{II.15}$$

Often the SNR degradation is characterized in dB scale in terms of the noise figure  $NF$ .

$$NF = 20 \cdot \log(F) \quad \text{II.16}$$

$F$  depends on the frequency of operation and also on the source impedance, i.e., the impedance that the coil presents to the preamplifier. That means that the noise factor is minimal for a unique optimal source impedance  $Z_{\text{opt}}$  [69]. Noise matching consists of transforming the coil impedance to  $Z_{\text{opt}}$ , thus ensuring optimal SNR performance of the preamplifier. Most NMR preamplifiers are calibrated in a way that  $Z_{\text{opt}}$  equals  $50 \Omega$ .

However, the noise matching condition does not necessarily coincide with the power matching condition [60]. For instance, preamplifier decoupling is often implemented in a way that the input impedance of the preamplifiers, i.e. the impedance presented to the coil by the preamplifier, is very low ( $\sim 3 \Omega$ , [16]) and therefore differs strongly from the optimal source impedance  $Z_{opt}$ . In this case, the coil impedance has to be matched to the maximum SNR point, i.e.  $Z_{opt} = 50 \Omega$ , rather than the preamplifier input impedance for optimal SNR performance.

Typically the complex impedance of a loaded NMR probe has a small resistive part, e.g.  $5 \Omega$ , and a positive, i.e. inductive, reactive part ( $20 - 200 \Omega$ ) [70]. Various ways have been proposed to transform this impedance to the required purely resistive  $50 \Omega$ .

### II.3.2. Capacitive matching

It is common practice to use a capacitive tuning and matching network [36,70] between the RF coil and the coaxial cable. A basic tuning and matching network can be constructed with two variable capacitors, one in parallel and one in series with the coil inductance.

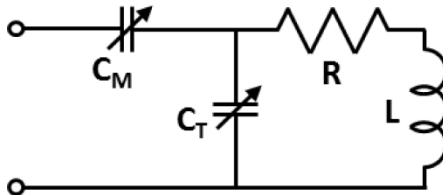


Figure II.5 Basic capacitive tuning and matching network

Using capacitive components for impedance matching has the advantage of introducing less noise to the circuit than with inductive components. A comparison can be performed in terms of the  $Q$ -factor. Real inductors have a  $Q$  around 50 at 300 MHz, whereas high quality capacitors have a  $Q$  of 1000 or more at the same frequency [70]. In this regard it should be also stated that trimmer capacitors in general have lower  $Q$  values than ceramic capacitors with fixed capacitance.



Besides impedance matching, also electrical balance of the coil, i.e. the symmetry with respect to electrical ground, has to be taken into account. When the coil is not electrically balanced, unwanted current pathways (common mode currents) may induce parasitic coupling, or increase dielectric and radiation losses. Using a balanced design the common mode rejection of the circuit is increased, making it much less sensitive to external interference sources [36]. The matching network in Figure II.5 is not electrically balanced; it can be improved by splitting the matching capacitor  $C_M$  into two series capacitors with capacitance  $2C_M$ , which are then connected symmetrically on both legs.

### II.3.3. Inductive matching

Another way to relate the RF coil to the MR spectrometer is to use a coupling loop. This approach has several advantages over capacitive matching [30,71,72]. The coil is intrinsically balanced with respect to electrical fields, tuning and matching adjustments can be made almost independent from each other, and the NMR coil itself can be constructed wireless which is especially advantageous for implanted coils.

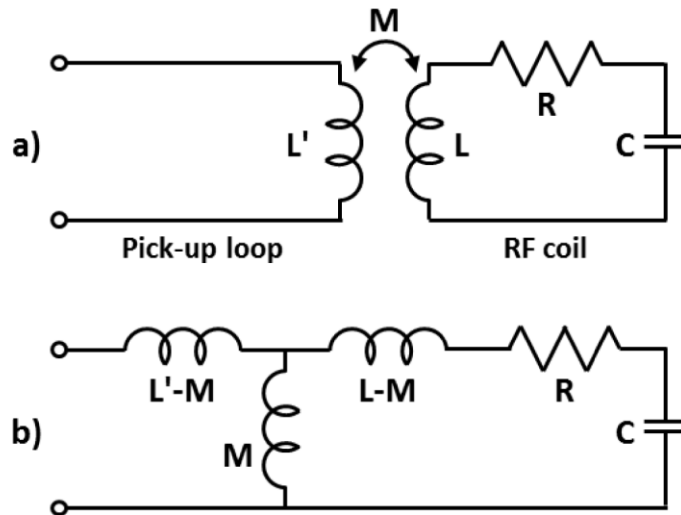


Figure II.6 Equivalent circuits for an inductively matched RF coil

With inductive matching, the coil impedance  $Z$  has to be transformed to  $Z_0 = 50 \Omega$  at the terminals of the coupling loop. The pick-up loop is coupled to the RF coil by magnetic flux

sharing via the coils' mutual inductance  $M$ . For analysis of the inductive matching circuit (Figure II.6a), the transformer can be replaced by a T-circuit as shown in (Figure II.6b).

The proportion of shared magnetic flux is defined by the coupling coefficient  $k$ .

$$k = \frac{M}{\sqrt{L \cdot L'}} \quad \text{II.17}$$

Thereby three different configurations have to be distinguished:

- Under coupling: The coupling loop is placed far away from the coil, resulting in a small  $M$ . The resistive impedance at the pick-up loop terminal is smaller than  $Z_0$ , and matching is impossible.
- Critical coupling: The distance between the coils is adjusted in a way that the transformed impedance is exactly  $Z_0$  at the resonance frequency. The critical coupling coefficient  $k_c$  depends on the Q-factors of both coils.

$$k_c = \frac{1}{\sqrt{Q_{\text{Coil}} \cdot Q_{\text{Pick-up}}}} \quad \text{II.18}$$

- Over coupling: For coupling coefficients higher than  $k_c$  the resistive part of the transformed impedance becomes higher than  $Z_0$ . Then impedance matching can be achieved for two different frequencies, slightly above and below the original resonance frequency. The difference between those frequencies increases with increasing  $k$ . Optimal inductive matching can generally be obtained in a slightly over-coupled mode [70].

In the basic configuration, very fine movements of the pick-up loop with respect to the RF coil are required to adjust the matching, which is mechanically very challenging. In practice, mostly tuned coupling loops [70] are used since this enables to adjust tuning and matching independently from each other [71]. In this configuration, tuning is achieved by varying the probe capacitance  $C$ ; on the other hand, matching is obtained either by adjusting the mutual inductance  $M$  (Figure II.7a) or by varying the pick-up loop capacitance  $C'$  (Figure II.7b). The

latter setup has the advantage of being mechanically more robust because with a fixed mutual inductance no high precision mechanical system is needed to control the distance between pick-up loop and RF coil.

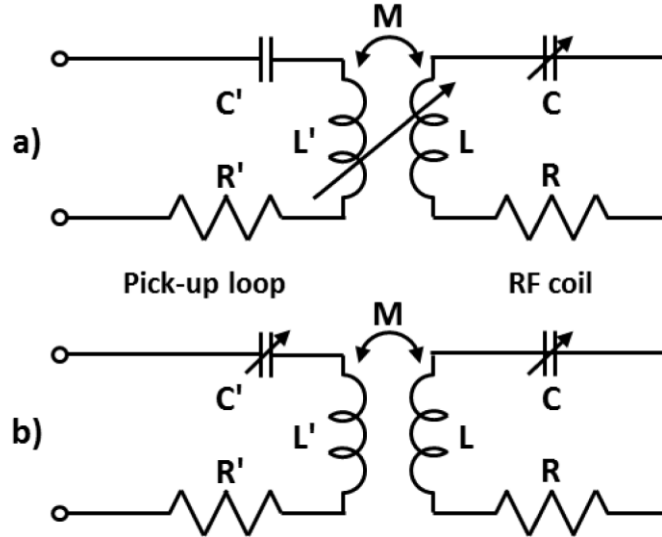


Figure II.7 Inductive matching with a tuned pick-up loop

With inductive matching, also the resistive losses in the pick-up loop ( $R'$ ) have to be taken into account. The noise factor for pick-up loop matching [73] is defined as

$$F = 1 + \frac{\text{Noise power from the pickup loop}}{\text{Noise power from the NMR coil}} \quad \text{II.19}$$

$F$  can be calculated from the following expression [73]

$$F = 1 + \frac{k_c^2}{k^2} + \frac{Q_{\text{Coil}}}{k^2 Q_{\text{Pick-up}}} \left(1 - \frac{f_0^2}{f_L^2}\right)^2 \quad \text{II.20}$$

where  $f_0$  is the resonance frequency of the isolated NMR probe, i.e. without pick-up loop, and  $f_L$  is the Larmor frequency to which the coupled two coil system has to be tuned. Although  $f_0$  and  $f_L$  differ in over-coupled mode, this difference is usually small, and  $F$  is dominated by the ratio of  $k_c$  to  $k$ . To achieve a noise factor close to one at the Larmor frequency,  $k$  must be large as compared to  $k_c$ .

If the inductive matching setup is not carefully configured, the current in the coupling loop may perturb the  $B_1$  field of the RF coil [72]. Strong over-coupling ensures a low current ratio  $I_{\text{Pick-up}}/I_{\text{Coil}}$  over a wide bandwidth to minimize  $B_1$  contribution from the pick-up loop [73].

$$\frac{I_{\text{Pick-up}}}{I_{\text{Coil}}} = \frac{1}{k} \sqrt{\frac{L}{L'}} \left( \frac{f_0^2}{f^2} - 1 + \frac{j}{Q_{\text{Coil}}} \right) \quad \text{II.21}$$

However the effective field contribution from the pick-up loop is also related to the proximity between the pick-up loop windings and the sample. Therefore, for a single inductively matched surface coil a larger pick-up loop placed further away from the NMR coil should be preferred over a smaller closer one (for the same coupling coefficient  $k$ ) [72].

### II.3.4. Baluns and common mode current blocking

The coaxial cable itself is an unbalanced line, and connecting one end of the coil directly to the shield of the cable, e.g. with the capacitive matching network shown in Figure II.5, results in an unbalanced circuit. A balun is a network that converts between a balanced signal (i.e., two signals working against each other and, thus, ground is irrelevant, as at the terminal of the NMR coil) and an unbalanced signal (i.e., a single signal working against ground, as in a coaxial cable). Baluns exist in various forms, e.g. the  $\lambda/2$  balun shown in Figure II.8. They can also be used as impedance transformers in which case they can replace standard capacitive matching networks.

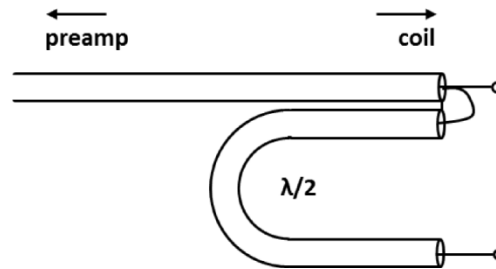


Figure II.8  $\lambda/2$  balun

Another possibility is to reduce (“block”) current flow on the shield of the coaxial cable. Such blocking devices are often called cable traps, some examples are ferrite chokes (not MR

compatible), tank circuits or “bazookas” [70,74], as shown in Figure II.9. As a rule of thumb, the distance between the coil and the first cable trap should be smaller than one-eighth of the resonance wave-length.

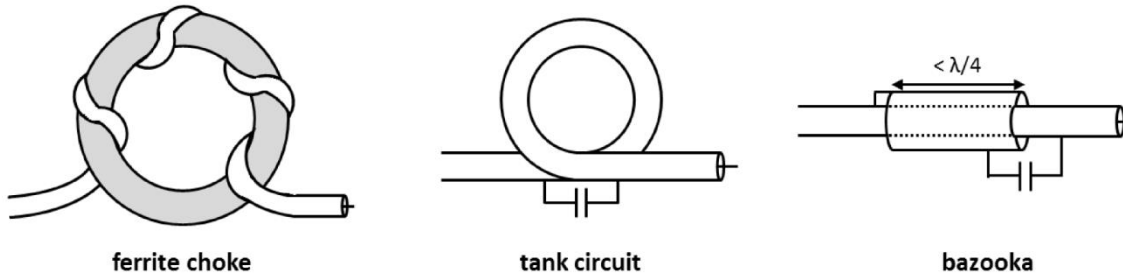


Figure II.9 Three different cable trap designs

### II.3.5. Receive-only probes

Often single surface coils and phased array coils are used only for signal reception. In this case, excitation of the spin signal is achieved with a separate volume coil in order to provide a more homogenous  $B_1^+$  distribution. However, when a surface coil is placed inside a volume probe, the two coils may strongly couple to each other. This coupling has to be avoided by any means since the transmit coil could induce high current in the receive coil during RF transmission, which poses a potential risk for the patient. Further, the transmit field homogeneity may be perturbed by the presence of the receive coil, and sensitivity might be lost during reception due to the mutual coupling between the two coils.

Besides geometric decoupling, the coupling between the two circuits may be reduced by detuning one coil while the other is in use. This can be achieved using a trap circuit in the receive coil and a PIN diode switch [75]. The trap consists of an inductance connected in parallel with one of the coil capacitors, forming a resonance circuit, which presents a high impedance at the resonance frequency, and therefore, blocks current flow in the RF coil. The PIN diode functions as a switch to open and close this parallel resonance circuit and is triggered actively by DC signals generally provided by the MR scanner. Due to the active diode switching, this decoupling method is called active detuning.

In the surface coil, the actively switched PIN diode may also be replaced or supplemented by fast RF diodes, which are switched simply by the induced Tx signal which is much higher than the signal during reception. This is then called passive detuning [76]. Active detuning has advantages over passive detuning because of its greater safety margin and the ability to work with arbitrarily small transmit powers.

## **II.3.6. Additional hardware**

### **II.3.6.1. The preamplifier**

Ideally, the NMR signal induced in the RF coil has to be amplified without degradation of SNR. This is the purpose of the preamplifier; modern models achieve a noise figure  $NF$  of 0.3 dB. As the signal induced in the coil is small, the preamplifier should be placed in close vicinity to the coil in order to minimize losses in the connecting cable. In commercial NMR probes the preamplifiers are often integrated in the coil housing. The preamplifier gain has to be high enough so that additional noise introduced by further sections of the receive chain does not significantly reduce the SNR; typically values between 25 and 30 dB are achieved.

### **II.3.6.1. Transmit/Receive switching**

The MRI signal is usually processed in two separate paths: the transmit (Tx) and the receive (Rx) path. When the same RF coil is used for both, transmission and reception, the correct signal path must be switched by a so-called transmit/receive (T/R) switch (Figure II.10).

The transmit signal is typically eight orders of magnitude higher than the receive signal; if the preamplifier in the Rx path were exposed to the transmit signal it would be permanently damaged. Typically, T/R switches used in NMR are based on PIN diodes [77] and quarter-wavelength transmission lines, which act as impedance transformers [70].

During transmission both PIN diode switches ( $D_1$ ,  $D_2$ ) are closed. Closing  $D_1$  allows the transmit signal to pass to the coil, while closing  $D_2$  short circuits the preamplifier input to ground. The quarter-wave transmission line element converts the low impedance of this short circuit (ideally 0) to a very high impedance (ideally  $\infty$ ) at the other end of the transmission line. This high impedance prevents the transmit signal from passing to the preamplifier.

During reception both PIN diode switches are opened. This way, the signal received in the coil can directly pass to the preamplifier.

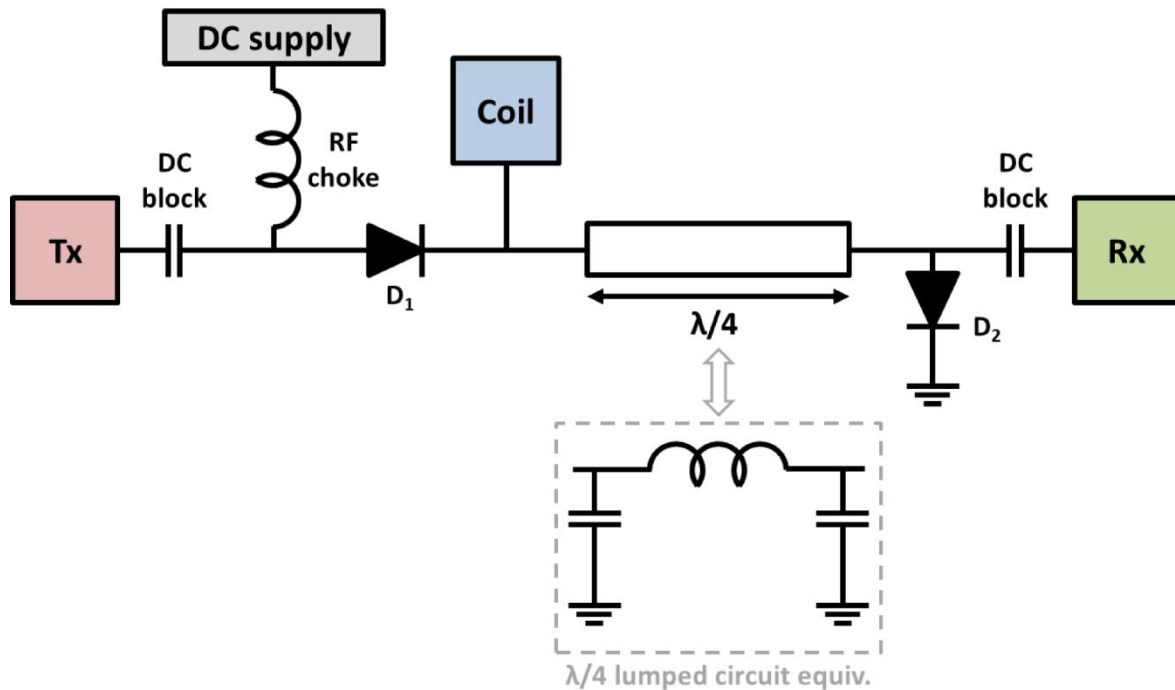


Figure II.10 Quarter-wavelength T/R switch

### II.3.6.2. Splitting the transmit power

Most commercial MR scanners are equipped with a single transmit channel only. To operate an array of transmit coils, it is necessary to split up the delivered transmit power to the individual channels. One simple method of achieving this is a Wilkinson power divider.

Figure II.11 shows the equivalent circuit of a two-way Wilkinson power divider in its lumped element configuration. It splits an input signal into two output signals with the same phase and amplitude, or it combines two equally phased signals into one in the opposite direction. The power splitter is based on quarter-wave transmission lines with characteristic impedance of  $\sqrt{2}$ -times the port impedance  $Z_0$  (typically 50  $\Omega$ ), and a resistor of 2-times  $Z_0$ , which ensures impedance matching for all three ports and isolates port 2 from port 3.

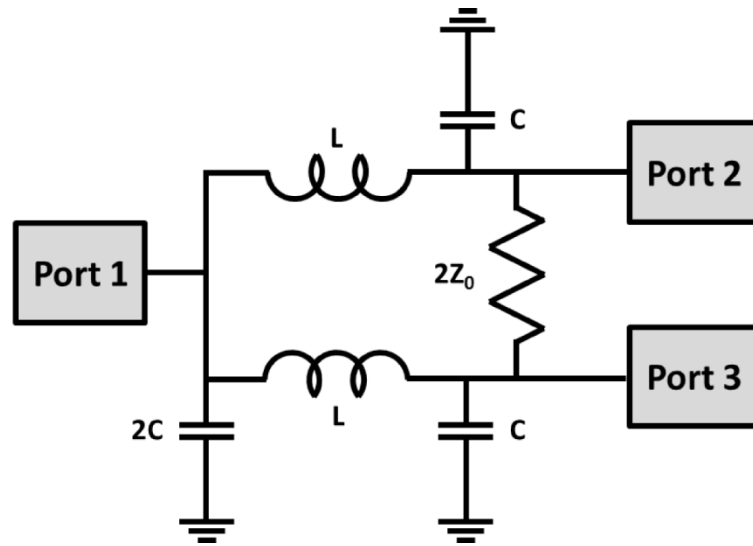


Figure II.11 Two-way lumped element Wilkinson power divider

If the transmit signal has to be split into more than two ways, either a cascade of two-way dividers or an n-way divider can be used. Further, it is possible to build asymmetric Wilkinson power dividers for certain applications.

Recently, the concept of parallel RF transmission (pTx) with array coils has been introduced [58] and several research MR scanners giving access to this technology are available at intermediate and high field strengths. With pTx technology, the transmit phase and amplitude of each transmit channel can be controlled individually. This gives access to active  $B_1^+$  shimming, and parallel excitation for shortened spatially selective RF pulses. In this case all necessary hardware is integrated in the MR scanner and no external power splitters are needed if the number of array elements does not exceed the number of transmit channels.



## II.4. Numerical and analytical RF coil modeling

### II.4.1. Full-wave electromagnetic simulation

Full-wave electromagnetic modeling of NMR probes is widely used in high and ultra-high field MRI [37], where the quasi-static approximation applicable at low field is no longer valid (section II.1.4). It allows the coil and the sample, and if necessary also the magnet bore, to be analyzed as a single system. In combination with realistic body models and suitable post-processing tools, full-wave electromagnetic simulations (EMS) can provide distributions of electric and magnetic fields inside the human body by solving Maxwell's equations. The simulated fields can then be used to calculate SNR and SAR maps.

The most widely used techniques are the finite difference time domain (FDTD) method [78], the finite element method (FEM) [79,80], and the method of moments (MoM) [81]. Further, the advantages of the different methods can be combined by so-called hybrid solvers [82]. FDTD is a grid-based time-domain technique, which solves Maxwell's equations directly in their partial differential equation form. This is the method used in this work, and is described in more detail in the following section.

### II.4.2. Principles of FDTD

The FDTD method was introduced by Yee [78], and is based on the discretization of Maxwell's curl equations.

$$\nabla \times \mathbf{E} = -\mu_0 \frac{\partial \mathbf{H}}{\partial t} \quad \text{II.22}$$

$$\nabla \times \mathbf{H} = \varepsilon \frac{\partial \mathbf{E}}{\partial t} + \sigma \mathbf{E} + \mathbf{J} \quad \text{II.23}$$

These equations may be replaced by a set of finite difference equations, which can then be solved iteratively. For this purpose, central-difference approximations are used to discretize equations II.22 and II.23 in space and time ( $\Delta x$ ,  $\Delta y$ ,  $\Delta z$ ,  $\Delta t$ ).

In order to solve the finite difference equations, the problem space is subdivided into unit cells (“Yee cells”) of appropriate size. Suitable dielectric properties (relative permeability  $\mu$ , relative permittivity  $\epsilon$ , and electric conductivity  $\sigma$ ) are assigned to each cell. For an FDTD simulation, also excitation sources have to be specified. Depending on the type of situation to be simulated, the excitation source can be a plane wave or a current or voltage source placed on the conductive elements of the RF coil.

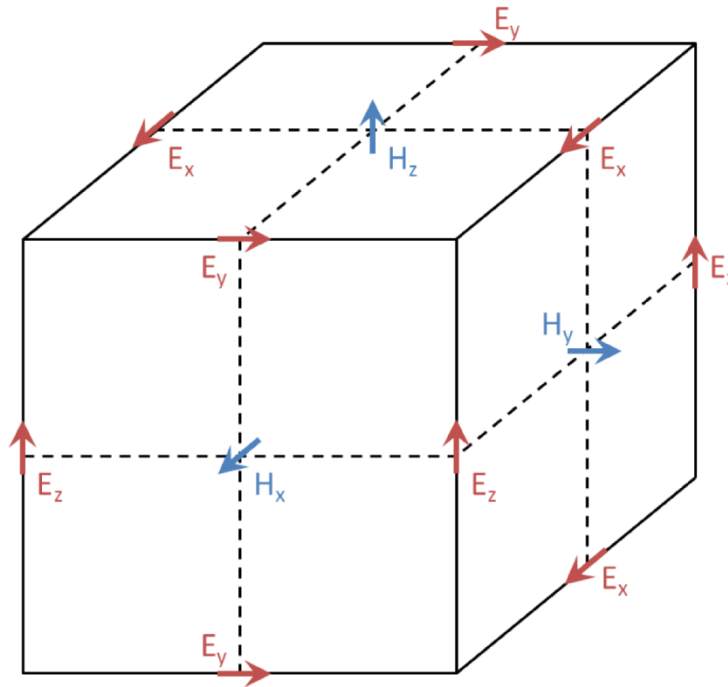


Figure II.12 Yee cell, illustrating the offset between E- and H-field

As shown in Figure II.12, the electric field components are assigned to the center of each edge, while the magnetic field components are assigned to the center of each face of a cell. This way, the electric field can be calculated using the surrounding magnetic field components and vice versa. After applying suitable initial and boundary conditions, the E-field vector components are solved first. Then, the H-field vector components in the same spatial volume are solved at the next instant in time. From that on, at any given instant in time and space, the FDTD algorithm will calculate both electric and magnetic fields. These calculations are repeated until the desired numerical stability is achieved. At its end, an FDTD simulation yields the E- and H-field distribution throughout the whole problem space.

The FDTD method is simple to implement [83], and several commercial software packages suitable for NMR probes are available.

A disadvantage of FDTD is that the simulation mesh has to be composed of regular cuboid cells. This can pose a problem when modeling structures with curved surfaces. In this case, a so-called stair-casing approach is applied to adapt the mesh to the sample geometry. This stair-casing can, however, introduce significant errors into the solution, unless the mesh resolution is increased to accurately resolve the variations in the geometric features, increasing the memory requirements and run time. Further, since the electromagnetic field generated by an RF coil radiates infinitely into space, suitable boundary conditions surrounding and limiting the original problem space have to be defined. Usually, absorbing boundary conditions in the form of 3D perfectly matched layers (PMLs) [84] are used in the FDTD simulations. This way, considerable computational time and memory resources can be saved.

### II.4.3. Combining FDTD and circuit co-simulation

Usually, an RF coil model also contains lumped components, e.g. tuning and matching capacitors. Including these components in the 3D EMS may lead to unreasonably long simulation times if a human body model is included in the simulation and tuning and matching is performed using the 3D EMS software. In this case, the full 3D models of the coil and the sample have to be simulated for each iterative tuning step. This limitation can be overcome by combining 3D EMS with RF circuit co-simulations, which are computationally less demanding [85,86].

For circuit co-simulation [87], all lumped component networks (e.g. matching networks, tuning and decoupling capacitors) are replaced by equivalent ports with an impedance  $Z$  (typically  $50 \Omega$  for NMR applications), after the coil has been modeled in the 3D EMS software. Then the FDTD solver is run with one port activated at a time, while the remaining ports are terminated by a  $50 \Omega$  load. These simulations of the multiport coil design provide prototypes for the electric ( $\mathbf{E}$ ) and the magnetic ( $\mathbf{H}$ , where  $\mathbf{B}_1 = \mu_0\mu\mathbf{H}$ ) field of the coil, as well as the multiport scattering matrix, i.e. the reflection and transmission scattering

parameters of all ports in the system. The S-parameter matrix is then used by the RF circuit simulator, where the lumped element networks are defined and connected to the corresponding ports of the S-parameter simulation. Suitable values for tuning and matching capacitors, decoupling networks, or other lumped components can be calculated using optimization procedures in the co-simulation tool solely based on the S-parameter data. Afterwards, the electrical properties of the circuit (e.g. current and voltage for circuit nodes) are simulated for the optimized component values. The current ( $I$ ) and voltage ( $U$ ) values thus obtained for each node of the S-parameter simulation are used to calculate the voltage  $V$  across each equivalent port.

$$V^j(\omega) = I^j(\omega) \cdot Z^j(\omega) - U^j(\omega) \quad \text{II.24}$$

where  $j$  is the port index. Instead of voltage, most full-wave EMS tools define the port excitation in terms of power  $P$  and phase  $\varphi$ .

$$P^j(\omega) = \frac{|V^j(\omega) \cdot (V^j(\omega))^* / (8 Z^j(\omega))|}{P_{\text{prototype}}^j} \quad \text{II.25}$$

$$\varphi^j(\omega) = \text{phase}(V^j(\omega)) - \varphi_{\text{prototype}}^j \quad \text{II.26}$$

$P_{\text{prototype}}^j$  and  $\varphi_{\text{prototype}}^j$  are the power and phase defined for the initial 3D EMS run. The final E- and B<sub>1</sub>-field of the coil setup including lumped components can be calculated as linear superposition of the prototype fields with  $P^j$  and  $\varphi^j$  as weighting factors.

$$\mathbf{B}_1 = \sum_j^N \mathbf{B}_1^j \cdot \sqrt{P^j(\omega)} \cdot e^{i\varphi^j(\omega)} \quad \text{II.27}$$

$$\mathbf{E}_1 = \sum_j^N \mathbf{E}_1^j \cdot \sqrt{P^j(\omega)} \cdot e^{i\varphi^j(\omega)} \quad \text{II.28}$$

where  $N$  is the total number of ports in the model.

The fields calculated this way are exactly the same as the fields that would have been obtained with the lumped components included in the 3D EMS [87]. Therefore, circuit co-simulation enables the estimation of the electric and magnetic fields and other dependant properties (e.g. SAR, receive sensitivity, transmit efficiency) for various tune/match/decoupling conditions based on only one set of full-wave 3D EMS, together with as many RF circuit simulations as required.

#### **II.4.4. Modeling of TLRs**

TLRs give access to coil miniaturization and form-fitting due to their auto-resonant and monolithic nature. However, these properties also evoke the need for specialized modeling methods which enable the determination of the resonance frequency as a function of the geometric parameters of the TLR. Further, the effect of the surroundings, e.g. the sample or the coil housing, also should be taken into account during the design process.

An analytical formulation for the resonance condition based on transmission line models has been proposed [53,54] and is commonly used for predicting the resonance frequency of TLRs. The accuracy of this model in comparison to experimental data is in the range of 10 %. Possible explanations for these deviations are for instance an inaccuracy in the estimation of the characteristic transmission line impedance or inductance, and limitations in the applicability of the transmission line model. Nonetheless, more accurate means for predicting the resonance frequency of TLRs would be desirable. Additionally, the analytical model does not account for any material surrounding the TLR. Therefore, full-wave electromagnetic modeling in form of FDTD simulation has been recently introduced for TLRs [88].

Here, first the analytical model for calculating the resonance frequency of a TLR is described. Then some considerations about the implementation of FDTD simulation for TLRs are given.

### II.4.4.1. Analytical Model for TLRs

An analytical model for the resonance condition of TLRs is given by Gonord et al. for single turn structures [53] and was extended to multiple turns by Serfaty et al. [54].

$$\frac{L_{\text{tot}}\omega_0}{4N_g Z_0} \tan\left(\frac{\omega_0\sqrt{\varepsilon} l_f}{4N_g c}\right) = 1 \quad \text{II.29}$$

The angular resonance frequency  $\omega_0$  is implicitly given in terms of the TLR's equivalent inductance  $L_{\text{tot}}$ , the length of one conducting band  $l_f$  and the parallel-plate transmission line characteristic impedance  $Z_0$ , which is a function of the conductor width  $w$ , the substrate thickness  $h$  and its dielectric constant  $\varepsilon$ .  $c$  denotes the vacuum speed of light and  $N_g$  the number of gaps per conductor. The derivation of this equation using the differential and common mode model for transmission lines is given in appendix section A.1.

$L_{\text{tot}}$ , is given by the sum of the individual inductances  $L_i$  of all  $N$  turns and their respective mutual inductances  $M_{ij}$ .

$$L_{\text{tot}} = \sum_{i=1}^N \left( L_i + 2 \sum_{j=i+1}^N M_{ij} \right) \quad \text{II.30}$$

The inductance of a flat circular loop with mean radius  $r$  and width  $w$  can be calculated by the following expression [54].

$$L_i = \frac{4r_i}{\mu_0} \left[ \ln\left(\frac{8r_i}{w}\right) - \frac{1}{2} + \frac{w^2}{96r_i^2} \left( \ln\left(\frac{8r_i}{w}\right) + \frac{43}{12} \right) \right] \quad \text{II.31}$$

A formula to compute the mutual inductance  $M$  between two circular loops with both lateral and angular misalignments based on the filament method, where the coils are replaced by infinitesimal filaments, has been proposed by Grover [89]. For the special case of no angular misalignment, the original expression can be simplified; for coil radii  $r_i$  and  $r_j$ , a vertical displacement  $a$  between coil centers and a horizontal displacement  $d$ , the following expression is obtained [90]:

$$M_{ij} = \frac{2\mu_0}{\pi} \sqrt{r_i r_j} \int_0^\pi \frac{\left(1 - \frac{d}{r_j} \cos \varphi\right) \Psi(k)}{k\sqrt{V^3}} d\varphi \quad \text{II.32}$$

$$V = \sqrt{1 + \frac{d^2}{r_j^2} - 2 \frac{d}{r_j} \cos \varphi} \quad \text{II.33}$$

$$k^2 = \frac{4V \frac{r_j}{r_i}}{\left(1 + V \frac{r_j}{r_i}\right)^2 + \frac{a^2}{r_i^2}} \quad \text{II.34}$$

$$\Psi(k) = \left(1 - \frac{k^2}{2}\right) K[k] - E[k] \quad \text{II.35}$$

In the last equation,  $K[k]$  and  $E[k]$  are the complete elliptic integrals of first and second kind:

$$K[k] = \int_0^\pi \frac{1}{\sqrt{1 - k^2 \sin^2 \theta}} d\theta \quad \text{and} \quad E[k] = \int_0^\pi \sqrt{1 - k^2 \sin^2 \theta} d\theta \quad \text{II.36}$$

To calculate the mutual inductance between turns of a single TLR, the horizontal displacement  $d$  can be set to zero because all turns are coaxially aligned. The characteristic impedance  $Z_0$  of a parallel plate transmission line can be calculated with semi-empirical models [91] for two different geometric configurations:

Wide band approximation ( $w > h$ ):

$$Z_0 = \frac{120\pi}{\sqrt{\varepsilon}} \left[ \frac{w}{h} + 0.441 + \frac{\varepsilon + 1}{2\pi\varepsilon} \left( \ln \left( \frac{w}{h} + 0.94 \right) + 1.452 \right) + 0.082 \frac{\varepsilon - 1}{\varepsilon^2} \right]^{-1} \quad \text{II.37}$$

Narrow band approximation ( $w < h$ ):

$$Z_0 = 120\pi \sqrt{\frac{2}{\varepsilon + 1}} \left[ \ln \left( \frac{4w}{h} \right) + \frac{1}{8} \left( \frac{w}{h} \right)^2 - \frac{\varepsilon - 1}{2(\varepsilon + 1)} \left( 0.451 + \frac{0.241}{\varepsilon} \right) \right] \quad \text{II.38}$$

In previous work [92], a Matlab toolbox has been implemented, which allows one to find a TLR design for a given Larmor frequency of interest. The toolbox returns sets of geometric parameters, including the number of turns  $N$ , the external TLR diameter  $d_{\text{ext}}$ , the conductor width  $w$ , the spacing between turns  $p$ , the substrate thickness  $h$ , and the substrate permittivity  $\epsilon$ , which may be limited by the user. For instance, when designing a TLR for a certain application, the field strength, and thus the Larmor frequency, as well as the coil size are a priori set; depending on availability, often also the substrate permittivity and thickness are fixed, or at least limited to several discrete values. That leaves the number of turns, the conductor width and the spacing between turns as degrees of freedom for TLR tuning.

#### II.4.4.2. FDTD simulation of TLRs

When performing 3D EMS of TLRs several additional aspects have to be taken into account in comparison to conventional RF coils. Besides the magnetic and electric fields that are commonly simulated, for TLRs also the self-resonance frequency and the current density distribution along the transmission line are of interest. While the calculation of the current density is readily available as an option in most simulation software packages, designing a TLR for a certain Larmor frequency is more difficult. Since the resonance frequency depends on the TLR geometry, this analysis cannot be performed by circuit co-simulation, but relies on a recalculation of the complete 3D model (TLR and sample) for each modification of the TLR geometry. For TLRs, this is particularly time-consuming because the resonators have a relatively high quality factor. In this case, the time-domain simulation may take a very long to reach a steady state [93]. In contrast, conventional loop coils are not resonant when the respective lumped elements are replaced by 50- $\Omega$ -ports and, thus, require much shorter run times. Additionally, due to the thin dielectric substrate (several 100  $\mu\text{m}$ ) a very fine mesh resolution has to be chosen for TLRs, which further increases the simulation time. Therefore, FDTD simulations are only useful for TLR design in combination with analytical modeling. Starting values for the geometric parameters are determined using the analytical formula; then, a few fine adjustments are performed using the FDTD solver.

Information about how FDTD simulations were implemented for TLRs in this work will be given in section III.3.1.5.



## II.5. Experimental characterization of RF coils

### II.5.1. Bench measurements

#### II.5.1.1. Network analyzer

The typical tool to analyze an RF network is a vector network analyzer (VNA), which can be used to measure amplitude and phase properties as a function of frequency; in contrast to a scalar network analyzer (SNA), which only measures amplitude properties. Basically, a network analyzer is composed of a signal generator, a test set, one or more receivers, and a processing and display unit. The signal generator provides a test signal; the test set routes the test signal to the investigated circuit (device under test, DUT) and the input signal to the receivers, where the actual measurement is performed. VNAs need at least two receivers because a reference channel is required to determine the signal phase. The received signal is then processed and displayed in a suitable format, e.g. on a linear or logarithmic scale or in form of a Smith chart. Commonly, VNAs are used to measure S-parameters since reflection and transmission of electrical networks can be easily measured at high frequencies. Bench measurements in this work were performed using two- and four-port VNAs (E5061B and E5071C, Agilent, Santa Clara, USA).

#### II.5.1.2. S-Parameters

The scattering matrix of a network can be used to establish a relationship between incident and reflected voltage waves  $V$ . The complex S-parameters of a two-port network are defined in the following way.

$$\begin{aligned} S_{11} &= \frac{V_{1b}}{V_{1f}} \Big|_{V_{2f}=0} & S_{21} &= \frac{V_{2b}}{V_{1f}} \Big|_{V_{2f}=0} \\ S_{12} &= \frac{V_{1b}}{V_{2f}} \Big|_{V_{1f}=0} & S_{22} &= \frac{V_{2b}}{V_{2f}} \Big|_{V_{1f}=0} \end{aligned} \tag{II.39}$$

The subscripts 1 and 2 refer to the respective ports and the subscripts f and b distinguish forward and backward voltages (Figure II.13); In  $S_{ij}$  the first subscript refers to the receiving

port, and the second to the transmitting port. This definition can be extended to an arbitrary number of ports. The diagonal elements of the S-matrix are measured in reflection, and correspond to the respective voltage reflection coefficients  $\rho$ . All off-diagonal elements are measured in transmission, and correspond to the respective linear voltage gains  $T/E$ .



Figure II.13 Two-port network

Often, S-parameters are given in dB scale.

$$S_{ij}|_{\text{dB}} = 20\log_{10}(S_{ij}|_{\text{linear}}) \quad \text{and} \quad S_{ij}|_{\text{linear}} = 10^{S_{ij}|_{\text{dB}}/20} \quad \text{II.40}$$

### II.5.1.3. Double-loop probe method

Characteristics of an RF coil, such as the resonance frequency and the Q-factor, can be measured on the bench using sniffer loops. The most commonly used types of sniffer loops are the double-loop probe and the single-loop probe.

The double-loop probe consists of two identical loops decoupled from each other. This is commonly achieved by geometrical overlap. The probe is placed in the vicinity of the investigated RF coil, each loop is connected to a port of the VNA, and a transmission measurement is performed. The signal transmitted through one of the loops induces a current in the RF coil; the voltage induced in the second loop by the current flowing in the RF coil is then recorded. The resonance frequency and the Q-factor can be deduced from the resulting  $S_{21}$  curve by determining the curve maximum and the respective -3 dB bandwidth. Further, the coil sensitivity is proportional to the square root of the voltage gain at the resonance frequency [94]:

$$\frac{B_1}{\sqrt{P}} = \frac{\sqrt{Z_0}}{\omega_0 S} \sqrt{\frac{T}{E}} \quad \text{II.41}$$

where  $P$  is the supplied electrical power, and  $S$  is the surface area of the investigated RF coil.

In order to accurately use this method, the probe loops have to be sufficiently small in comparison to the RF coil, so as to not perturb the  $B_1$  field of the coil. Also, the probe has to be positioned in a way that the coupling between each of the loops and the investigated RF coil is identical. Further, if the coupling between the double-loop probe and the RF coil is too strong, an equivalent resistance is added to the coil, leading to an error in the measured Q-factor. This effect can be assumed negligible if  $S_{21}$  is below -40 dB, which establishes an upper limit for the voltage gain that should be used. In practice, also a lower limit exists, because the two loop probes cannot be perfectly decoupled and signal is still coupled between the loops (typically in the order of -80 dB). The  $S_{21}$  value at the resonance frequency should exceed this reference level by approximately +20 dB [94].

#### II.5.1.4. Single-loop probe method

With the single-loop probe method [95] the sniffer probe consists of only a single loop, and a reflection measurement is performed. This method is based on two separate measurements of the reflection coefficient of the probe, one with the sniffer coil alone in free space ( $\rho_0$ ) and the other in the presence of the investigated RF coil ( $\rho_c$ ). The first measured curve is subtracted from the second one in order to yield a compensated reflection coefficient  $\rho_{\text{comp}} = \rho_c - \rho_0$ . Also with this method, the sensitivity of the investigated RF coil may be measured.

$$\frac{B_1}{\sqrt{P}} = \frac{R + R_0}{\omega_0 S} \sqrt{\frac{2\rho_{\text{comp}}}{2R_0 - (R + R_0) \cdot \rho_{\text{comp}}}} \quad \text{II.42}$$

$R_0$  is the input resistance of the VNA, typically 50  $\Omega$ , and  $R$  is the resistance of the RF coil.

The resonance frequency and the Q-factor can be extracted from the resulting (compensated)  $S_{11}$  curve. As for the double-loop probe method, the influence of the sniffer loop on the

Q-measurement can be assumed negligible if the  $S_{11}$  value at resonance is below -40 dB; if this condition is not fulfilled, the initially determined Q-value may be corrected.

$$Q = \frac{Q_{\text{initial}}}{1 - \rho_{\text{comp}}} \quad \text{II.43}$$

The single-loop probe method is easier to implement than the double-loop probe method, because it does not rely on mutually decoupled loops. Also, the used sniffer loop can be very small, which enables the characterization of miniaturized RF coils. This method was used primarily in the presented work to analyze the studied TLRs.

## **II.5.2. MR Imaging Experiments**

### **II.5.2.1. MR scanners**

The most significant part of an MR system is the main magnet. The static magnetic field should have very high spatial homogeneity and good temporal stability. Modern high-field systems use superconducting magnets to achieve field strengths  $\geq 3$  T. The bore of the magnet contains the shim coils, used to homogenize the static magnetic field in presence of the sample, and the gradient coils for signal localization.

In this work, most MRI experiments were carried out on a 7 T whole-body scanner (Magnetom 7 T MRI, Siemens Medical Solutions, Erlangen, Germany) and on a 4.7 T small animal scanner (BioSpec USR47/40, Bruker BioSpin, Billerica, USA). The 7 T scanner is equipped with a SC72d gradient coil with maximum gradient strength of 70 mT/m and slew rate of 200 T/m/s, one RF transmit channel for  $^1\text{H}$  measurements, one transmit channel for other nuclei, and 32 receive channels. The 4.7 T scanner is equipped with a single transmit and receive channel for  $^1\text{H}$  imaging only.

### II.5.2.2. Imaging sequences

Before in vivo imaging tests on healthy volunteers or patients can be performed with a newly developed RF coil, the coil's performance has to be evaluated on suitable test objects, so-called phantoms.

A first basic test for the coil is to acquire an MR image of a homogenous sample. Since spin echo sequences are very sensitive to  $B_1$  inhomogeneities, gradient echo (GRE) sequences are better suited for the characterization of surface coils [96]. More advanced imaging experiments can be performed, for instance with the coil form-fitted to a phantom with non-planar surface, or imaging a phantom with internal structure.

Further, it is desirable to know the  $B_1$  distribution produced by the RF coil. Several different methods to map the flip angle distribution in a sample have been proposed [97], which can be used to calculate the  $B_1$  field according to equation I.22. Among these methods, the most commonly used is the double-angle method (DAM) [98], which uses the ratio of two images with two different nominal flip angles  $\alpha$  and  $2\alpha$ . If a GRE sequence is used, the signal amplitude of the first image is proportional to  $\sin(\alpha)$ , and that of the second image to  $\sin(2\alpha)$ , respectively. Taking the ratio  $r$  of the two acquisitions allows one to calculate the flip angle.

$$r = \frac{\sin(\alpha)}{\sin(2\alpha)} = \frac{1}{2\cos(\alpha)} \quad \text{II.44}$$

With DAM, flip angles from  $90^\circ$  to  $180^\circ$  give magnitude ratios equal to those obtained for flip angles between  $0^\circ$  and  $90^\circ$ , symmetric about  $90^\circ$ ; therefore it is only valid for flip angles between  $0^\circ$  and  $90^\circ$ . However, by taking into account the phase information from the two acquisitions, flip angles from  $0^\circ$  to  $180^\circ$  may be mapped [98,99].

DAM has been shown to give robust results and can be straight-forwardly implemented. A drawback of this technique is, however, that it takes rather long to acquire flip angle maps since a  $T_R \geq 5 T_1$  is needed so as to allow a full relaxation of the sample magnetization before each excitation. To improve time efficiency, several alternative flip angle mapping techniques based on magnitude [100,101] and phase information [102–105] have been proposed.

The method used in this work is called saturated Turbo FLASH (satTFL) [101]. It relies on the acquisition of two images: a proton density (PD) weighted image for signal normalization with signal intensity  $S_0$ , and a preconditioned image acquired directly after a slice-selective saturation RF pulse with signal intensity  $S_{\text{sat}}$ . A turbo fast low-angle-shot (Turbo FLASH) sequence is used for image readout. The flip angle can be calculated from the ratio of the two images.

$$\alpha = \arccos\left(\frac{S_{\text{sat}}}{S_0}\right) \quad \text{II.45}$$

## **Chapter III Development, Implementation and Evaluation of a Flexible TLR Array**

This chapter is a reproduction of a full article about the developed TLR array published in the journal *Magnetic Resonance in Medicine* [106]. (Kriegl, R., Ginefri, J.C., Poirier-Quinot, M., Darrasse, L., Goluch, S., Kuehne, A., Moser, E., Laistler, E., *Novel inductive decoupling technique for flexible transceiver arrays of monolithic transmission line resonators*. Magn Reson Med, 2014, doi: 10.1002/mrm.25260)

## III.1. Abstract

### *Purpose*

This article presents a novel inductive decoupling technique for form-fitting coil arrays of monolithic transmission line resonators, which target biomedical applications requiring high signal-to-noise ratio over a large field of view to image anatomical structures varying in size and shape from patient to patient.

### *Methods*

Individual transmission line resonator elements are mutually decoupled using magnetic flux sharing by overlapping annexes. This decoupling technique was evaluated by electromagnetic simulations and bench measurements for two- and four-element arrays, comparing single- and double-gap transmission line resonator designs, combined either with a basic capacitive matching scheme or inductive pickup loop matching. The best performing array was used in 7T MRI experiments demonstrating its form-fitting ability and parallel imaging potential.

### *Results*

The inductively matched double-gap transmission line resonator array provided the best decoupling efficiency in simulations and bench measurements ( $< -15$  dB). The decoupling and parallel imaging performance proved robust against mechanical deformation of the array.

### *Conclusion*

The presented decoupling technique combines the robustness of conventional overlap decoupling regarding coil loading and operating frequency with the extended field of view of nonoverlapped coils. While demonstrated on four-element arrays, it can be easily expanded to fabricate readily decoupled form-fitting 2D arrays with an arbitrary number of elements in a single etching process.



## III.2. Introduction

Many biomedical applications of MRI on humans and small animals require high image resolution, together with high signal-to-noise ratio (SNR) and reasonably short acquisition time. From an instrumental point of view, these requirements call for highly sensitive radio-frequency RF probes adapted in size and shape to the region of interest. To achieve this, several strategies known to improve detection sensitivity and speed can be combined, such as operating at high field, using arrays of small sized RF coils, and using flexible materials for coil fabrication to enable form-fitting of the coil to the target region.

Applying a higher static magnetic field strength is one of the most common strategies in NMR research to increase the amount of detectable nuclear magnetization, and thus, to achieve high spatial resolution with sufficiently high SNR [107–109]. Currently, the highest field strength available for human whole-body MRI is 9.4 T, with head scanners up to 10.5 T.

The use of small surface coils in the regime of sample dominated noise enables strong sensitivity improvement because it provides both, stronger magnetic coupling with the sample and noise reduction due to the smaller volume of tissue visible for the coil [48,110].

The concept of coil miniaturization is of particular interest for high field ( $3 \text{ T} \leq B_0 < 7 \text{ T}$ ), and ultrahigh field ( $\geq 7 \text{ T}$ ) applications and has been used to improve the SNR in several studies [49,50], as the coil size defining the threshold between sample and coil noise domain decreases with increasing frequency. For instance, at 300 MHz, i.e. the proton Larmor frequency at 7 T, this threshold should be reached for a coil diameter of 12 mm [33].

Mechanical flexibility of the RF detection system is advantageous for imaging samples with nonplanar surfaces or anatomical regions that can vary in shape and size from one subject to the other. Form-fitting RF coils to the sample improves the magnetic coupling between sample and coil, provides a higher filling factor and better RF transmission efficiency, and thus, leads to a significant SNR gain [111].

RF coil arrays have several advantages over large single element coils for imaging large anatomical regions. In receive mode, arrays can achieve a large field of view (FOV) while

preserving the intrinsically high detection sensitivity of small coils [16]. Combined with parallel imaging techniques they allow for accelerated image acquisition [17,18]. In addition, in transmit mode, coil arrays give access to  $B_1^+$  shimming [56,57], enabling homogenization or specific shaping of the transmit RF field. This provides a way to compensate for transmit field inhomogeneity occurring at high field due to the shorter wavelength at high Larmor frequency, which usually induces undesired spatial variation of image contrast and intensity. Finally, the concept of parallel excitation permits to shorten the duration of applied spatially selective RF pulses, thus further, speeding up the MRI experiment [10,58].

While efficient principles and techniques are available for these strategies when followed individually, combining all of them to develop a flexible transceiver array composed of small sized coils for high field MRI evokes several technical constraints as well as more fundamental issues.

Standard coil technology using lumped resistive (R), inductive (L), and capacitive (C) components imposes practical limits on the design and fabrication of miniaturized flexible RF devices. This is due to the rigidity of the coils themselves and to the minimum space required by discrete capacitors. Furthermore, even for coils fabricated on flexible substrate or made of semi-rigid copper, the use of lumped capacitors involves rigid solder joints that might crack upon bending, may cause susceptibility artifacts (despite the use of nonmagnetic capacitors), and induces electrical stray fields increasing dielectric losses [42]. This is especially important at ultrahigh field, where multiple lumped capacitors per coil are needed to generate a uniform current distribution along the loop [36]. These constraints can be overcome by the concept of monolithic transmission line resonators (TLRs) [52,54]. TLRs consist of two circular conducting bands intersected by diagonally opposite gaps and deposited on both sides of a low-loss dielectric substrate, which may be flexible. They are auto-resonant and can be tuned over a wide range of NMR frequencies without the use of lumped elements by adjusting the geometrical parameters of the coil, such as substrate thickness and permittivity, or conductor width. After fabrication the TLR's resonance frequency is fixed; however, appropriate fine-tuning under variable loading conditions can be achieved by resonant inductive matching. The  $B_1$  field of the TLR is generated by the

common mode current, given by the sum of the currents flowing in the two conductors. This current is intrinsically constant even if the length of the rings is comparable to the wavelength [53]. With the TLR design, in comparison to standard RLC coils, dielectric losses are reduced, the RF homogeneity is improved [112], and, when combined with an inductive coupling technique, no solder joints on the coil are needed.

A major technical challenge in coil array design is the mutual decoupling between individual coil elements. Conventional decoupling techniques use either geometrical overlap [16], with the drawback of reduced overall FOV and higher g-factors for parallel imaging due to the overlapping sensitivity profiles. Another decoupling strategy includes LC-networks between nonoverlapping coils [63,65], with the disadvantage of frequency and load-dependent decoupling efficiency. Some authors proposed strategies to decouple physically separated coils by magnetic flux sharing to combine the advantages of overlap and LC-network decoupling. Avdievich and Hetherington [113] used a pair of overlapping annex loops with opposite winding orientation connected in series with two neighboring surface coil elements. Constantinides and Angeli [114] placed closed copper loops proximal to the array, partially overlapping with the mutually interacting surface coils, and thereby eliminating the magnetic coupling. Low-impedance preamplifiers are widely used for inter-element decoupling in receiver arrays [16]. In transmit arrays, the mutual coupling can be reduced with the current source RF amplifier method [61,62], although it is currently not available for most MRI systems.

However, the above decoupling techniques are not well suited for double-sided monolithic structures. They are either restricted to standard single layer coils, using lumped elements, and therefore contradict the monolithic feature of TLRs (e.g. LC-component decoupling), or they require three or more conductive layers, which implies a more complex fabrication process and also complicates handling after fabrication (i.e., existing inductive methods). Furthermore, none of them is readily implementable for flexible coil arrays. Hence, no flexible array of TLRs exists so far due to the lack of a suitable decoupling strategy.

The goal of this work is the development of an original transceiver array composed of small monolithic TLRs fabricated on flexible substrate for MRI at 7 T. To this end, a novel decoupling technique suitable for TLR arrays is proposed. This work aims at establishing the proof of concept that the new decoupling technique combined with monolithic design and microtechnological processes can be used to produce flexible two-dimensional arrays of TLRs with an arbitrary number of elements that enhance the RF detection sensitivity.

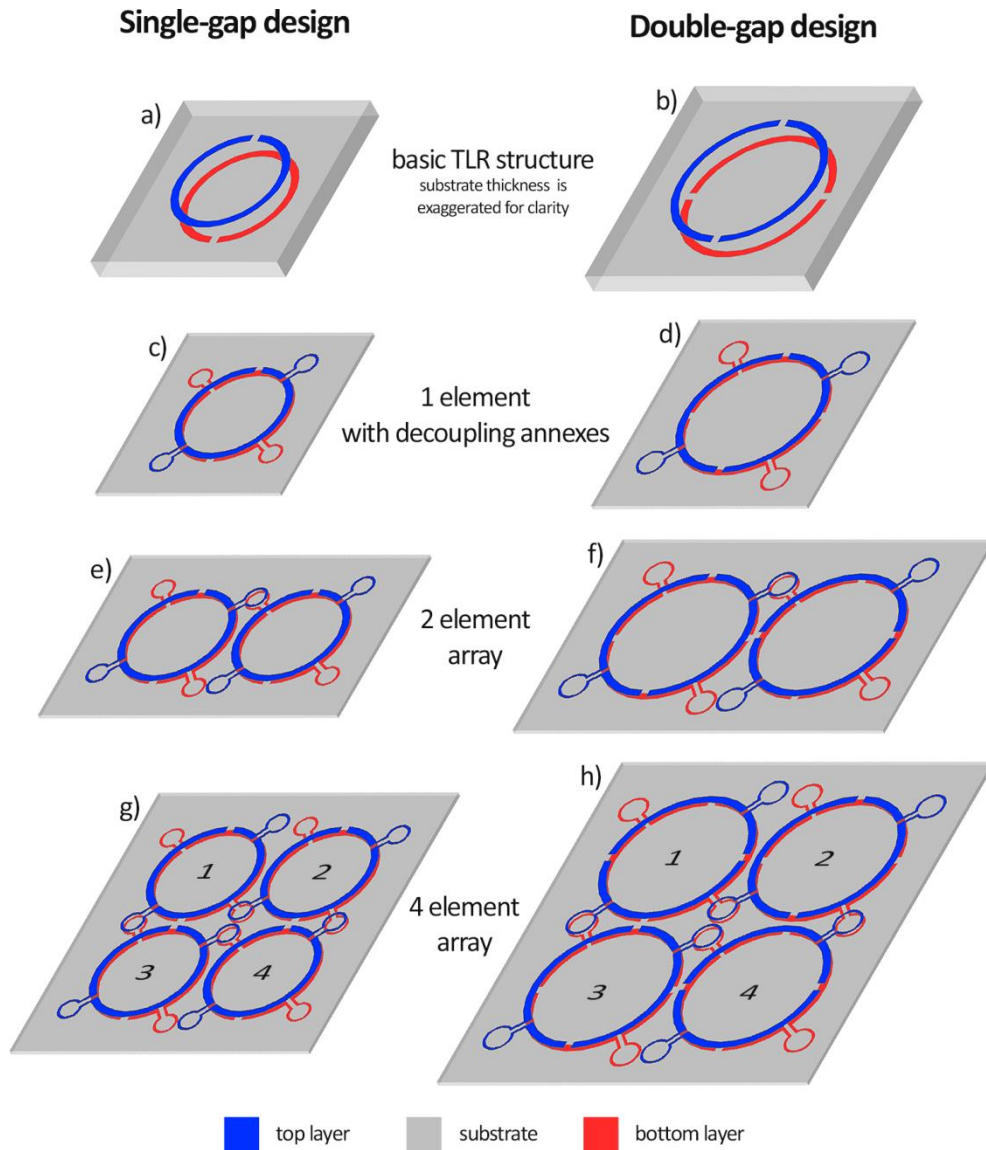


**Figure III.1 Single- and double-gap TLR designs.** Basic TLR designs (a, b), single elements with decoupling annexes (c, d), two-element (e, f) and four-element (g, h) arrays are shown. The substrate thickness in (a) and (b) is not to scale but adjusted for better visibility of the gaps. Note the gap positioning for the double-gap arrays (f, h).

## III.3. Methods

### III.3.1. Design and Simulation

#### III.3.1.1. Novel Decoupling Technique for TLR Arrays

To decouple the elements within an array of TLRs, the basic TLR geometry (Figure III.1 a,b) is extended by small circular annexes connected in series with the main windings (Figure III.1 c,d). Neighboring elements are decoupled by overlapping a front-sided annex of one element with a back-sided annex of the other element (Figure III.1 e,f). Four annexes per TLR permit decoupling from nearest neighbors in 2D-arrays (Figure III.1 g,h) [115].

The coil arrays investigated in this study were composed of single-turn TLRs fabricated on flexible Teflon substrate providing low dielectric losses. Two different TLR geometries were compared, the first design being a 30-mm single-gap TLR self-resonating well above the Larmor frequency of interest, i.e. 297.2 MHz, and to be tuned and matched capacitively. For the second design, the geometric parameters of a 40-mm double-gap TLR were chosen in a way to closely approach the Larmor frequency, with an accuracy of a few MHz, to completely avoid lumped element tuning. This coil could then be fine-tuned and matched inductively with a coupling loop.

Exact geometric parameters of single TLR elements and arrays are given in the results section (Table III.1).

#### III.3.1.2. Matching Networks

Capacitive matching networks consisted of a variable tuning capacitor (6.5 – 30 pF) and two series matching capacitors (6.5 – 30 pF) connected in symmetric configuration between the tuning capacitor and the coaxial feed cable. The question, how a TLR can be optimally matched capacitively to the receiver has not been answered yet. Here, a configuration was chosen, where the tuning capacitor is connected in parallel to the coil capacitance, as in a conventional RLC coil circuit. In the case of a TLR, the coil capacitance is distributed across the substrate and, hence, the feed points were positioned on either side of the TLR. The feed

point position along the winding was chosen to achieve the highest voltage across the two conductors, which is at a gap on one side and in the center of the conductor on the other side (Figure III.2 a).

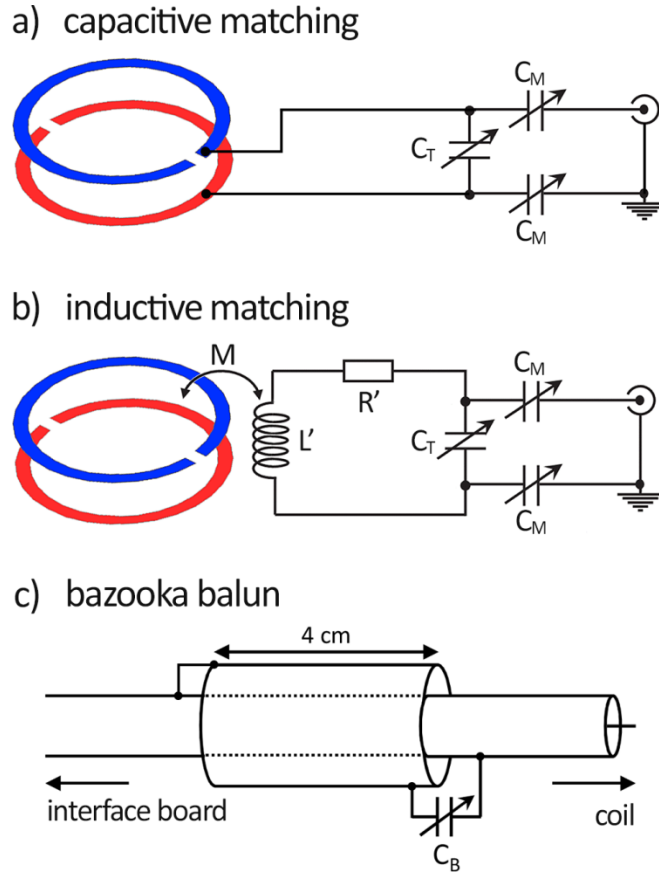


**Figure III.2 Impedance matching schemes for TLRs.** The TLRs are shown on the left side; electrical equivalent circuits of the capacitive matching network ( $C_T$ ,  $C_M = 6.5 - 30$  pF) (a) and the inductive matching ( $C_T$ ,  $C_M = 3 - 10$  pF) setup (b) are drawn on the right side.  $R'$  and  $L'$  refer to the equivalent resistance and inductance of the pickup loop and  $M$  is the mutual inductance between the TLR and the pickup loop.  $C_T$  and  $C_M$  are the tuning and matching capacitors, respectively. In (c) a sketch of the shortened bazooka balun is shown ( $C_B = 24.8 - 32$  pF).

For inductive matching, pickup loops were placed at a distance of 6.5 mm above each TLR. The pickup loops were tuned and matched with lumped element capacitors (Figure III.2 b;  $C_T$ ,  $C_M = 3 - 10$  pF). Each pair of TLR and pickup loop was operated in over-coupled mode to permit fine-tuning [70], since the free resonance frequency of the fabricated TLRs was few

MHz above the Larmor frequency. To shift the lower resonance peak of the coupled two-coil system to the Larmor frequency, the pickup loop had to be tuned above the free resonance frequency of the TLR (Figure III.3).

To investigate the effect of mutual coupling between pickup loops on the overall decoupling efficiency, the coupling between two neighboring inductively matched double-gap TLRs, was simulated for pickup loop diameters of 10 - 30 mm in 5 mm steps.

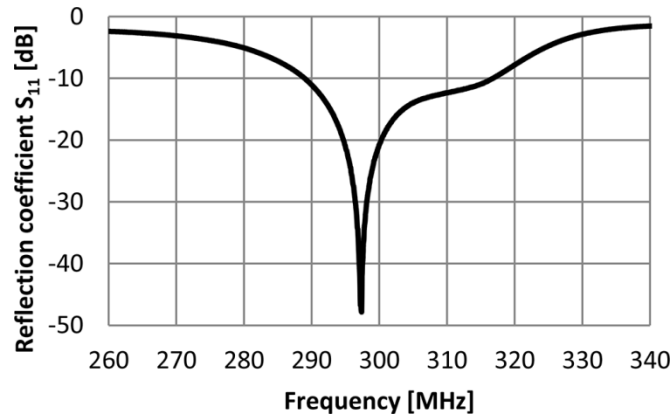


**Figure III.3 Typical  $S_{11}$  response of the over-coupled system of TLR and pickup loop.** The reflection coefficient,  $S_{11}$ , of a double-gap TLR loaded by the torso phantom and matched with a 15-mm pickup loop was measured on the bench. The low frequency peak is tuned to the Larmor frequency of 297.2 MHz (7 T), where the system is matched to 50  $\Omega$ .

### III.3.1.3. Decoupling Performance

The size of the decoupling annexes was optimized for single- and double-gap TLR designs by simulating the transmission scattering parameter  $S_{21}$  of two neighboring elements as a function of the annex diameter. For each annex size, the TLRs were tuned and matched by circuit cosimulation before recording the  $S_{21}$  values. The annex size resulting in the best isolation between neighboring channels was considered optimal. The width of the conducting bands forming the decoupling annexes was reduced in comparison to the width of the main winding and set to 0.8 mm as the space for placing the annexes in four-element arrays is limited (Figure III.1 g,h).

After predicting the resonance frequencies for the basic TLR designs with an analytical model (Eq. IV.1), the shift in resonance frequency induced by the decoupling annexes was accounted for by 3D electromagnetic simulations (EMS) for finding the final TLR geometries (Results section, Table III.1).

The single element TLR designs, annex sizes and pickup loop diameters as determined in the previous steps, were used to demonstrate the decoupling technique in four-element arrays with the individual elements arranged to form a square with an interelement distance of 2 mm. The decoupling efficiency in arrays of single- and double-gap TLRs, each with either capacitive or inductive matching, was compared by simulating the full S-parameter matrices. To explain variations in decoupling efficiency between the different configurations, current density distributions in single TLR elements were simulated at the resonance frequency [116].

#### III.3.1.4. Specific Absorption Rate

To evaluate how adding the decoupling annexes influences the performance of the TLRs in terms of specific absorption rate (SAR), local unaveraged SAR distributions were derived from EMS for single TLR elements with and without decoupling annexes, and for a four-element array decoupled by overlapping annexes (All channels were driven with the same phase and amplitude). Post-processing was performed using a dedicated toolbox (SimOpTx, Research Studio Austria, MedUni Vienna, Austria) using local power correlation matrices [58,117] computed by an ultrafast convolution based SAR averaging algorithm [118].

#### III.3.1.5. Simulation Tools

Starting values for the geometrical parameters of the TLR coils were determined using an analytical model for the resonance condition of TLRs (Eq. III.1) [53],

$$\frac{L_{\text{tot}}\omega_0}{4n_g Z_0} \tan\left(\frac{\omega_0\sqrt{\epsilon}l_f}{4n_g c}\right) = 1 \quad \text{III.1}$$

with the angular resonance frequency  $\omega_0$ , the coil's equivalent inductance  $L_{\text{tot}}$ , the length of one conducting band  $l_f$  and the parallel-plate transmission line characteristic impedance  $Z_0$ ,



which is a function of the conductor width  $w$ , the substrate thickness  $h$  and its dielectric constant  $\epsilon$ .  $c$  denotes the vacuum speed of light and  $n_g$  the number of gaps per conductor.  $L_{tot}$ , which is the sum of the individual inductances of the windings on both sides of the substrate and their respective mutual inductance, as well as  $Z_0$  can be calculated with semi-empirical models [54].

TLR geometries and decoupling efficiency were studied by full wave 3D EMS (XFDTD 7.3, Remcom, State College, PA) in combination with circuit cosimulation (ADS, Agilent, Santa Clara, CA). For 3D EMS a basic mesh resolution of  $2 \times 2 \times 2 \text{ mm}^3$  was used. In the vicinity of the coil, the resolution in the coil plane was increased to 0.5 mm for S-parameter simulations and to 0.25 mm for current density simulations; the resolution along the coil axis inside the substrate was set to half the substrate thickness. The XACT-mesh technology allowing for conformal modeling [119] embedded in the simulation software was enabled for improved meshing accuracy. A rectangular block phantom with the electric and magnetic properties of muscle tissue (0.72 S/m conductivity, 64 relative permittivity) placed 5 mm below the coil was used as load in all EMS. The phantom was 5 cm thick and its lateral dimensions were chosen in a way that the phantom exceeds the simulated single TLR element, two-element or four-element array by 5 cm. Reduced sample dimensions were chosen in comparison to bench and MR measurements (see next section) to save simulations time; it was verified that results were not substantially altered by this simplification. For rapid tuning and matching, the corresponding capacitors were modeled as  $50 \Omega$  ports in 3D EMS and the resulting S-parameters were postprocessed using circuit co-simulation [87]. Current density simulation data were analyzed using Matlab (Mathworks, Natick, MA).

### III.3.2. Hardware and Phantoms

For step-to-step characterization of the novel TLR designs, single coil elements with and without annexes, as well as two- and four-element arrays of single- and double-gap design were fabricated. Single-gap TLRs were etched in-house from double-sided CuFlon® microwave substrate (Polyflon Company, Norwalk, CT); double-gap structures were fabricated by a third party with standard photolithographic techniques (db electronic, Daniel Boeck SAS, Saint-Louis, France). A copper layer thickness of 18  $\mu\text{m}$  was used in both cases,

substrate thicknesses of 510  $\mu\text{m}$  (single-gap), and 127  $\mu\text{m}$  (double-gap), were used as indicated in Table 1. The pickup loops were etched from standard 1.5 mm thick FR4 printed circuit board material. Nonmagnetic trimmer capacitors (Murata Manufacturing Company, Kyoto, Japan) were used and shortened “bazooka” type baluns (Fig. 2c) were placed on the coaxial cables at a distance smaller than one eighth of the wavelength from the coils to reduce shield currents.

Bench measurements were performed using a four port vector network analyzer (E5071C, Agilent, Santa Clara, CA).

For MR imaging, one of the four tested four-element arrays was selected based on bench measurements and simulation results. MRI experiments were carried out on a 7T whole-body MRI system (Magnetom 7 T MRI, Siemens Medical Solutions, Erlangen, Germany) equipped with a SC72d gradient coil with maximum gradient strength of 70 mT/m and slew rate of 200 T/m/s. All coil elements were used in transmit/receive mode, driven with the same amplitude and phase during transmission. Additional hardware, including power splitters, transmit-receive switches, and low-noise preamplifiers were placed on a separate interface board.

For bench and MRI experiments with the TLRs in planar configuration, a torso phantom with dimensions and electromagnetic properties as specified in the ASTM F2182-11a standard was used. The phantom is box-shaped (65 x 42 x 9  $\text{cm}^3$ ) and filled with 25 L polyacrylic acid gel. To test the ability of form-fitting and the applicability for various target regions, the before selected four-element array was wrapped onto a cylindrical phantom (7.5 cm diameter, 17.5 cm long) filled with the same gel, representing, for example, a human arm or lower leg. Further, to investigate the performance of the developed array when loaded less than by the phantoms, a kiwano fruit (*Cucumis metuliferus*) was used in bench and MRI experiments mimicking, for instance, wrist or small animal loading conditions. In addition, the tuning and matching capability as well as the decoupling performance of the selected array were evaluated on the bench when it was placed on the torso of a volunteer (male, 39 years, body

mass index = 23 kg/m<sup>2</sup>). For all configurations, 5 mm thick acrylic glass was located between sample and TLR array.

### III.3.3. Bench Measurements

#### III.3.3.1. Decoupling Performance

On the workbench the decoupling efficiency was evaluated by measuring the transmission scattering parameters of two- and four-element arrays of single- and double-gap TLRs. S-parameter matrices were recorded at the Larmor frequency after a typical impedance match better than -30 dB had been achieved for all elements. From these measurements and from simulation results, the array configuration showing the best decoupling efficiency was chosen for further experimental evaluation.

To select a suitable pickup loop size for the inductive matching setup, the coupling of neighboring inductively matched double-gap TLRs in two-element arrays was measured for pickup loop diameters from 10 to 30 mm in 5 mm steps. Bench measurements were compared to the results from EMS.

#### III.3.3.2. Form-fitting

The selected array was wrapped on an acrylic glass former suitable for experiments with the cylindrical phantom and the kiwano fruit. Tuning and matching capacitors were adjusted and full S-parameter matrices were measured to evaluate the matching and decoupling performance in form-fitted configuration.

#### III.3.3.3. Pickup Loop Noise Factor

The noise degradation associated with pickup loop matching [73] was studied as a function of pickup loop size by calculating the noise factor  $F$  for single double-gap TLR elements loaded by the torso phantom:

$$F = 1 + \frac{k_c^2}{k^2} + \frac{Q_{\text{TLR}}}{k^2 Q_P} \left( 1 - \frac{f_0^2}{f_L^2} \right)^2 \quad \text{III.2}$$

with the coupling coefficient  $k$

$$k = \frac{1}{2} \left( \frac{f_P}{f_0} + \frac{f_0}{f_P} \right) \cdot \sqrt{\left( \frac{f_2^2 - f_1^2}{f_2^2 + f_1^2} \right)^2 - \left( \frac{f_P^2 - f_0^2}{f_P^2 + f_0^2} \right)^2} \quad \text{III.3}$$

and the critical coupling coefficient  $k_c$

$$k_c = \frac{1}{\sqrt{Q_{\text{TLR}} \cdot Q_P}} \quad \text{III.4}$$

These equations include the resonance frequency of the isolated TLR  $f_0$ , the lower ( $f_1$ ) and the higher resonance frequency ( $f_2$ ) of the over-coupled system of TLR and pickup loop (see Supporting Information Fig. S1), and the Larmor frequency  $f_L$ .  $Q_{\text{TLR}}$  and  $Q_P$  denote the isolated quality factors of the TLR when loaded with the torso phantom and the pickup loop, respectively.

#### III.3.3.4. Influence of the Decoupling Annexes

The influence of the decoupling annexes on the coils' resonance frequencies and quality factors was evaluated by comparing isolated double-gap elements with and without annexes. Measurements were done in unloaded configuration and when the coils were loaded by the torso phantom using the single-loop probe method [95], while not connected to a matching network. The influence of the single-loop probe was considered negligible when the reflection coefficient measured at its terminal was  $< -40$  dB.

### III.3.4. MRI Experiments

#### III.3.4.1. Preparatory Measurements

To examine the  $B_1$  field distortion potentially induced by the pickup loops [72], MR measurements with a single, inductively matched, double-gap TLR were performed. Transversal 2D gradient echo (GRE) images ( $T_R/T_E = 140$  ms/7.74 ms,  $0.375 \times 0.375$  mm<sup>2</sup> resolution, 1 mm slice thickness,  $256 \times 128$  matrix) with a flip angle  $>180^\circ$  close to the TLR were acquired using the five different pickup loops placed 6.5 mm above the TLR, and

compared to those acquired using a 30-mm pickup loop placed at a distance of 20 mm, for which the induced distortion is assumed to be negligible [72].

The pickup loop diameter, for which the best compromise between preserved decoupling efficiency, low noise degradation and low  $B_1$  field distortion is achieved, was selected for further experiments.

### **III.3.4.2. Noise Correlation and Parallel Imaging Performance**

The parallel imaging performance of the selected array in planar and bent configuration was evaluated in terms of the GRAPPA g-factor applying the pseudomultiple replica method [120] and off-line GRAPPA reconstruction as described by Breuer et al. [121]. Therefore, noise-only data, for computing the noise correlation matrix, and fully encoded 2D GRE images ( $T_R/T_E = 500$  ms/7.74 ms,  $80^\circ$  nominal flip angle,  $0.52 \times 0.52$  mm<sup>2</sup> in-plane resolution, 1 mm slice thickness) of the cylindrical (transversal slices) and the torso phantom (transversal and coronal slices) were acquired. Acceleration factors of  $R = 1$  (no acceleration),  $R = 2$ , and  $R = 3$ , were mimicked during reconstruction by eliminating not required phase encoding steps. Resulting g-factors were computed for sum-of-squares combined images. To compare the parallel imaging performance in flat and bent array configuration, mean and maximum g-factors were calculated for an elliptical region of interest (ROI) (major axis 60 mm, minor axis 40 mm) drawn on transversal images of both, the torso and the cylindrical phantom.

### **III.3.4.3. High Resolution MRI**

High-resolution images of the kiwano fruit were acquired with the selected array in form-fitted configuration applying a 3D GRE sequence ( $T_R/T_E = 150$  ms/6.56 ms,  $76 \times 84$  mm<sup>2</sup> FOV,  $220 \times 220$   $\mu\text{m}^2$  in-plane resolution, 52 slices, 1 mm slice thickness, GRAPPA with  $R = 2 \times 2$ ,  $T_{\text{acq}} = 7$  min 15 sec).

## III.4. Results

### III.4.1. Coil Geometries and Matching Setup

The geometrical parameters of the fabricated single TLR elements and four-element arrays including the optimized annex sizes are summarized in Table III.1. The table also provides simulated and measured resonance frequencies, measured  $Q$  factors for the TLRs in unloaded condition and when they are loaded by the torso phantom, and the comparison of the double-gap TLRs' RF characteristics with and without decoupling annexes.

Single TLR element	$d_{\text{ext}}$ [mm]	$w$ [mm]	$h$ [ $\mu\text{m}$ ]	$\epsilon$	$a_{\text{ext}}$ [mm]	$w_{\text{an}}$ [mm]	$l_{\text{an}}$ [mm]	$f_0$ 3D EMS [MHz]	$f_0$ unloaded [MHz]	$f_0$ loaded [MHz]	$Q$ unloaded	$Q$ loaded
Single-gap	30	2.0	510	2.05	6.4	0.8	2.0	413.7	423.4	416.0	250	33
Double-gap	40	2.1	127	2.2	8.0	0.8	2.7	307.9	315.7	310.0	280	30
Double-gap no annexes	40	2.1	127	2.2	-	-	-	344.0	339.7	335.0	370	29
4-element array	inter-element spacing			square comprising 4 elements without annexes				square comprising 4 elements with annexes				
Single-gap	2 mm			62 x 62 mm <sup>2</sup>				70.4 x 70.4 mm <sup>2</sup>				
Double-gap	2 mm			82 x 82 mm <sup>2</sup>				92 x 92 mm <sup>2</sup>				

**Table III.1 Coil Geometries, Resonance Frequencies, and Quality Factors.** The table also includes the dimensions of the four-element arrays for single-gap and double-gap TLR design as well as the respective interelement spacing. TLRs were loaded by the torso phantom in respective experiments.  $d_{\text{ext}}$  external TLR diameter,  $w$  conductor width,  $h$  substrate thickness,  $\epsilon$  relative permittivity of the substrate material,  $a_{\text{ext}}$  external diameter of the decoupling annexes,  $w_{\text{an}}$  conductor width for the annexes,  $l_{\text{an}}$  length of the linear segment connecting the annexes to the main windings.

The simulated transmission scattering parameters of two neighboring TLRs (corresponding to element 3 and 4 in four-element arrays, Figure III.1) as a function of the annex diameter are shown in Figure III.4 for single-gap (capacitively matched) and double-gap (inductively matched) design. The simulated decoupling levels with size-optimized annexes were -17.5 dB for single-gap TLR and -16.5 dB for double-gap TLR, respectively.

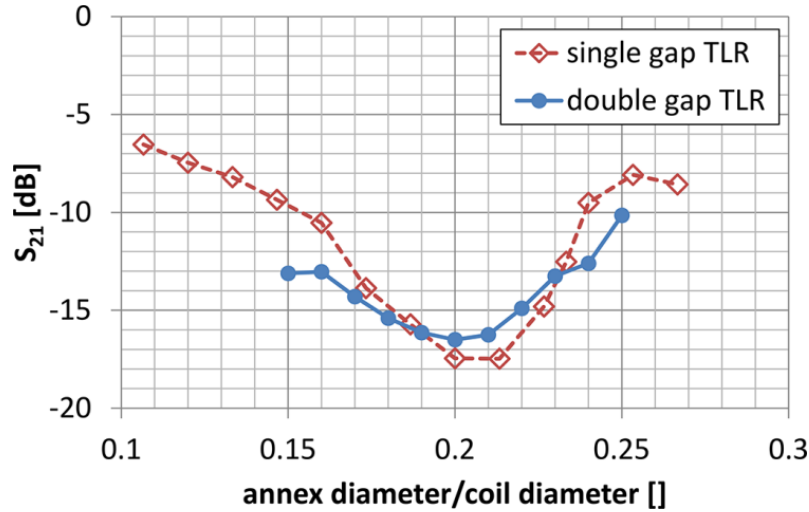


**Figure III.4 Annex size optimization.** The curves show the achieved simulated decoupling levels as a function of the relative annex diameter for single-gap (capacitively matched,  $d_{\text{ext}} = 30$  mm,  $w = 2.0$  mm,  $h = 510$   $\mu\text{m}$ ) and double-gap (inductively matched,  $d_{\text{ext}} = 40$  mm,  $w = 2.1$  mm,  $h = 127$   $\mu\text{m}$ ) TLR design.

For the final array configuration 15-mm pickup loops were selected after comparing matching performance, decoupling efficiency, noise factor, and  $B_1$  field distortion for pickup loops with diameters ranging from 10 to 30 mm in 5 mm steps. Typical matching levels better than -30 dB at the Larmor frequency could be achieved using any of the five tested pickup loops. However, a decrease in decoupling efficiency with increasing pickup loop size was observed in simulations (transmission increased from -16.2 dB to -12.5 dB) and bench measurements (from -14.7 dB to -12 dB), as shown in Figure III.5. Conversely, the noise performance improved with increasing pickup loop diameter. The calculated noise factors decreased from 3.1 (10 mm pickup loop diameter) to 1.1 (30 mm pickup loop diameter) corresponding to 4.9 and 0.4 dB noise degradation, respectively (Figure III.5). High-flip-angle images revealed an asymmetry in  $B_1$  distribution in comparison to the reference image obtained with the 30-mm pickup loop placed 20 mm above the TLR, which decreased with increasing pickup loop diameter.

The 15- and 20-mm pickup loops performed sufficiently well to be used in the developed four-element array; the 15-mm pickup loops were then selected as they provided a higher decoupling efficiency, which is the primary objective of this study. The corresponding pickup

loop noise factor was 1.6, and the measured isolation between neighboring TLRs was -14.3 dB.

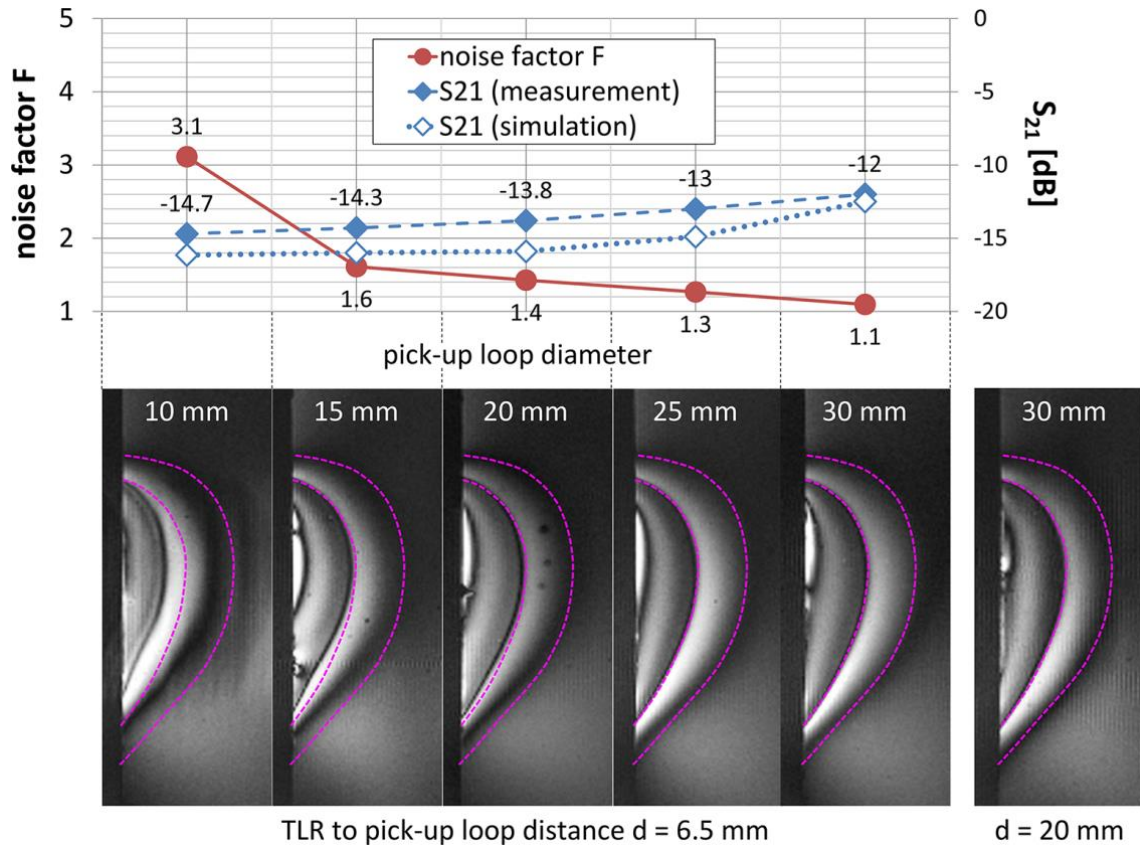


**Figure III.5 Pickup loop selection.** Simulated and measured transmission scattering parameters  $S_{21}$  and noise factors  $F$  are plotted as function of the pickup loop diameter. Transversal gradient echo images obtained using the investigated pickup loops are shown below. A high flip angle was used so as to evoke three  $180^\circ$  signal voids in the images. To highlight the field asymmetry, isocontours from the reference image (30-mm pickup loop at a distance of 20 mm; right) are overlaid with all images.

### III.4.2. Choice of the Array Design

Simulations of the current density (Figure III.6) show that the current is not equally distributed among all decoupling annexes with the single-gap TLR design whatever the matching configuration. As the current exhibits a minimum at the gap, two annexes placed at different distances from the gap do not carry the same current. This can be overcome with the double-gap design for which all annexes are placed at the same distance from the gaps. The



simulated current density distributions also show that connecting capacitive matching networks to the TLRs induces an asymmetry in current density between front and back conductor, while inductive matching provides the same current distribution on both faces of the TLR.

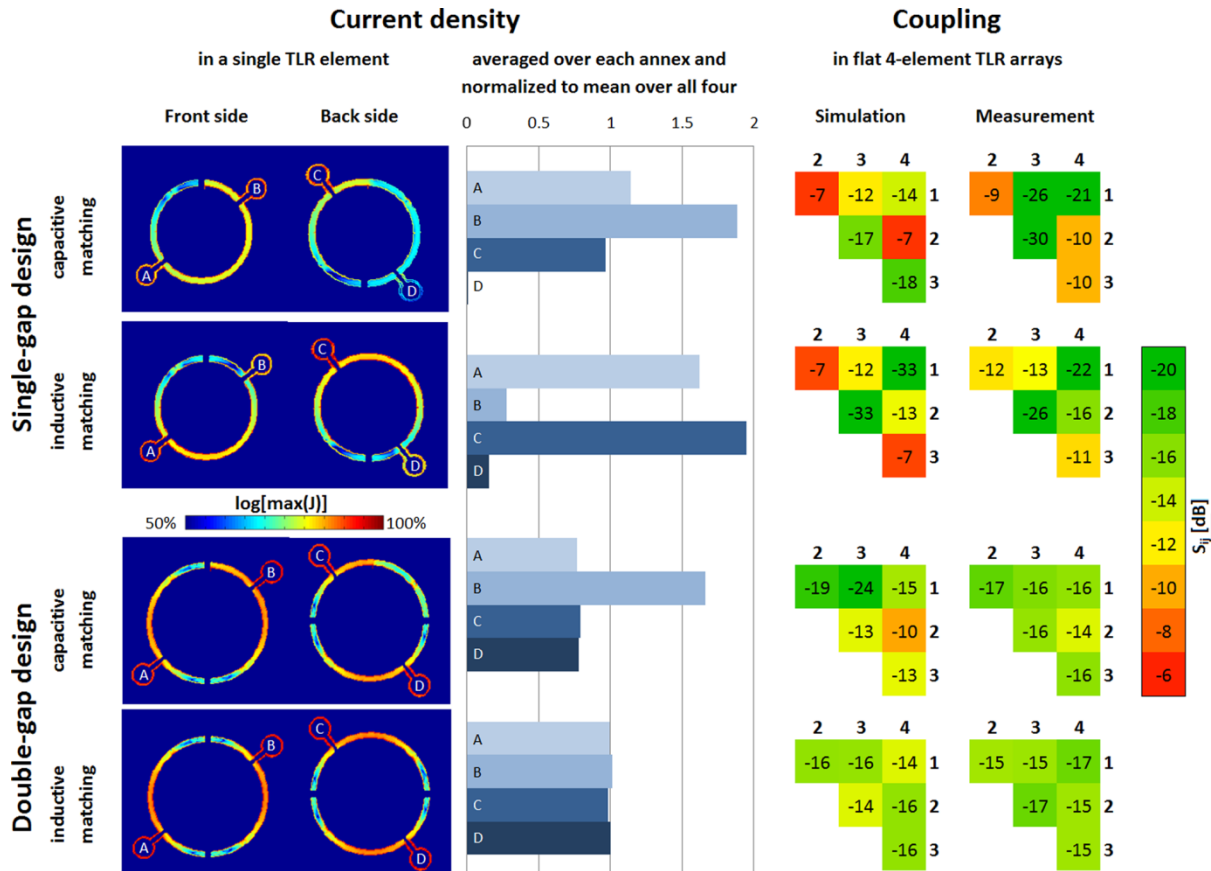


**Figure III.6 Choice of the array configuration.** Current density distributions in single TLR elements are shown on the left. The averaged current density in each annex normalized to the mean  $J$  in all four annexes is plotted in the center. On the right, simulated and measured decoupling levels are depicted.

The simulated S-parameter matrix (Figure III.6) of the capacitively matched four-element array of single-gap TLR shows unequal decoupling efficiencies for pairs of TLR elements ranging from -7 to -18 dB. A comparable asymmetry is observed when the single-gap array is inductively matched. Also for the double-gap TLRs a variation in decoupling efficiency is observed using capacitive coupling while the simulated transmission parameters are equilibrated with the inductive matching technique. Resulting transmission parameters for

the latter were -16 dB for nearest neighbors, and -14 dB for diagonal elements, which are not decoupled by overlapping annexes.

The S-parameter matrices of four-element arrays recorded in bench measurements (Figure III.6) basically reflect the behavior observed in EMS with slightly lower coupling values. For single-gap arrays and the capacitively matched double-gap array, the resonance peaks of the individual elements showed severe asymmetry in bench measurements due to insufficient interelement decoupling. No peak splitting or asymmetry was observed for the inductively matched array of double-gap TLRs for which an isolation of -15 dB or better was measured when loaded by the torso phantom. The observed decoupling performance proved robust when the same array was loaded by the torso of a volunteer, and also tuning and matching at the Larmor frequency could easily be achieved. In unloaded condition the coupling between diagonal elements, which are not decoupled with the proposed technique, increased to -6 dB while the isolation between direct neighbors remained below -15 dB.

Following the above results, the inductively matched array of double-gap TLRs was then chosen for MRI experiments.

### **III.4.3. Specific Absorption Rate**

Figure III.7 depicts maximum intensity projections of the simulated unaveraged SAR distributions for single double-gap TLRs with and without decoupling annexes, and for the selected four-element array. Adding the decoupling annexes leads to a 14.5 % lower peak SAR value. Further, it is demonstrated that no SAR hot spots are introduced at the location of the annexes, neither for the single TLR element (Figure III.7 b), nor for the four-element array (Figure III.7 c). For the four-element, array all TLRs were driven in-phase resulting in destructive interference of  $E$ -fields in the center.

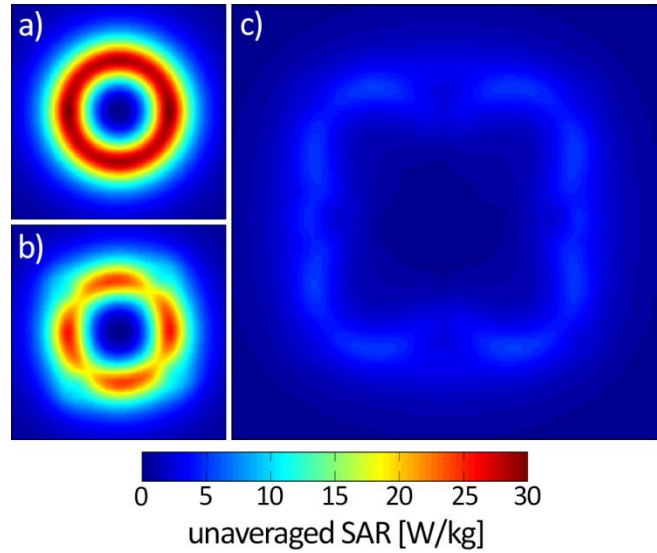


**Figure III.7 Unaveraged SAR distributions derived from 3D EMS.** Coronal maximum intensity projections of unaveraged SAR distributions are shown for double-gap TLRs, a: without decoupling annexes (see Figure III.1 b), b: with decoupling annexes (see Figure III.1 d), and c: for the selected four-element array (see Figure III.1 h). All elements of the four-element array were driven with equal amplitudes and phases, resulting in destructive interference of  $E$ -fields, and thus, negligible SAR between elements. SAR values are normalized to 1 W input power.

#### III.4.4. Performance of the Flexible TLR Array

Coronal GRE images and corresponding g-factor maps acquired with the selected four-element array in flat configuration are shown in Figure III.8. The depicted slices are located 2 and 20 mm below the phantom surface, which is separated from the array by a 5 mm thick acrylic glass plate. For the top slice a signal void between neighboring elements can be observed along the z-direction, where the produced  $B_1$  field is parallel to  $B_0$ . This effect is greatly reduced for the slice located deeper inside the phantom. Signal related to the decoupling annexes cannot be clearly distinguished.

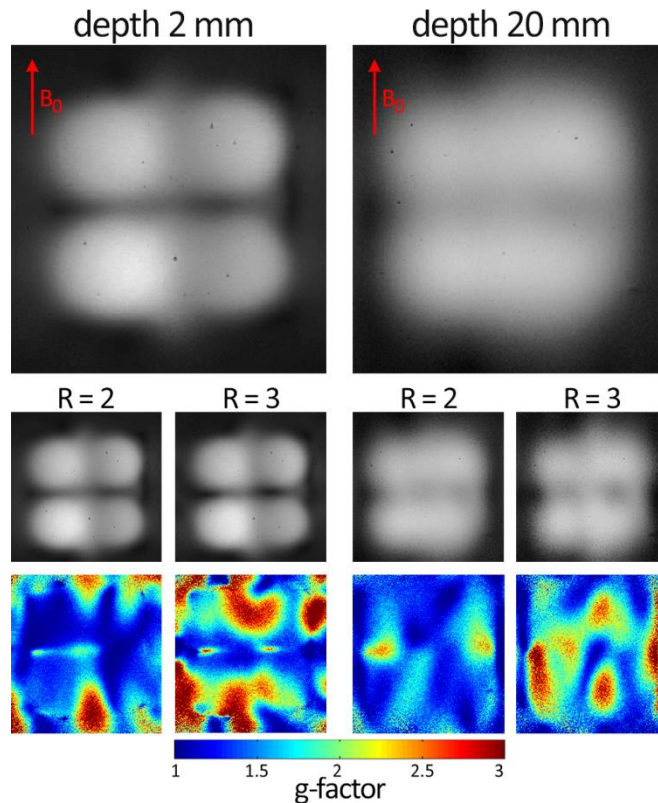


**Figure III.8 Coronal MR images acquired in flat array configuration.** Coronal GRE images of the torso phantom acquired with the inductively matched four-element array of double-gap TLRs at 7 T and corresponding g-factor maps are shown. The depicted slices are located 2 and 20 mm, below the phantom surface.

The measured transmission scattering parameters and corresponding noise correlation matrices of the inductively matched (15-mm pickup loop), four-element array of double-gap TLRs in bent and flat configuration are shown in Figure III.9 for direct comparison. In bent array configuration, slightly increased transmission S-parameters between neighboring elements are observed. Noise correlation values are comparable to those for the flat configuration with peak values of 0.31 (bent) and 0.34 (flat), respectively.

Figure III.9 also shows transversal phantom MR images acquired in flat and bent configuration and the calculated g-factor maps for acceleration factors  $R = 2$  and  $R = 3$ . No degradation in parallel imaging performance due to bending of the array was observed. Mean g-factors calculated for the elliptical ROI were  $1.2 \pm 0.2$  ( $R = 2$ ) and  $1.9 \pm 0.4$  ( $R = 3$ ) for the

flat configuration and  $1.1 \pm 0.1$  ( $R = 2$ ) and  $1.6 \pm 0.4$  ( $R = 3$ ) for the bent configuration, respectively.

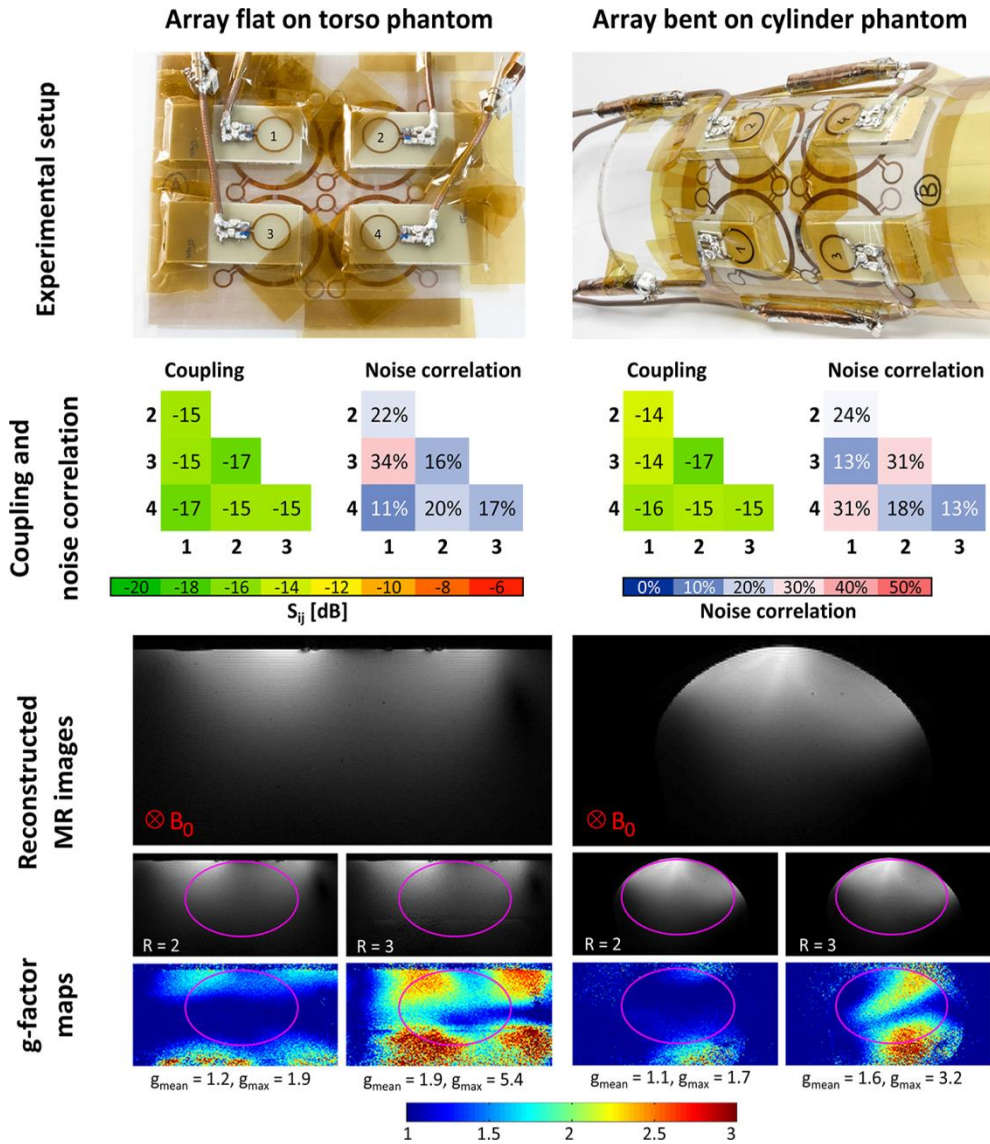


**Figure III.9 Influence of mechanical flexibility on the performance of the novel TLR array.** The experimental setup for the inductively matched double-gap array in planar (left) and bent (right) configuration is shown in the top row. Below transmission S-parameters and measured noise correlation matrices are plotted. At the bottom 7 T MR images reconstructed with GRAPPA acceleration factors of  $R = 1$  (no acceleration),  $R = 2$ , and  $R = 3$  and corresponding g-factor maps are shown. The peak and the mean g-factor for an elliptical ROI (major axis 60 mm, minor axis 40 mm) are listed below each map.

In Figure III.10, a high-resolution image of a kiwano fruit acquired in bent array configuration is shown. The decoupling performance of the form-fitted array when loaded by the kiwano fruit was comparable to that observed with the cylindrical phantom.

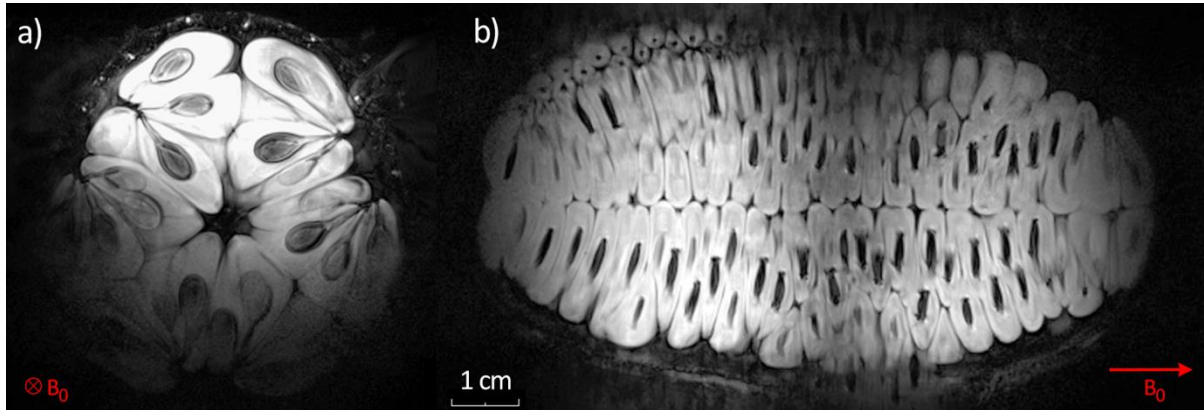


**Figure III.10 High-resolution images of a kiwano fruit (*Cucumis metuliferus*).** A transversal (a) and a coronal slice (b) are shown. GRE images ( $220 \times 220 \times 1000 \mu\text{m}^3$  resolution) were acquired at 7 T with the inductively matched array of double-gap TLRs in form-fitted configuration in an acquisition time of 7 min 15 sec. The pulp and the seeds of the fruit as well as the inner structure of the paring can be observed.

### III.5. Discussion and Conclusions

In this paper a novel technique for inter-element decoupling in TLR arrays based on mutual magnetic flux sharing via overlapping annexes is introduced. This new decoupling technique is frequency independent over a wide range and robust against variations in loading, similar to conventional overlap decoupling. Although this new decoupling technique was first demonstrated for 7T MRI, it is fully applicable to other static field strengths and can be implemented for various coil-element sizes. In addition, the larger FOV of nonoverlapped coils is retained, and more distinct sensitivity profiles of the individual elements are provided. This potentially allows for an improvement of the parallel imaging performance [122,123].

The decoupling efficiency of the proposed technique was optimized and evaluated for two- and four-element arrays with single- or double-gap designs, combined with capacitive or inductive matching.

It should be noticed that the difference in diameter between single-gap TLRs (30 mm) and double-gap TLRs (40 mm) used in this study does not prevent the comparison of the two designs in terms of mutual decoupling. The decoupling performance was optimized separately for both TLR types and has been shown to depend on the current density in the annexes and on the size of the annexes but not on the TLR diameter. A comparison in terms of imaging performances (SNR,  $B_1$  homogeneity, FOV) of the two designs would require the use of single-gap and double-gap TLRs with equal diameters. Since the aim of this work was to evaluate the performance of the presented novel decoupling method, however, the difference in diameters is not relevant.

Using 3D EMS, it is demonstrated that the decoupling efficiency in TLR arrays is closely related to the current density distribution along the transmission line. In particular, the current density has to be made equal for all decoupling annexes to equilibrate decoupling levels between all nearest neighbors in 2D-arrays. It is shown, that this can be achieved using a double-gap TLR design together with resonant inductive matching. Using the double-gap design, the respective distances between each annex and the closest gap (at which the current

density is forced to zero) are equal. As long as the symmetry of the half-wave sinusoidal current density along the conductor of the transmission line [53] is not broken, it follows that the current density in each annex is the same. An inductive matching scheme conserves this intrinsic symmetry, since it does not introduce a defined electrical ground at any position of the TLR. The capacitive matching network used in this work did not fulfill this criterion, and therefore, resulted in asymmetric current distribution. However, other approaches for positioning of the feed points on the TLR and possibly using asymmetric matching capacitors, could be studied in future work in view of equilibrating the current distribution in the TLR. But even if a solution can be found, resonant inductive matching still offers the intrinsic advantage for flexible arrays, that no solder joints have to be added onto the coils. It was demonstrated that tuning and matching may be achieved with this technique for various loading conditions (e.g., human torso, torso phantom, cylindrical phantom, and kiwano fruit).

The double-gap TLR geometry enables not only an equally distributed current density among the decoupling annexes but also a symmetric array layout regarding the relative gap position for the individual elements. The relative gap orientation may strongly influence the mutual coupling behavior, as Fang et al. [124] demonstrated for spiral surface coils. The proposed design avoids these effects, since each coil element has the same geometric relation to its four nearest neighbors (Figure III.1 g). Further, the investigated four-element arrays cover all nearest-neighbor interactions in tetragonally arranged arrays. Therefore, the proposed decoupling principle can be easily expanded to multielement linear or 2D arrays without restriction regarding the number of elements.

It was found that the influence of adding the decoupling annexes to the basic TLR geometry is not a limiting factor in terms of imaging and SAR performance. The resulting decrease of the resonance frequency can be accounted for by proper choice of the TLR geometry. The unloaded quality factor is decreased by adding the annexes, but is still well higher than the loaded Q indicating that sample noise is the dominating loss mechanism. When using this decoupling technique for small TLRs at lower field strength, e.g. 1.5 T, it should be considered that adding the decoupling annexes increases the coil noise, and therefore, also increases the coil diameter for which coil noise becomes dominant. As shown in Table III.1,



the optimal size of the annex is not fixed in general. It has to be specifically optimized for a given array configuration since the magnetic flux to be cancelled mainly depends on the size of the TLRs, on the distance between TLRs and on the arrangement of the array elements. The magnetic flux shared by the overlapped annexes depends on the thickness of the substrate and the annex size.

A theoretical limitation of the presented array design is that coupling between diagonal elements, which are not decoupled by overlapping annexes, may induce splitting of the resonance peak. In practice, however, a single peak is observed for each TLR element within the array when sufficiently loaded; this holds true for all investigated loading conditions. For applications where loading is minimal, further investigations might be needed to ensure proper tuning and decoupling.

Pickup loop matching in over-coupling mode can be implemented for transceiver coil arrays, but requires careful choice of the position and size of the pickup loops. These can be determined by finding a reasonable trade-off between pickup loop noise factor, coupling between neighboring pickup loops, and  $B_1$  distortion. The closer the free resonance frequency of a fabricated TLR matches the Larmor frequency, the less it has to be retuned and the smaller the noise contribution of the pickup loop is (see Eq. IV.2).

A slight asymmetry in signal intensity between the left and right side of the array was observed in 7 T MR images (Figure III.8 and Figure III.9). We believe that the major source for this artifact is high frequency effects introducing asymmetry in  $B_1^+$  and  $B_1^-$  [37]. Note that in the present work, all transmit elements were driven with equal amplitude and phase. Such asymmetry could in future implementations be alleviated by the use of optimized amplitude and phase settings between the coil elements, using, e.g. a parallel transmission system. This would be particularly beneficial for bent configurations, since the relative phases could be easily adapted to the target geometry without hardware changes.

The form-fitting ability of the developed array was successfully demonstrated in bench and MR experiments when wrapped upon a cylindrical former where the measured transmission scattering parameters, noise correlation matrices and g-factors proved robust concerning this

mechanical deformation of the TLR array. The proposed decoupling technique is especially favorable for form-fitting TLR arrays comprising a large number of elements, because readily decoupled arrays can be fabricated on a single flexible substrate in one standard photo-lithographic etching process. Also, in contrast to previous work proposing the principle of magnetic flux sharing for physically separated coils [113,114], no soldering is necessary.

Such flexible arrays are well-suited for studying anatomical regions, which may vary strongly in size and shape from patient to patient and require both a large FOV and high SNR. Potential biomedical applications include high-resolution imaging of skin and joints like wrist, elbow or knee, or dynamic imaging of moving organs such as the heart. In this respect, the performance of the developed prototype array will be further improved by increasing the number of coil elements and by adapting the size of the individual elements to the targeted organ or structure.

Considering, for instance, skin imaging [125,126], the achievable SNR could be further increased by miniaturizing the TLR elements until the threshold between sample and coil noise dominance is reached. In the coil noise domain, further SNR improvement could be achieved by reducing internal coil noise, e.g. by using superconducting coil technology [33]. The concepts presented here are particularly attractive for this field of applications since both the TLR coil design and the proposed decoupling technique are fully monolithic and none of them imposes limits in terms of coil miniaturization. Furthermore, the inductive matching approach used here avoids direct soldering on the coil, and thus, allows preserving low noise features of superconducting coils.

## **Chapter IV Additional information about the developed TLR array**

## **IV.1. Introduction**

This chapter presents additional data concerning the developed TLR array, which was not published in the original article [106].

In section IV.2 it is described how the mutual coupling between TLRs was assessed by calculating and measuring the mutual inductance, which clearly indicates the need of element decoupling in a TLR array.

Section IV.3 is concerned with the analytical modeling of TLRs. A comparison of the TLR resonance frequencies determined using the analytical model, 3D EMS and bench measurements is provided. Further, it is described how the measured Q factors of unloaded and loaded TLRs are used to roughly estimate the increase in coil noise induced by the decoupling annexes.

In section IV.4 additional MR imaging data is presented. The developed flexible TLR array was also used to acquire high-resolution images of a pepper fruit and of a sheep knee.

## IV.2. Preparatory study: Mutual inductance between TLRs

The mutual inductance between two neighboring TLRs ( $d_{\text{ext}} = 33.465$  mm,  $w = 3.465$  mm,  $h = 0.25$  mm;  $f_0 = 292$  MHz) was studied as a function of the distance between the coils by analytical calculations and on the bench.

### IV.2.1. Analytical modeling

Equations II.32 - II.36 were used to calculate the mutual inductance, where the vertical distance was set to zero as long as the two coils did not overlap, and to  $10 \mu\text{m}$  in the case of overlap, respectively. From an external point of view, a TLR behaves similarly to a simple loop coil [52]; therefore, each TLR was modeled as a single loop. The distance between the centers of the two coils was varied from 70 mm to 5 mm in steps of 0.1 mm. Calculations were done using Matlab (Mathworks, Natick, USA).

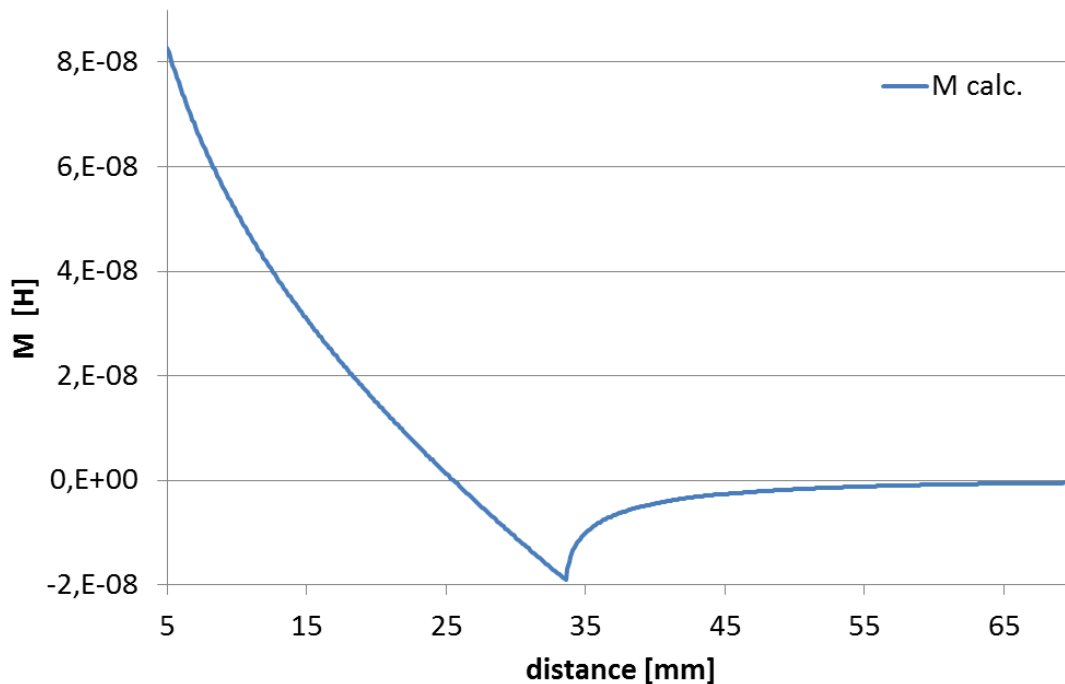


Figure IV.1 Calculated mutual inductance over distance between TLR centers

Figure IV.1 shows the computed mutual inductance as a function of the distance between coil centers. Per definition,  $M$  is positive when the net magnetic flux shared by the two coils is positive, and negative for negative flux, respectively. When the two TLRs are placed far from each other,  $M$  is close to zero. By decreasing the distance between coil centers the absolute value of  $M$  increases until the distance is in the range of the coil diameter. When the two coils overlap, positive and negative magnetic flux start to cancel each other, and the absolute value of  $M$  decreases again. This turning point corresponds to a distance of 33.6 mm for the chosen TLR geometry. By further decreasing the distance between the TLRs, the point of critical coil overlap is reached at one specific distance (here, 25.5 mm). At this point, the mutual inductance is zero, since the net magnetic flux produced by one coil in the other is zero, and hence, the two coils are mutually decoupled from each other. For smaller distances, the positive magnetic flux dominates, resulting in positive values for  $M$ , which continuously increase until the distance between coil centers is zero.

#### IV.2.2. Bench measurements

To experimentally determine the mutual inductance between two TLRs, a small untuned pick-up loop (approximately 3 mm diameter) was connected to the output terminal of the network analyzer and the  $S_{11}$  parameter was measured. The pick-up loop was positioned just below one TLR which was fixed on a custom measurement rig.

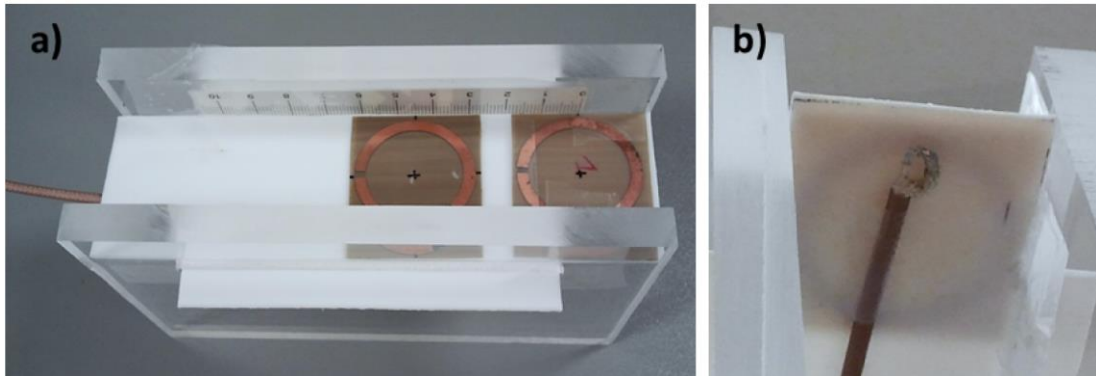


Figure IV.2 Measuring the coupling coefficient of two neighboring TLRs

The measurement rig with the two TLRs is shown in Figure IV.2.a, and the small pick-up loop placed below one TLR is depicted in Figure IV.2.b. The second TLR was shifted

manually relative to the fixed coil along one direction, varying the distance between the coil centers from 70 mm to 5 mm in 1-mm steps.

Due to the mutual coupling between the two TLRs, a second resonance peak was visible in the  $S_{11}$  spectrum. The lower ( $f_1$ ) and the higher ( $f_2$ ) resonance frequency in the  $S_{11}$  curve were measured and used to calculate the coupling coefficient  $k$  of the two synchronously tuned TLRs, [127]:

$$k = \frac{f_2^2 - f_1^2}{f_2^2 + f_1^2} \quad \text{IV.1}$$

To calculate the mutual inductance  $M$ , it is necessary to know the self-inductance  $L$  of each TLR.  $L$  can be deduced from the resonance condition of TLRs (Equation II.29), inserting the measured resonance frequency of the isolated TLR and the characteristic transmission line impedance, see Equations II.37 and II.38.

$$|M| = k \cdot \sqrt{L_1 L_2} \quad \text{with} \quad L_1 = L_2 = L \quad \text{IV.2}$$

Note that the coupling coefficient  $k$  is always positive with the used definitions and that in this case  $|M|$  corresponds to the absolute value of the mutual inductance determined by analytical calculations.

Figure IV.3 shows the absolute value of the mutual inductance  $M$  as a function of the distance between coil centers; experimental results are compared to analytical calculations. In general, the experimental and the theoretical curve are in good agreement. In the experiment, the critical overlap is reached for a distance of 25 mm between coil centers.

Deviations between theory and experiment can be observed close to the local maximum at a distance of approximately 33 mm, and for distances smaller than 10 mm. These deviations probably derive from experimental and theoretical imperfections: (1) The vertical distance of 10  $\mu\text{m}$  in the case of coil overlap defined for theoretical calculations could not be realized experimentally. Nonetheless, this distance was chosen in analytical modeling to highlight the sharp peak at a distance of 33.6 mm. (2) In experiments, it is assumed that the small pick-up

loop only couples to the TLR with fixed position; however, for small distances between TLR centers, this assumption no longer holds true. (3) Importantly, the assumption that a TLR can be replaced by an infinitesimally thin circular loop in the theoretical calculation does not hold when the windings of the two TLRs are close together. This effect most likely results in a “smoothing” of the measured curve of mutual inductance.

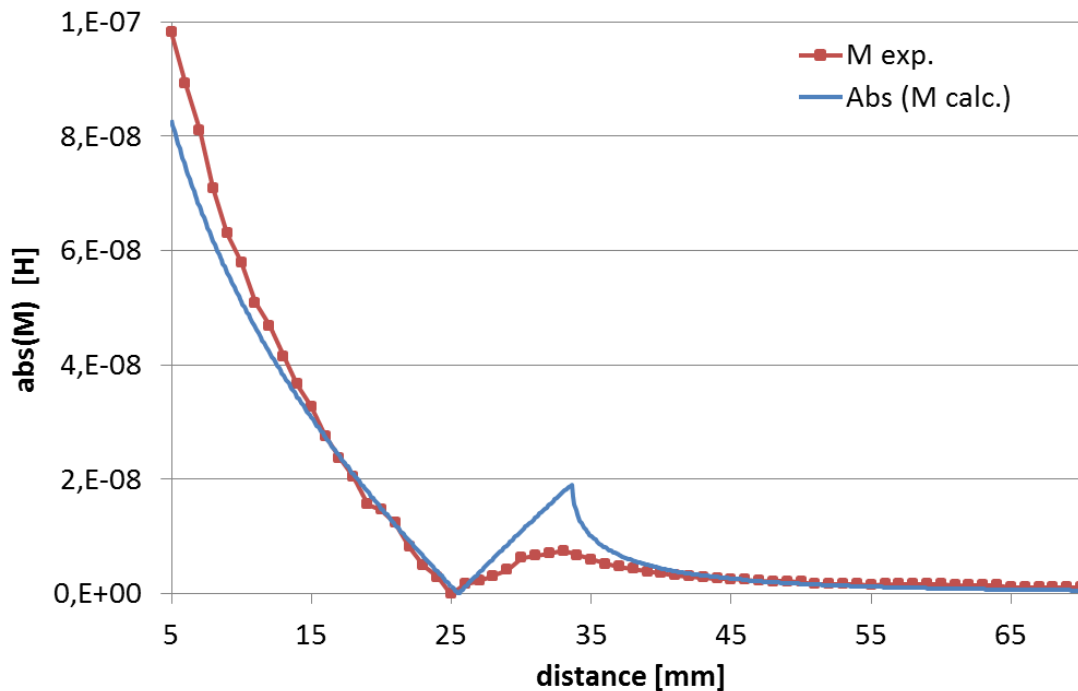


Figure IV.3 Mutual inductance over distance between TLR centers - theory and experiment

Figure IV.4 shows a plot of the measured frequencies  $f_1$  and  $f_2$ ; the larger the discrepancy between the two frequencies, the stronger the mutual coupling.

For large distances, the splitting of the resonance peaks is symmetric with respect to the original resonance frequency  $f_0$  (292 MHz). However, for small distances  $f_2$  deviates stronger from  $f_0$  than  $f_1$ , i.e. when the coupling becomes stronger, the high-frequency peak shifts farther from the original frequency than the low-frequency peak. This phenomenon provides an indicator for differentiating weak from strong coupling [66]. When the frequency splitting is approximately symmetric, the coupling is weak; otherwise, there is strong coupling. Weak coupling means that the second-order influence of the coupling from one coil to another and



then back to itself (“self-coupling”) can be neglected; when the coupling is strong, both self-coupling and mutual coupling coexist.

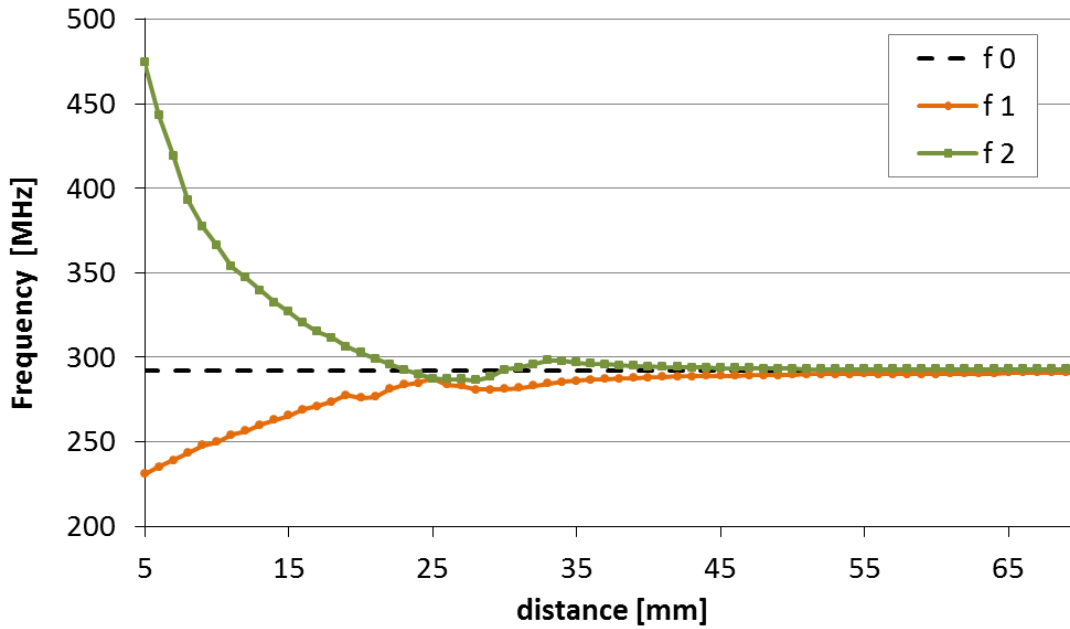


Figure IV.4 Measured resonance frequencies  $f_1$  and  $f_2$  over distance between TLR centers

This preparatory study clearly demonstrates that two TLRs placed in close vicinity to each other strongly couple. Therefore, mutual decoupling is needed when constructing an array of TLRs.

## IV.3. Geometry of the individual array elements

### IV.3.1. Resonance frequency analysis

As described in section III.3.1, starting values for the TLR geometries used for the individual array elements were determined using the analytical model for the resonance condition of TLRs (Equation II.29/III.1). The analytic model does not account for the effect of the decoupling annexes on the resonance frequency and is of limited accuracy (approximately 10 %). However, calculations are very fast and help to limit the parameter space for consecutive FDTD simulations which are very time-consuming for TLRs.

The resonance frequency, self-inductance  $L$ , and characteristic impedance  $Z_0$  calculated with the analytical model for single- and double-gap TLR designs, as described in Table III.1 but without decoupling annexes, are given in Table IV.1.  $L$  comprises the self-inductance of top and bottom conductor, and the respective mutual inductance (Equation II.30).  $Z_0$  was calculated using the wide band approximation ( $w > h$ ) given in equation II.37.

	$L$ model [nH]	$Z_0$ model [ $\Omega$ ]	$f_0$ model [MHz]
Single-gap TLR no annexes	243.5	51.6	445.6
Double-gap TLR no annexes	422.2	14.1	302.4

Table IV.1 Analytical modeling of single- and double-gap TLRs

Double-gap TLRs without decoupling annexes were also studied in 3D EMS and bench measurements. Respective resonance frequencies were 344.0 MHz for 3D EMS (loaded), 335.0 MHz for experiments (loaded), and 339.7 MHz (unloaded), as indicated in Table III.1. Therefore, the resonance frequency of the double-gap TLR without annexes calculated by analytical modeling can be directly compared to the resonance frequency determined in 3D EMS and bench experiments. The comparison indicates that the self-resonance frequency determined by 3D EMS (loaded configuration) deviates much less from the experimental

value than the frequency predicted with the analytical model (unloaded configuration, value given in Table IV.1).

$$\frac{|f_{0 \text{ bench unloaded}} - f_{0 \text{ model unloaded}}|}{f_{0 \text{ bench unloaded}}} \cong 11\% \quad \text{IV.3}$$

$$\frac{|f_{0 \text{ bench loaded}} - f_{0 \text{ 3D EMS loaded}}|}{f_{0 \text{ bench loaded}}} \cong 3\% \quad \text{IV.4}$$

### IV.3.2. Noise contribution from the decoupling annexes

Further, in bench experiments summarized in Table III.1 it was found that the Q-factor of the unloaded TLRs is decreased by adding the decoupling annexes, which means that the annexes increase the internal coil noise. The measured Q-factors together with the analytically calculated TLR inductance  $L$  (Table IV.1) can be used to calculate rough estimates for the internal coil resistance ( $R_C$ ) and the resistance added by the sample ( $R_S$ ). The accuracy of these calculations is limited by the accuracy of the inductance calculation and experimental imperfections.

$$R_C = \frac{\omega L}{Q_{\text{unloaded}}} \quad \text{IV.5}$$

$$R_S = \frac{\omega L}{Q_{\text{loaded}}} - R_C \quad \text{IV.6}$$

These equations yield  $R_C = 2.4 \Omega$ , and  $R_S = 28.2 \Omega$  for the double-gap TLR without decoupling annexes. Assuming that the sample induced noise is not changed by adding the annexes, the respective TLR inductance  $L_{\text{an}}$  and resistance  $R_{C,\text{an}}$  with decoupling annexes can be calculated; resulting values are  $L_{\text{an}} = 477.8 \text{ nH}$ , and  $R_{C,\text{an}} = 3.4 \Omega$ . This indicates that the decoupling annexes lead to an increase in coil resistance by approximately  $1 \Omega$ . However, the loaded  $Q$  is approximately equal for TLRs with and without decoupling annexes, and much lower than the unloaded Q-factor. This indicates that sample noise is clearly the dominant noise mechanism.

## IV.4. High-resolution MRI with the flexible array

### IV.4.1. MR imaging of a pepper fruit

In addition to the kiwano fruit, the inductively matched four-element array of double-gap TLRs was also used to acquire 7 T MR images of a pepper fruit (*Capsicum annum*) in form-fitted configuration. The pepper fruit could be inserted into the acrylic glass former used in section III.3.4.3. Tuning and matching at the Larmor frequency could easily be achieved by adjusting the respective capacitors on the pick-up loops, and also the observed decoupling performance proved robust against the variation in loading.

Figure IV.5 shows a transversal spin echo image of the pepper fruit with an in-plane resolution of  $100 \times 100 \mu\text{m}^2$ . The image was acquired in 18 min 48 sec using a 2D turbo spin echo sequence (TSE,  $T_R / T_E = 4000 \text{ ms} / 52 \text{ ms}$ , 10 slices, 1.9 mm slice thickness). On the left side of the image a bruise where the inner structure of the pulp is damaged can be identified.

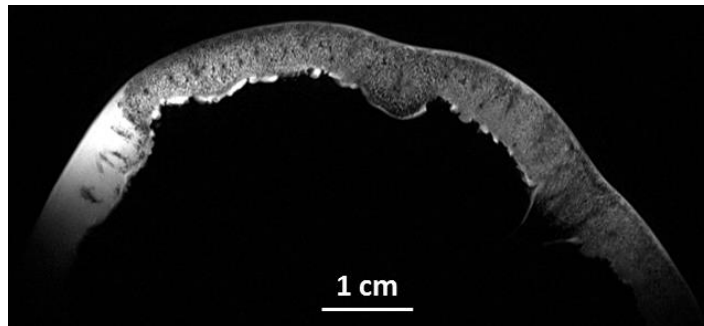


Figure IV.5 TSE image of the pepper fruit,  $100 \mu\text{m}$  in-plane resolution

Although spin echo based sequences are generally less suitable for surface coils in comparison to gradient echo sequences due to their high sensitivity to inhomogeneous  $B_1$  distributions [128], the pepper fruit constitutes a special case, because the signal only emerges from a region over which an almost constant flip angle distribution can be achieved with the form-fitted array.

#### IV.4.2. MR imaging of a sheep knee

Further, the developed TLR array was placed on a 1.5 mm thin flexible PTFE plate and form-fitted (without the acrylic glass former) to a sheep knee, which served as a tissue equivalent phantom. Again, tuning and matching could be obtained without difficulties, and the decoupling annexes provided sufficient inter-element decoupling.

Figure IV.6 shows how the developed array was form-fitted to a sheep leg at the position of the knee, since knee MRI is a potential application for the flexible TLR array.

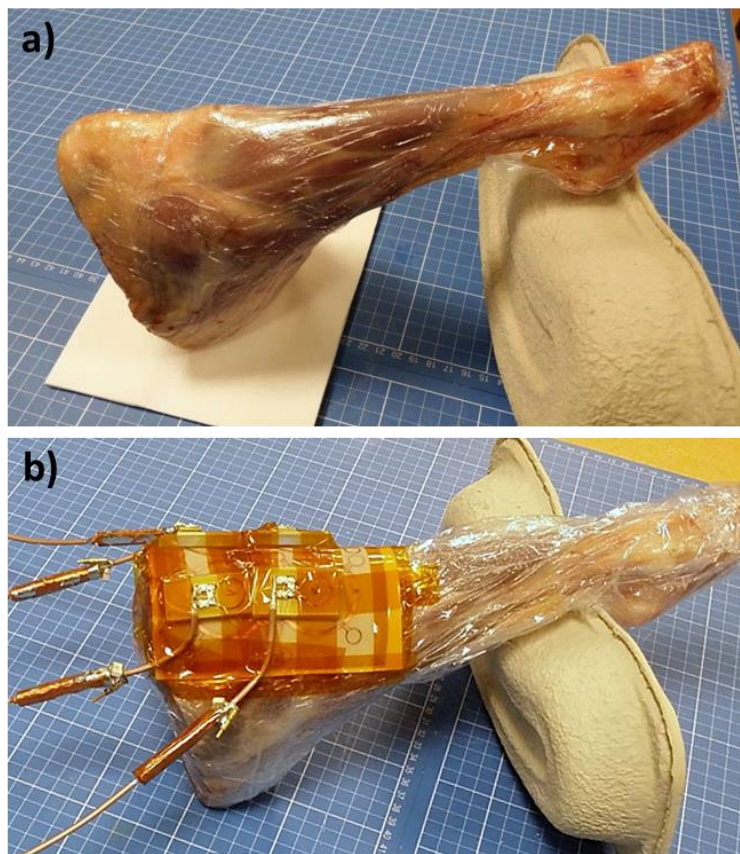


Figure IV.6 Photo of the sheep knee without (a) and with (b) the flexible TLR array

An MP-RAGE (Magnetization Prepared Rapid Acquisition Gradient Echo) sequence was used to acquire a  $T_1$ -weighted image of the sheep knee. In this sequence an initial  $180^\circ$  inversion pulse is applied, followed by a 3D GRE acquisition [129]. The image was acquired in 12 min 17 sec with an isotropic resolution of  $300 \mu\text{m}$ , and the following sequence

parameters:  $T_R/T_E = 2360 \text{ ms} / 3.77 \text{ ms}$ , inversion time  $T_I = 1700 \text{ ms}$ . The epiphyseal plates, the cartilage, the patellar ligament, and a fracture in the head of the tibia filled with liquid can be observed.

Further, the developed array was used to acquire 3D GRE images ( $T_R/T_E = 13 \text{ ms} / 5.66 \text{ ms}$ ) of the knee with an isotropic resolution of  $120 \mu\text{m}$ , shown in Figure IV.8. The acquisition time was 16 min 2 sec. The image was cropped to the region that appears hyper-intense in Figure IV.7, and provides a more detailed view of the patellar ligament and the cartilage.

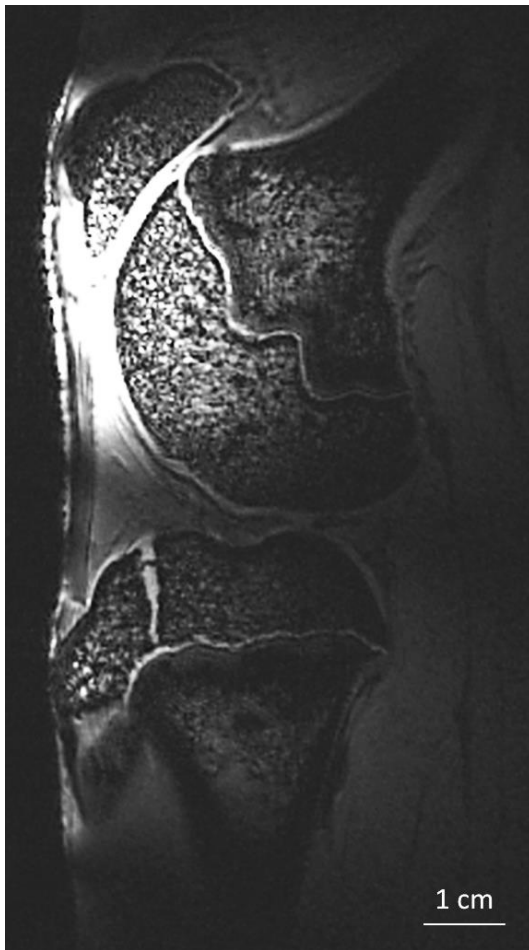


Figure IV.7  $T_1$  weighted image of the sheep knee,  $300 \mu\text{m}$  isotropic resolution

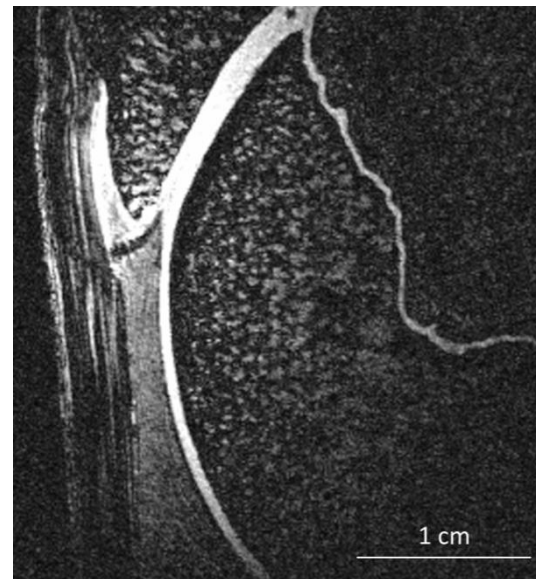


Figure IV.8 GRE image of the sheep knee,  $120 \mu\text{m}$  isotropic resolution

## **Chapter V    Other Advances with TLR Coils**

## **V.1. Introduction**

Besides the development of a flexible TLR array, in the scope of this thesis other advances concerning TLRs for MRI have been made, which are summarized in this chapter.

Firstly, an alternative to the capacitive matching network was sought, that does not perturb the intrinsically symmetric current density distribution along the TLR; this matching scheme could then be used in TLR arrays which employ mutual decoupling by overlapping annexes. A suitable network is described in section V.2. Additionally, a network which can be used in combination with capacitive matching to actively detune a TLR during transmission for operation in receive-only mode is introduced in section V.3.

Secondly, a novel TLR design is introduced, that enables the fabrication of multi-turn TLRs with several gaps per conducting band. The first study with the novel TLR design was performed at 4.7 T, and is presented in section V.4. After successful implementation of a prototype coil, a comparison study including several TLRs employing the novel design was conducted at 7 T; this is described in section V.5.



## V.2. Alternative capacitive matching scheme

### V.2.1. Investigated matching networks

After successful implementation of the four-element TLR array using the presented inductive matching scheme, alternative capacitive matching schemes were investigated. Several advantages of a capacitive matching scheme that preserves the intrinsically symmetric current density distribution along the TLR are expected in comparison to inductive matching. The increased coupling between TLRs due to the mutual coupling between pick-up loops could be avoided, and the introduction of additional circuitry for transmission decoupling and preamplifier decoupling are facilitated, in the case that the array should be used in receive-only mode.

In addition to the configuration shown in Figure III.2a, the matching scheme presented in Figure V.1 was investigated. The matching network is connected across an additional gap that is inserted in one of the conductors. The additional gap is located at the center of a conducting section, i.e. at the position of a gap in the conductor on the other side of the substrate. Tuning to the Larmor frequency and matching to  $50 \Omega$  can be achieved by adjusting the respective trimmer capacitors.

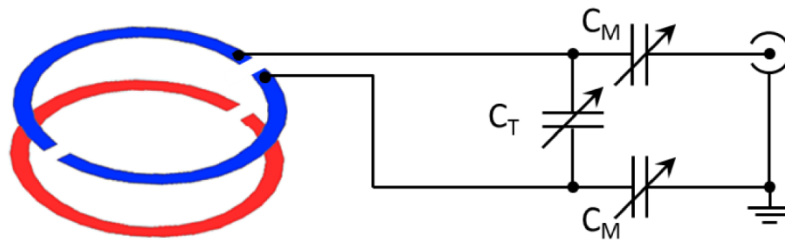


Figure V.1 Capacitive network connected at the center of one conductor

### V.2.2. Simulations

This capacitive matching scheme was tested when connected to the double-gap TLRs with decoupling annexes used for the developed four-element array (see Table III.1). The network was connected across a third gap on the front conductor placed in the center between the original two gaps, as shown in Figure V.2.

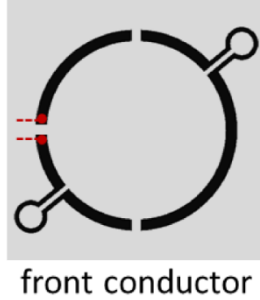


Figure V.2 Alternative feed point with capacitive matching for double-gap TLRs

First tests were performed using 3D EMS in combination with circuit co-simulation. It was found that with the proposed configuration tuning and matching could be achieved in a frequency range from approximately 330 - 380 MHz with capacitance values ranging from 1 - 30 pF for  $C_T$  and  $C_M$ ; this is well above the original resonance frequency of the TLR (310 MHz). Since tuning and matching at the  $^1\text{H}$  Larmor frequency at 7 T could not be achieved, it was decided to tune the TLRs to 350 MHz for further investigations.

At this frequency, the current density distribution in single TLR elements was simulated. The results in comparison to the resonant inductive matching setup are presented in Figure V.3

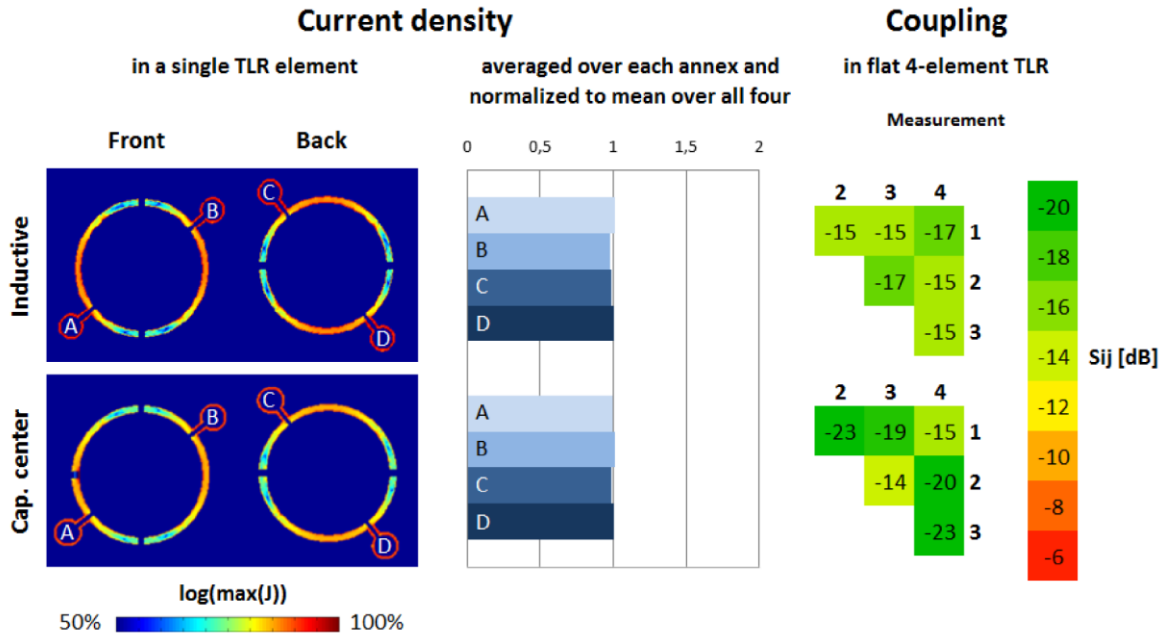


Figure V.3 Decoupling efficiency with inductive and center capacitive matching

The current density distribution along the TLR for the capacitive and the inductive matching scheme are comparable, i.e. a symmetric current distribution among all decoupling annexes can be achieved with center capacitive matching.

### **V.2.3. Bench tests**

The capacitive matching network was implemented on a four-element array fabricated for the studies presented in 0. All elements could be tuned and matched at the selected frequency of operation (350 MHz). The transmission S-parameters were measured, and are shown in Figure V.3 in comparison to those measured with the inductive matching setup. The resulting decoupling levels were  $< -19$  dB between nearest neighbors in the four-element array, and therefore lower than those achieved with inductive matching. The coupling between the diagonal elements of the array, which are not decoupled by overlapping annexes, is slightly higher to that measured with the inductive matching setup.

These results indicate that the presented capacitive matching scheme can be used without perturbing the intrinsically symmetric current distribution along the TLR, and is therefore compatible with decoupling by overlapping annexes. In order to be implemented for  $^1\text{H}$  imaging at 7 T, the used TLR geometry has to be adapted in a way to permit tuning to the Larmor frequency.

## V.3. Active detuning for TLRs

### V.3.1. Matching and detuning circuit

An active detuning scheme that allows a TLR to be used as receive-only probe is shown in Figure V.4. The feed point is chosen to be in the center of the top conductor opposite of the gap as shown in Figure V.1. In addition to the tuning and matching capacitors  $C_T$  and  $C_M$ , the matching scheme also contains a trap circuit composed of the capacitor  $C_{AD}$  and the inductor  $L_{AD}$ . The trap circuit forms a resonant circuit tuned to the TLR resonance frequency, and therefore represents a high impedance which blocks current flowing in the coil. It can be activated via the PIN diode switch, where the required DC voltage is supplied via the coaxial cable using an RF choke.

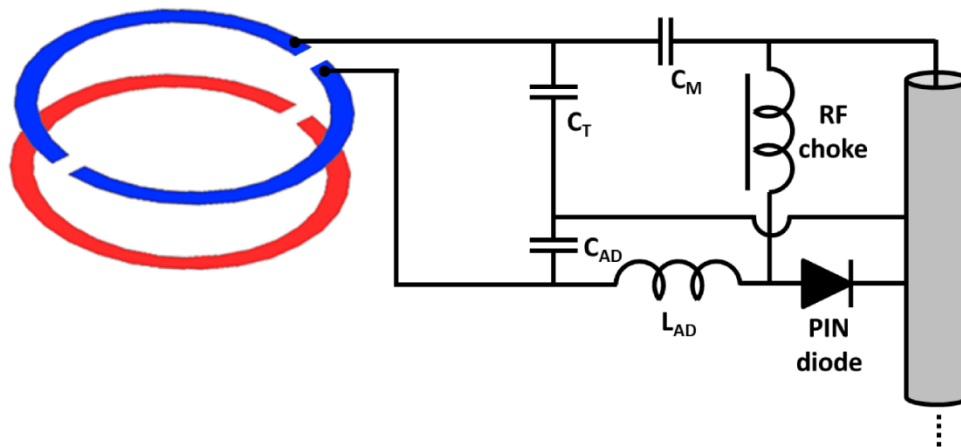


Figure V.4 Capacitive matching scheme for TLRs with active detuning circuit

The proposed detuning circuit was tested at 3 T. At this field strength, a transmit body coil is usually integrated in the MR scanner, and surface coils are likely to be used as receive-only probes. The TLR used in this first feasibility study was not initially designed for 3 T MRI; it was designed for a comparison study at 7 T, which is described in section V.5, and was adapted in a way that it can be used at 3 T. The used coil was a single-turn TLR with an external diameter  $d_{\text{ext}} = 10$  cm, a conductor width of 25 mm, and a 790  $\mu\text{m}$  thick PTFE substrate. The original structure had four gaps, three of which were closed by soldering copper strips onto the TLR. This way the self-resonance frequency was reduced, and the TLR

could be capacitively tuned and matched at the proton Larmor frequency at 3 T, i.e. 123.2 MHz.

$C_T$  and  $C_{AD}$  were composed of a ceramic capacitor with fixed capacitance (56 pF) and a trimmer capacitor (6.5 - 30 pF); similarly,  $C_M$  was composed of a 82 pF ceramic capacitor and a trimmer capacitor. These rather large values for the capacitances had to be chosen in order to successfully tune and match the TLR at 123.2 MHz. Consequently, the required inductance  $L_{AD}$  was small (approximately 20 nH); it was realized by forming 3.5 windings of 1 mm thick copper wire with a mean winding diameter of 2.5 mm. This configuration using a small trap inductance is not optimal since the achievable blocking impedance increases with  $L_{AD}$  [70]. Fine adjustments were performed with all components in place by adjusting the trimmer capacitors, and by slightly squeezing or stretching the inductor  $L_{AD}$ .

### **V.3.2. Experimental evaluation**

The active detuning scheme was evaluated on the bench using the double-loop probe method. The TLR was connected to a preamplifier and the required DC voltage was supplied to switch the PIN diode. An  $S_{21}$  drop between Rx state and Tx state of -27 dB was measured, where the difference of the two states determines the isolation between the receive and the transmit coil [70].

The setup was also tested in a 3 T whole-body MR scanner (Tim Trio 3T, Siemens Medical Solutions, Erlangen, Germany). The TLR coil was placed on the top side of a cylindrical phantom (20 cm diameter, 19 cm long) and connected to the receive chain of the scanner. 3D GRE images ( $T_R/T_E = 6.9 \text{ ms}/2.93 \text{ ms}$ , 1.3 mm isotropic resolution, 25 cm<sup>3</sup> FOV,  $T_{acq} = 2 \text{ min } 23 \text{ sec}$ ) were acquired in two different configurations: (1) The body coil was used for RF transmission and the TLR was used for signal reception; (2) The body coil was used for both, transmission and reception, while the TLR coil was actively detuned. The first test configuration shows whether the setup allows MR images to be acquired with the TLR in receive only mode. The second configurations reveals if current is induced in the TLR during RF transmission despite the detuning circuit, and causes detectable imaging artifacts.

GRE images acquired in the configurations described above are shown in Figure V.5. The left image shows that MR imaging can be performed with the TLR used as receive only probe employing the proposed detuning circuit. However, the image acquired with the body coil in transmit/receive mode shows a reduction of the signal intensity close to the location of the TLR. This indicates that the achieved isolation between body coil and TLR is insufficient, and that a more efficient blocking of the current in the TLR would be desirable.

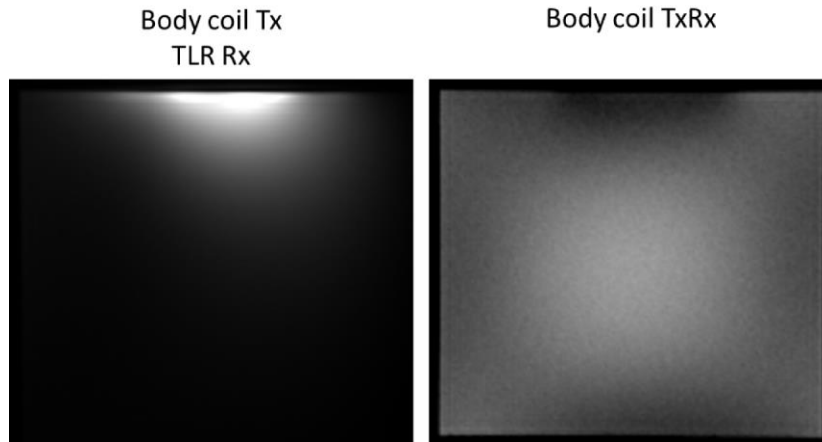


Figure V.5 GRE images acquired with the body coil and the TLR at 3 T

The TLR used in this first feasibility study was not initially designed for  $^1\text{H}$  imaging at 3 T; therefore its resonance frequency was not optimized for this application. It is expected if a TLR would be designed in a way that smaller capacitances could be used for  $C_T$  and  $C_{AD}$ , to achieve tuning to the Larmor frequency, and consequently the inductance  $L_{AD}$  could be increased, the achievable blocking impedance would be higher resulting in a better isolation and artifact-free images [130].

## V.4. MTMG TLRs - Proof-of-principle at 4.7 T

Work described in this sub-chapter has been presented at the 30<sup>th</sup> Annual Scientific Meeting of the ESMRMB held in October 2013 in Toulouse, France [131].

### V.4.1. Multi-turn multi-gap TLR principle

Up to now, high-field applications requiring a large FOV could not be addressed by multi-turn TLR (MTLR) technology because of the intrinsically low resonance frequencies of large MTLRs. High frequency resonators require a small equivalent inductance and/or capacitance, consequently setting a maximum diameter or a maximum number of turns for the coil. Contrarily, for a given size, the minimum equivalent inductance and capacitance of the MTLR limit the highest achievable frequency.

In this work, a novel TLR design is proposed which permits the use of MTLR technology for large FOV applications at high field strength – the multi-turn multi-gap (MTMG) TLR design (Figure V.6). This novel design exploits the fact that the resonance frequency of the TLR increases almost linearly with the number of gaps. So far, resonators with more than one gap per conducting band existed only in the single-turn configuration because no design scheme for multiple turns was available.

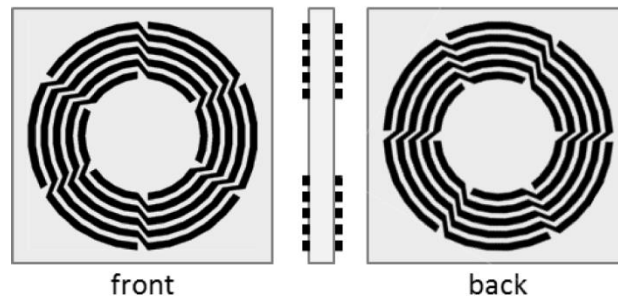


Figure V.6 Multi-turn multi-gap TLR

A prototype coil was designed and fabricated for proton imaging at 4.7 T. It was tested on the workbench and in a small-animal MR imaging system.

### V.4.2. Analytical modeling

A suitable MTMG TLR design for this feasibility study was found with the presented analytical model (Equation II.29) after modifying the Matlab toolbox in a way to vary the number of gaps on multi-turn TLRs.

A TLR design with a predicted resonance frequency slightly above the Larmor frequency was chosen because it was expected that the resonance frequency would decrease in experiments upon loading of the coil with the sample. PTFE ( $\epsilon = 2.05$ ) with a thickness of  $510 \mu\text{m}$  was chosen as substrate material because it was readily available for the fabrication of a prototype.

$d_{\text{ext}}$ [mm]	$w$ [mm]	$p$ [mm]	$h$ [ $\mu\text{m}$ ]	$\epsilon$	$N$	$N_g$
42	1	1.2	510	2.05	6	4

Table V.1 Geometric parameters of the MTMG TLR prototype for  $^1\text{H}$  imaging at 4.7 T

The geometric parameters of the designed MTMG TLR prototype are listed in Table V.1; the TLR geometry is given in terms of the external TLR diameter  $d_{\text{ext}}$ , the conductor width  $w$ , the spacing between two turns  $p$ , the number of turns  $N$ , the number of gaps  $N_g$ , the relative permittivity of the substrate material  $\epsilon$ , and the substrate thickness  $h$ . A sketch of the coil is shown in Figure V.7, [131].

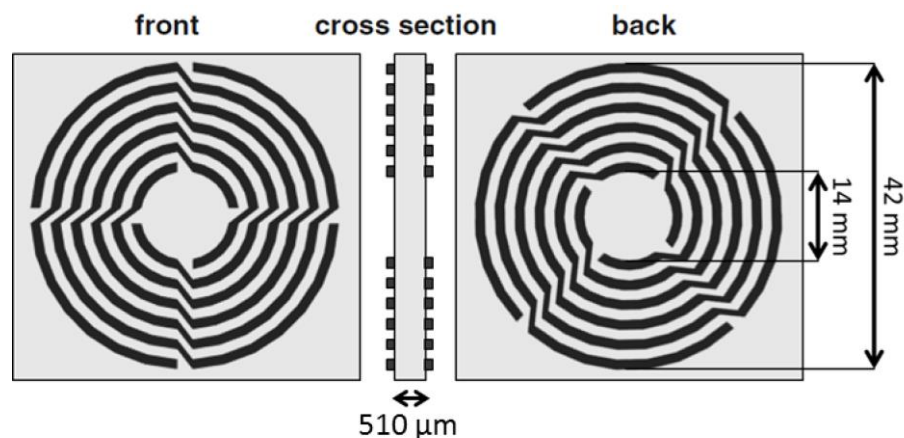


Figure V.7 Design of the MTMG TLR prototype for  $^1\text{H}$  imaging at 4.7 T, reproduced from [131]



### V.4.3. Bench measurements

The free resonance frequency of the fabricated TLR was measured with the single-loop probe method and compared to the theoretically predicted value. The theoretically predicted (215 MHz) and measured resonance frequencies of the unloaded coil (204.2 MHz) agreed with a deviation of 5% [131].

Further, the coil's Q-factor was measured for three different conditions. First the coil was placed in flat configuration on a phantom with a flat surface. Then the coil was tested on a cylindrical phantom, where it was used in flat as well as in form-fitted configuration (Figure V.8). The measured Q-factors were 340 for the unloaded flat coil, 46 for the flat coil loaded with the planar phantom, 80 for the flat coil loaded with the cylindrical phantom, and 60 for the coil form-fitted to the cylindrical phantom [131].

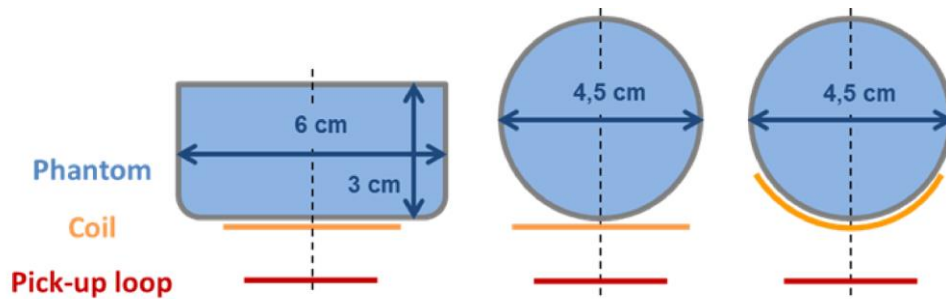


Figure V.8 Measurement conditions for the MTMG TLR prototype at 4.7 T

Fine tuning and matching for MRI experiments was performed using resonant inductive matching using a pick-up loop with a diameter of 2 cm placed coaxially with the TLR at a distance of 1.5 cm [131].

### V.4.4. MR imaging

MR imaging with the novel MTMG TLR was performed in transmit/receive mode on a 4.7 T Bruker small-animal MR imaging system [131]. 3D gradient-echo images were acquired in the three coil configurations shown in Figure V.8. The SNR was calculated for all images; the images and SNR maps of the cylindrical phantom were used to compare the coil performance in flat and form-fitted configuration.

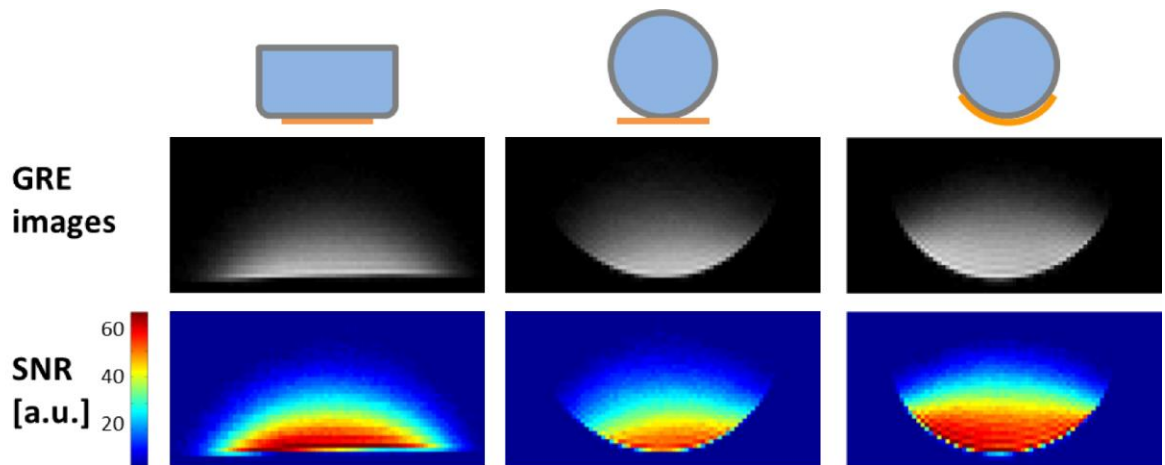


Figure V.9 GRE and SNR maps obtained with the MTMG TLR prototype at 4.7 T

Figure V.9 depicts gradient echo images acquired with the MTMG TLR prototype and calculated SNR maps. It is shown that the novel TLR coil can be used for MRI and its form-fitting ability is demonstrated. The comparison between flat and bent coil configuration reveals that form-fitting the coil to the cylindrical phantom leads to an SNR gain not only at the sides of the phantom, but also along the central axis.

## V.5. MTMG TLRs at 7 T

### V.5.1. Coil design

After successful experiments with the prototype coil at 4.7 T, various MTMG TLRs for  $^1\text{H}$  imaging at 7 T with an external diameter of 10 cm were designed using the analytical model. This coil size could not have been achieved for that operating frequency (approximately 300 MHz) with single-gap MTLR design using commonly available substrates.

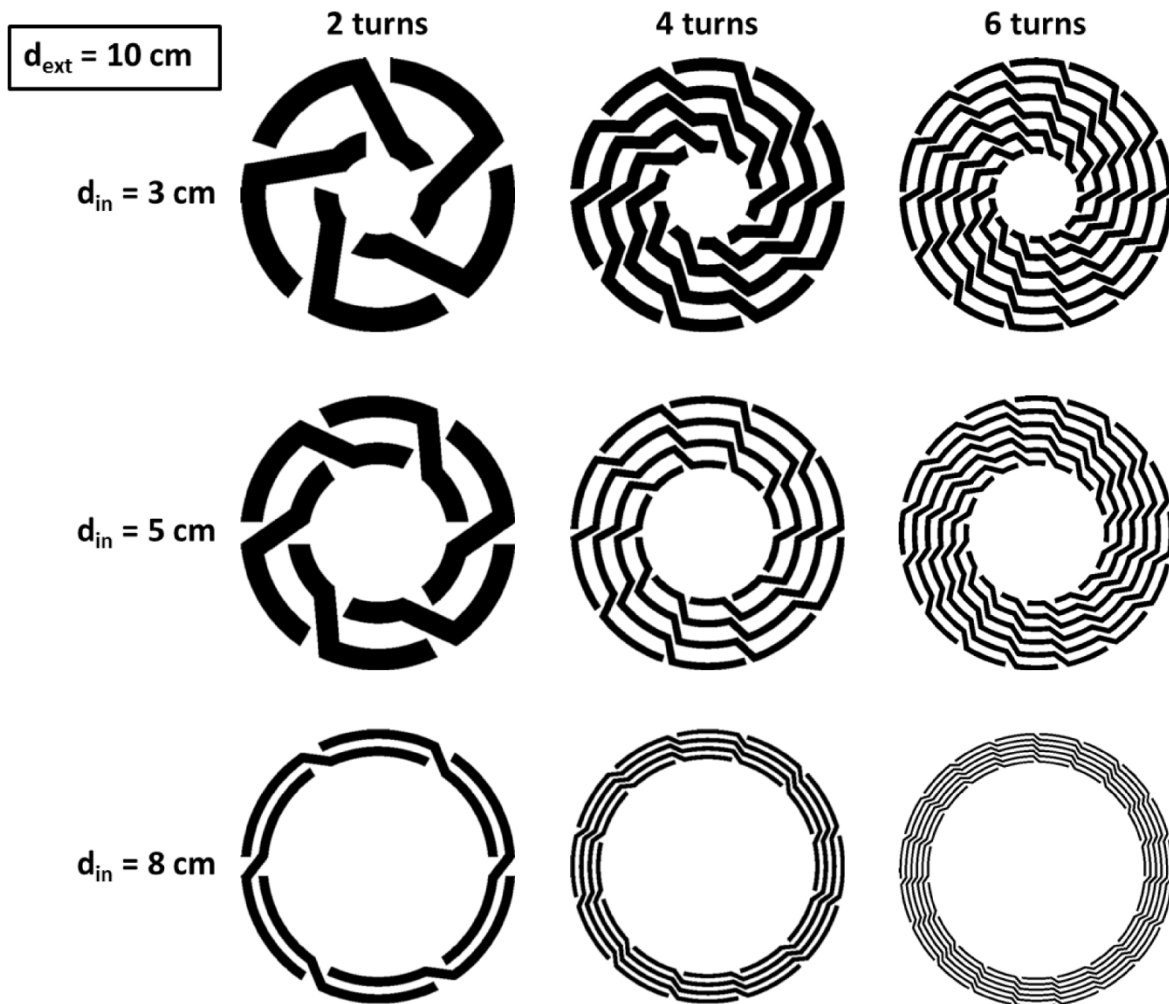


Figure V.10 MTMG TLR designs (only front conductors shown) for  $^1\text{H}$  imaging at 7 T

Again, PTFE was selected as substrate material, and the substrate thickness was chosen to be 790  $\mu\text{m}$ . The analytical model yielded a variety of possible MTMG TLR designs, out of which nine were selected for fabrication; the nine selected designs vary in number of turns and inner TLR diameter, as shown in Figure V.4. The selected MTMG TLRs together with single-turn TLRs with the same diameter for comparison, were fabricated by a third party (db electronic, Daniel Boeck SAS, Saint-Louis, France) with standard photolithographic etching techniques.

The geometric parameters and estimated resonance frequencies of the designed MTMG TLRs are given in Table V.2. The calculated resonance frequencies for the single-turn TLRs deviate farther from the targeted Larmor frequency, due to the limited degrees of freedom for the single-turn design, no more accurate designs could be found.

Name	$d_{ext}$ [mm]	$d_{in}$ [mm]	$w$ [mm]	$p$ [mm]	$h$ [ $\mu\text{m}$ ]	$\epsilon$	$N$	$N_g$	$f_0$ model [MHz]
2T-3cm	100	28.6	8	19.7	790	2.2	2	5	301.3
4T-3cm	100	31.4	4	6.1	790	2.2	4	10	302.5
6T-3cm	100	32	2	4.4	790	2.2	6	14	305.0
1T-5cm	100	50	25	-	790	2.2	1	4	287.9
2T-5cm	100	51.4	6.8	10.7	790	2.2	2	6	302.4
4T-5cm	100	48.6	2.3	5.5	790	2.2	4	10	302.7
6T-5cm	100	51	1.5	3.1	790	2.2	6	16	303.4
1T-8cm	100	78	11	-	790	2.2	1	4	313.1
2T-8cm	100	81.4	3	3.3	790	2.2	2	6	302.3
4T-8cm	100	80	1.3	1.6	790	2.2	4	12	302.5
6T-8cm	100	80.4	0.8	1	790	2.2	6	19	302.5

Table V.2 MTMG TLR designs for 7 T and predicted resonance frequencies

### V.5.2. Bench evaluation of MTMG TLRs at 7 T

The fabricated MTMG TLRs were characterized on the bench by measuring their resonance frequency and Q-factor with the single-loop probe method. A comparison between the theoretically predicted resonance frequencies and those measured in bench experiments is

shown in Table V.3. The table also contains the respective deviations from the Larmor frequency (297.2 MHz) and the measured unloaded Q factors.

It was found that the measured resonance frequencies deviate up to 23 % from the theoretically predicted values, and that, therefore, only two of the nine MTMG TLRs can be directly used for MRI. In order to increase the number of usable TLRs, the innermost turn of the structures which had a resonance frequency much lower than the Larmor frequency was removed. This way, one additional MTMG TLR resonating close to the Larmor frequency of interest could be generated: the 6T-5cm TLR was transformed into a 5T-6cm TLR.

Name	$f_0$ model [MHz]	$f_0$ bench [MHz]	$\frac{f_0 \text{ bench} - f_0 \text{ model}}{f_0 \text{ bench}}$	$\frac{f_0 \text{ bench} - f_0 \text{ Larmor}}{f_0 \text{ bench}}$	$Q_{\text{unloaded}}$
2T-3cm	301.3	332	9 %	10 %	106
4T-3cm	302.5	271	-12 %	-10 %	201
6T-3cm	305.0	248	-23 %	-20 %	212
1T-5cm	287.9	356	19 %	17 %	135
2T-5cm	302.4	318	5 %	7 %	116
4T-5cm	302.7	257	-18 %	-16 %	227
6T-5cm	303.4	261	-16 %	-14 %	212
1T-8cm	313.1	343	9 %	13 %	109
2T-8cm	302.3	294	-3 %	-1 %	137
4T-8cm	302.5	264	-15 %	-13 %	198
6T-8cm	302.5	261	-16 %	-14 %	148
5T-6cm	354.4	303	-17 %	2 %	106

Table V.3 Measured resonance frequencies and Q-factors for the 7 T MTMG TLRs

### V.5.3. EM field simulation and $B_1$ mapping

The performance of the three MTMG TLRs resonating at approximately 300 MHz was evaluated in FDTD simulations in combination with circuit co-simulation, and MR measurements. The MTMG TLRs were fine-tuned and matched inductively with a 5-cm pick-up loop placed at a distance of 4 cm above the TLRs. 3D EMS were used to simulate the current density distribution in front and back conductors, and to estimate  $B_1^+$  profiles normalized to 1 W input power  $P$ . Further, 10g-averaged SAR values were calculated.

Simulation results are summarized in Figure V.11. The simulated current density distributions show that the current is maximal at the center of the conducting strips and minimal at their ends.

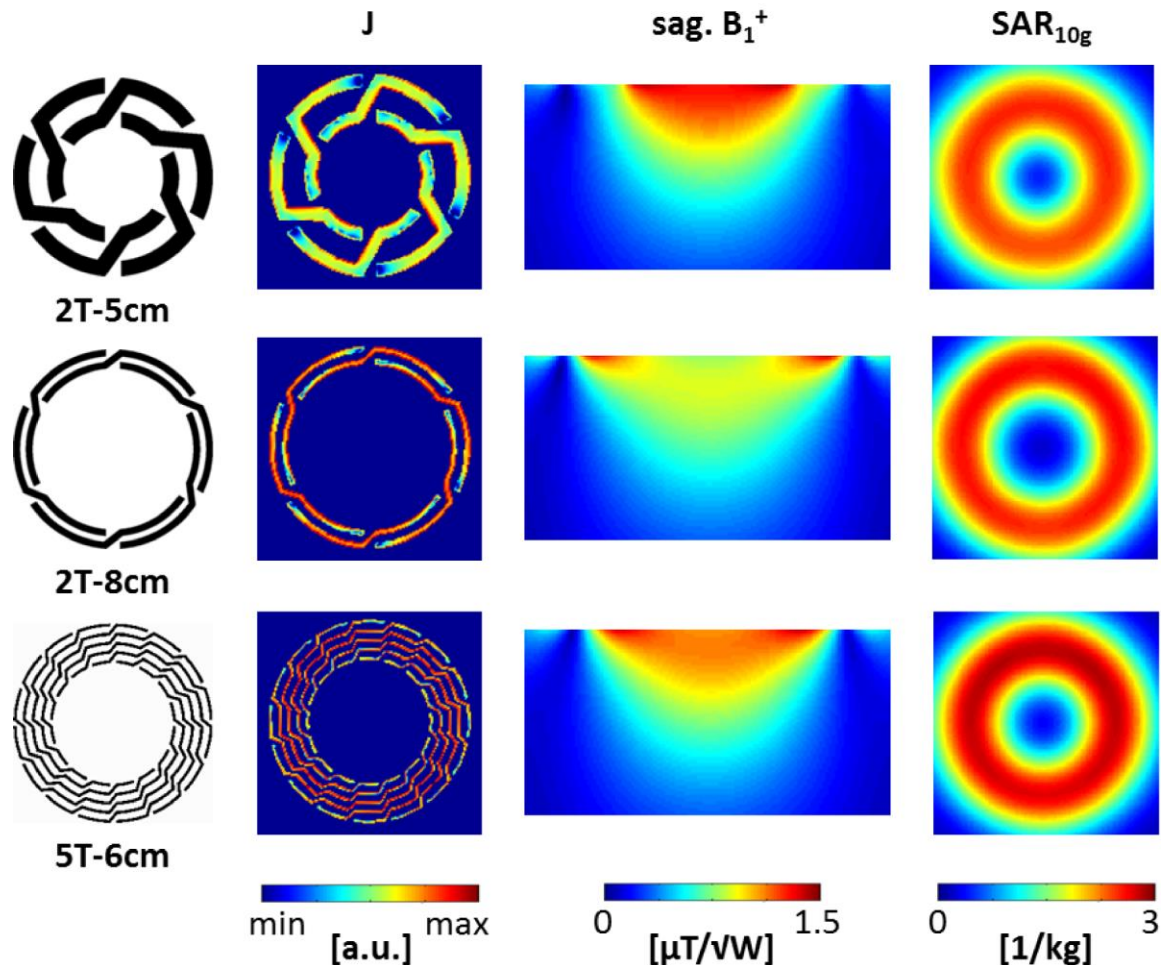


Figure V.11 Simulated current density,  $B_1$  and SAR distribution for MTMG TLRs

The simulated  $B_1^+$  profiles show that the  $B_1$  distribution varies strongly for the compared coil designs. While the 2T-5cm TLR produces a high  $B_1^+$  over a narrow lateral FOV, the 2T-8cm TLR generates a lower  $B_1^+$  but over a broader FOV; the  $B_1^+$  profile of the 5T-6cm TLR appears to represent a compromise between the former two.

Maximum intensity projections (MIPs) of the simulated 10g-averaged SAR vary slightly in spatial distribution with the inner diameter of the investigated MTMG TLRs. Further, it can

be observed that the SAR values are highest for the 5T-6cm TLR. This might be related to the high density of turns or the high number of gaps for this design, and a higher current amplitude potentially resulting therefrom.

In MRI experiments, 3D GRE images and flip angle maps employing the satTFL method [101] using a sinc-shaped slice-selective saturation pulse (2 ms pulse duration, 100 V reference amplitude) were acquired. Flip angle maps are shown in Figure V.12. The acquired flip angle maps are qualitatively in good agreement with the simulated  $B_1^+$  maps.

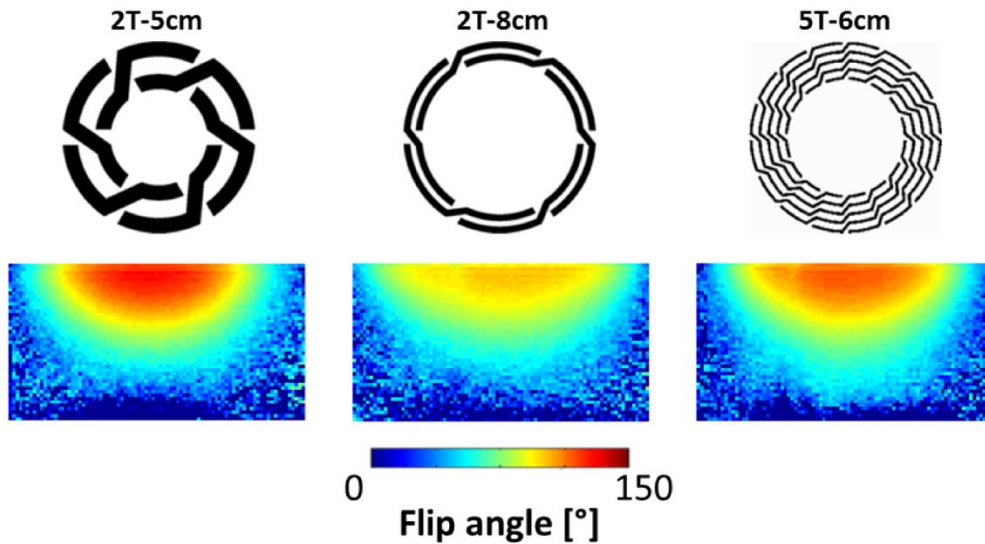


Figure V.12 Flip angle maps acquired with the selected MTMG TLRs

It should be noted that the distance between the TLRs and the phantom was 4 mm in simulations and 12 mm in experiments; this explains the discrepancy at the top of the images. A quantitative comparison between simulations and measurements was not performed; therefore realistic coil losses (for TLR and pick-up loop) would have to be included in the simulation, and losses of the transmit and the receive chain of the experimental setup would have to be determined.

## **Chapter VI Discussion, Conclusions and Perspectives**



## **VI.1. Flexible TLR array**

### **VI.1.1. Summary**

The primary goal of this thesis was the development of a flexible TLR array for proton MRI at 7 T. TLRs were chosen for the individual array elements because this coil design enables the fabrication of auto-resonant monolithic RF coils without using lumped element capacitors, which may be form-fitted to various sample geometries. To reach the objectives of this thesis, and to optimize the developed TLR array, the mutual coupling between TLRs was investigated in detail, and several matching networks suitable for monolithic TLRs were intensely studied and compared. Experimental methods were combined with analytical and numerical simulations employing state-of-the-art technology in order to enable the development and implementation of the first flexible TLR array for MRI.

A detailed discussion of the benefits of the novel decoupling technique, of the development of a four-element prototype array and its potential biomedical applications is given in section III.5.

### **VI.1.2. Ways to improve the developed TLR array**

As an alternative to the resonant inductive matching scheme used for the four-element TLR array developed in this work, the capacitive matching network presented in section V.2 could be used. One advantage of capacitive matching is that coupling between TLRs due to the mutual coupling between pick-up loops can be avoided. Further, the introduction of additional circuitry for transmission decoupling (presented in section V.3) and preamplifier decoupling is enabled, in the case that the array should be used in receive-only mode.

However, the capacitive matching network has to be connected to the TLR via solder joints which might crack upon bending. This issue could be resolved by fabricating an array that consists of rigid as well as flexible parts, as schematically depicted in Figure VI.1. This way, the form-fitting ability of the TLR array could be preserved, while preventing damage of the required solder joints.

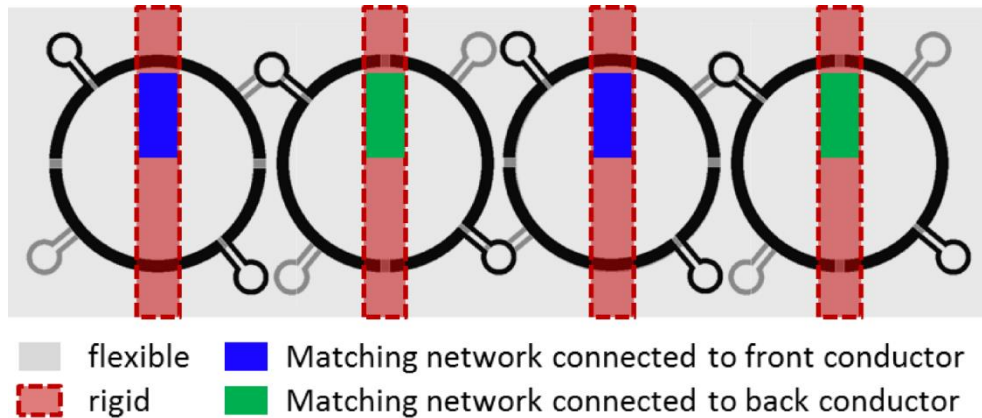


Figure VI.1 Conception of a capacitively matched flexible TLR array

Besides employing an alternative matching scheme, another possibility to improve the array performance is to investigate other annex geometries. This might be necessary when employing the proposed decoupling technique for small TLRs at lower field strength, e.g. 1.5 T. In this case, it should be taken into account that adding the decoupling annexes increases the coil noise (see section IV.3.2), and therefore, also increases the coil diameter for which coil noise becomes dominant [106]. The noise contribution from the annexes can be reduced by increasing the width of the conductors forming the annexes. Thereby, a compromise between annex size, inter-element spacing and conductor width has to be found.

In this work, the annex size was optimized using 3D EMS. In order to save time while designing TLR arrays in future work, an analytical model to determine the optimal annex size would be desirable. Further, an alternative decoupling scheme, or a modification of the presented technique would be required for TLR arrays fabricated on thick dielectric substrates, e.g. 1.5 mm thick FR4 plates. In this case, the magnetic flux shared by the annexes might be insufficient to cancel the flux shared by the main windings for reasonable annex diameters, depending on the TLR diameter and inter-element spacing.

In the developed prototype array the diagonally neighboring elements are not decoupled by overlapping annexes. For the chosen array configuration this did not cause difficulties in any of the performed MR imaging experiments when the array was sufficiently loaded.

Nonetheless, decoupling of diagonal elements would be desirable so as to further improve the decoupling and parallel imaging performance of TLR arrays. The coupling between diagonal or next-nearest neighbor elements may be reduced by switching from a tetragonal to a hexagonal placing scheme for the TLRs within the array, as depicted in Figure VI.2.

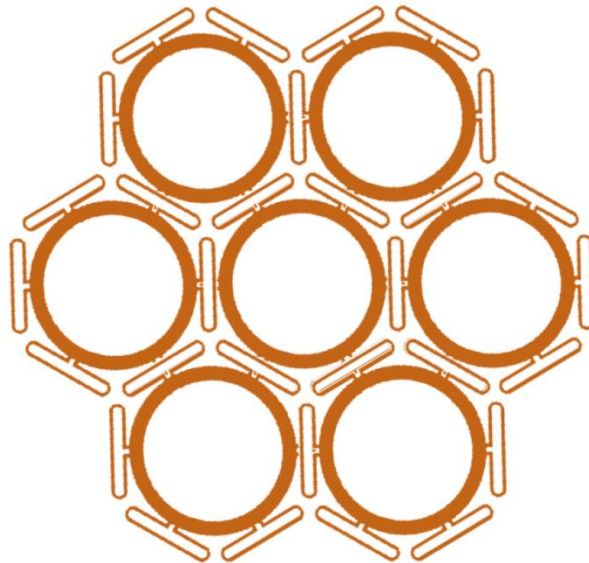


Figure VI.2 Schematic drawing of a hexagonally arranged TLR array

In this case, there are six nearest neighbors for each TLR element, which implies the need for six decoupling annexes per coil (three per conductor). In order to equilibrate the current density among all decoupling annexes, and to achieve efficient decoupling between all neighboring elements, three gaps per conductor would be needed.

### VI.1.3. Potential applications for flexible TLR arrays

Skin imaging has been named as a prospective biomedical application of flexible TLR arrays in section III.5. Another example would be imaging of the human heart. Cardiac MRI, is a viable non-invasive tool to investigate coronary arteries and ischemic tissue (infarction) [132], in particular using high resolution MRI with parallel imaging techniques. The technological concepts developed in this thesis could be employed to construct a form-fitted high-performance coil array for human cardiac MR studies at 7 T. Potential challenges during

the development of such a device are the search for a suitable matching strategy that will provide robust tuning and matching for various patient anatomies without performing adjustments before each examination, and to find the optimal operation mode during RF transmission in view of SAR and  $B_1^+$  efficiency. Further, a suitable coil housing will have to be constructed, that ensures mechanical stability, as well as patient safety and comfort. In view of required penetration depth and FOV, the diameter of the individual elements will be in a range for which sample noise usually clearly dominate over internal coil noise.

## VI.2. Multi-turn multi-gap TLRs for MRI

In this thesis, also a novel TLR design has been presented - the multi-turn multi-gap (MTMG) TLR. The novel design expands the parameter space for TLR geometries in a way that high-field MRI applications requiring a large FOV, like most biomedical applications, can be addressed by multi-turn TLR technology, which was not possible up to now. The reason for this limitation was the intrinsically low resonance frequency of large MTLRs resulting from their high inductance. The MTMG TLR design exploits the fact that the resonance frequency of the TLR increases almost linearly with the number of gaps. Up to now, resonators with more than one gap per conducting band existed only in single-turn configuration because no design scheme for multiple turns was available.

The MTMG TLR design was tested in a first prototype study at 4.7 T, and in a study including various MTMG TLRs at 7 T. It was demonstrated that MTMG TLRs can be used for MR imaging and that they can be form-fitted to non-planar sample surfaces. Further, the comparison of three different MTMG TLRs at 7 T showed that the  $B_1$  distribution of the individual TLRs varies strongly with the number of turns and with the spatial arrangement of the turns in the coil plane. This demonstrates that the additional degree of freedom in TLR design, does not only affect the self-resonance frequency, but also the sensitivity profiles of the TLRs. This fact could be exploited in future studies to design MTMG TLRs for applications that require a specific  $B_1$  distribution. In future work, also the applicability of the analytical model for calculating the TLR resonance frequency to the MTMG TLR design will have to be investigated in more detail.

Although the MTMG TLR design is expected to benefit primarily biomedical UHF MRI applications, it is applicable for any field strength or coil size. The additional degree of freedom in TLR design enables more accurate optimization of coil geometry, current distribution, and  $B_1$  pattern, also for small low-frequency MTLRs, and in principle also for superconducting coils. On the one hand, it can be used to increase the number of turns for a given TLR geometry; on the other hand, the MTMG TLR design may also be employed to increase the number of gaps. For instance, the array design shown in Figure VI.2 requires

three gaps per conductor. Since the resonance frequency increases with the number of gaps, this requirement may become a limiting factor for the minimum usable element diameter. With the MTMG TLR design, the number of turns can be increased in order to compensate for the high resonance frequency.

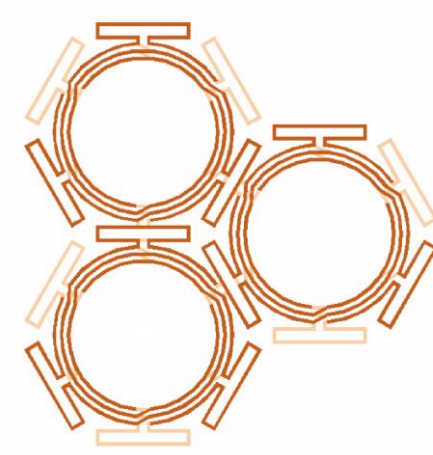


Figure VI.3 Concept for a MTMG TLR array

A possible design scheme for an MTMG TLR array with decoupling annexes is shown in Figure VI.3. The feasibility and applicability of this and similar designs will be investigated in future work.

### **VI.3. Conclusion**

In conclusion, this thesis describes novel technological concepts for the development of mechanically flexible high-field NMR probes based on monolithic transmission line resonators. The developed TLR array enables to exploit the high SNR of small coils for an extended field of view, and gives access to parallel imaging techniques for accelerated image acquisition, as well as  $B_1^+$  shimming. The possibility to form-fit the RF coil to the investigated anatomical region can be exploited to increase the detection sensitivity in MR imaging examinations.

# **Appendix**



## A.1. Resonance condition of TLRs

The analytical model for TLRs introduced in section II.4.4.1 has been developed by Gonord and Kan [53]. An internal document that provides a step-by-step derivation of the resonance condition (Equation II.29) is available at IR4M at Université Paris Sud (France) in French language. This chapter is a reproduction of that document in English.

Information about recent progress in analytical modeling of TLRs can be found in the PhD thesis of Li Zhoujian (Université Paris Sud, école doctorale STITS, expected 2015).

### *Description of the resonator*

The investigated resonators consist of circularly shaped transmission lines. Each of the two conductors composing the line is intersected by one or several gaps, where the number of gaps is equal for the two windings on top and bottom of the dielectric substrate. The gaps are alternately positioned along both conductors. This way, the resonator can be described as a sequence of segments as shown in Figure A.1.

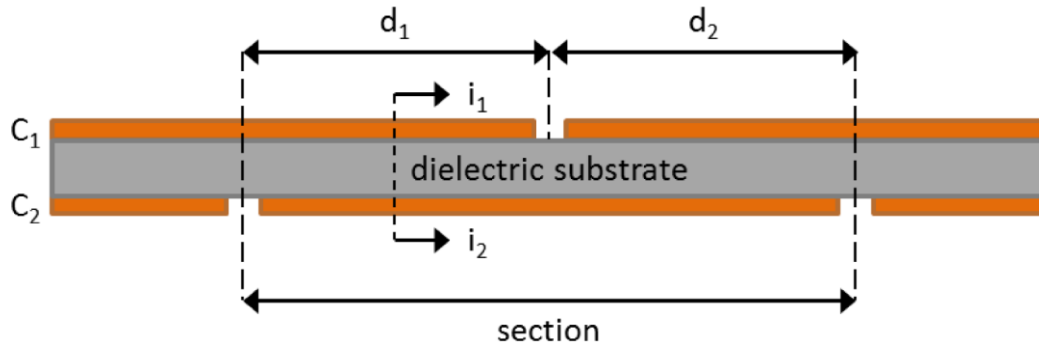


Figure A.1 Segmentation of the transmission line

Let  $i_1$  and  $i_2$  be the currents present at a given position in the two conductors  $C_1$  and  $C_2$ . They can be described as the superposition of two currents, the differential mode current  $i_D$  and the common mode current  $i_C$ :

$$i_D = \frac{i_1 - i_2}{2} \quad \text{and} \quad i_C = \frac{i_1 + i_2}{2} \quad \text{A.1}$$

$$i_1 = i_C + i_D \quad \text{and} \quad i_2 = i_C - i_D \quad \text{A.2}$$

The differential mode current does not create a magnetic field outside of the transmission line. For a perfect transmission line, the differential mode shows no interaction with the surrounding. This mode depends only on intrinsic properties of the transmission line, such as its inductance, capacitance, characteristic impedance  $Z_0$  and propagation constant  $\beta$ . The differential mode current varies with the position along the line.

In contrast, the common mode current is responsible for the creation of the external magnetic field – as the current in a conventional loop of wire. At the frequencies of interest, where the wave length is large compared to the circuit dimensions, this current can be described in the quasi-static regime rather than by antenna theory. Therefore, the common mode current can be considered constant along the transmission line.

The differential and common mode currents fulfill the following boundary conditions at the respective gaps along the conductors:

$$\text{for } C_1: i_1 = 0 \quad \text{and therefore} \quad i_C = -i_D \quad \text{A.3}$$

$$\text{for } C_2: i_2 = 0 \quad \text{and therefore} \quad i_C = i_D \quad \text{A.4}$$

### ***The differential mode***

The voltage across the line at position  $x$  is denoted by  $v(x)$ , and  $v_P$  denotes the voltage at a certain plane P, e.g.  $P = 4n$  (see Figure A.2). Further, the differential mode current is denoted by  $i_D(x)$  and  $i_{DP}$ , respectively. The symbol  $j$  represents the imaginary unit. The classical transmission line equations for the voltage and current along the line are given by:

$$v(x) = v(0) \cos(\beta x) - jZ_0 i_D(0) \sin(\beta x) \quad \text{A.5}$$

$$i_D(x) = i_D(0) \cos(\beta x) - jv(0)/Z_0 \sin(\beta x) \quad \text{A.6}$$

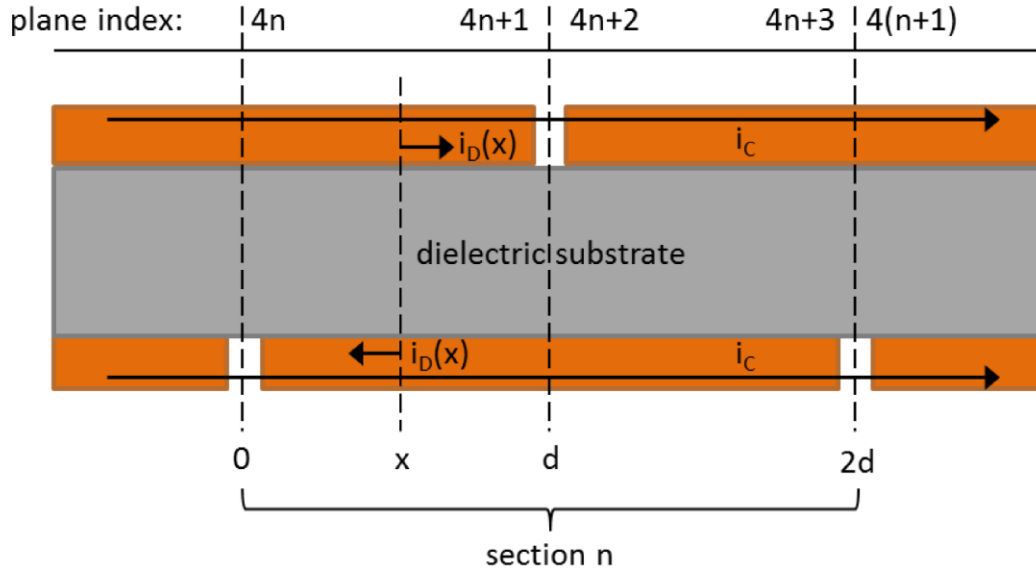


Figure A.2 Index planes along the TLR

The following shortcuts are used to simplify the equations:

$$\zeta_D = Z_0 i_D \quad \text{and} \quad \zeta_C = Z_0 i_C \quad \text{A.7}$$

Then, the transmission line equations can be written in the following form:

$$v(x) = v(0) \cos(\beta x) - j\zeta_D(0) \sin(\beta x) \quad \text{A.8}$$

$$\zeta_D(x) = \zeta_D(0) \cos(\beta x) - jv(0) \sin(\beta x) \quad \text{A.9}$$

As a consequence of the boundary conditions, the following relations between differential and common mode current hold:

$$i_2 = 0 \text{ at } x = 0 \rightarrow \zeta_{D4n} = \zeta_C \quad \text{A.10}$$

$$i_1 = 0 \text{ at } x = d \rightarrow \zeta_{D4n+1} = -\zeta_C \quad \text{A.11}$$

which imposes at  $x = d$

$$\zeta_{D4n+1} = \zeta_C \cos(\beta d) - jv_{4n} \sin(\beta d) \quad \text{A.12}$$

Combining equations A.11 and A.12, one obtains the following expression for the voltage  $v_{4n}$  at position  $x = 0$ :

$$v_{4n} = -j\zeta_C \frac{1 + \cos(\beta d)}{\sin(\beta d)} = -j\zeta_C \cot\left(\frac{\beta d}{2}\right) =: U \quad \text{A.13}$$

By inserting this expression in the transmission line equations A.8 and A.9, one obtains

$$v_{4n+3} = v_{4n+2} = -v_{4n} = -v_{4n+1} = j\zeta_C \cot\left(\frac{\beta d}{2}\right) \quad \text{A.14}$$

$$\zeta_{D4n+3} = -\zeta_{D4n+2} = -\zeta_{D4n+1} = \zeta_{D4n} = \zeta_C \quad \text{A.15}$$

Figure A.3 shows the voltages and currents occurring in the transmission line according to this derivation. The voltage across the gaps in the conductors is given by  $u_g = 2U$ .

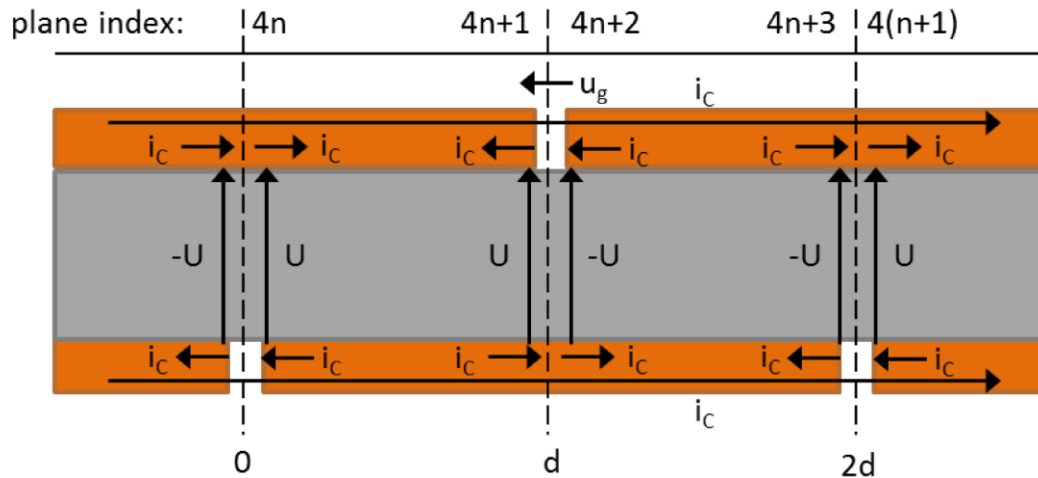


Figure A.3 Voltages and currents along the transmission line

### *The common mode*

The magnetic flux seen from outside of the TLR is created by the common mode current, while the differential mode current does not directly interact with the surroundings of the resonator. Figure A.4 shows a single-turn double-gap TLR seen from an external point of view.

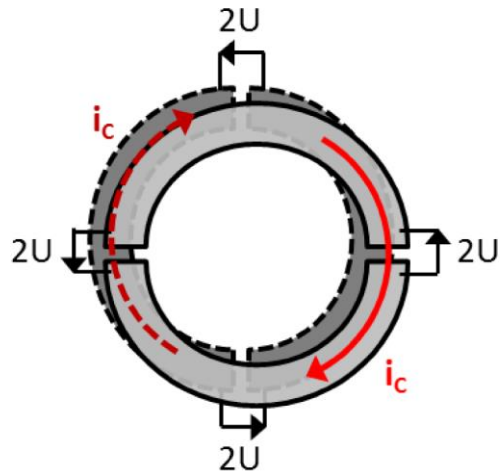


Figure A.4 TLR seen from an external point of view

The corresponding equivalent circuit (in the quasi-static approximation) is shown in Figure A.5, where  $L_1$  and  $L_2$  are the inductances of the conductors  $C_1$  and  $C_2$ , and  $M$  is their mutual inductance.

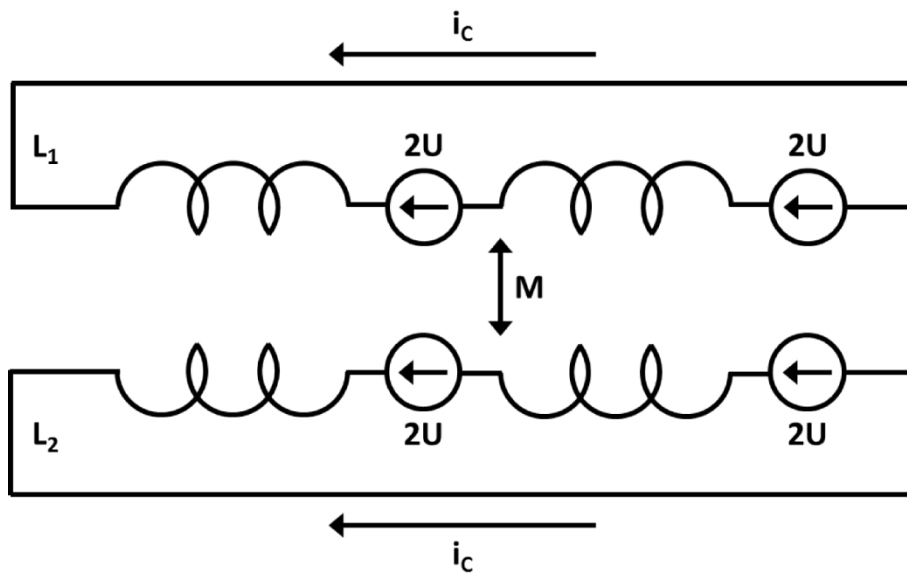


Figure A.5 Pseudo-equivalent circuit for a TLR

To have the same current  $i_C$  in both turns, the two conductors should be placed in series in the equivalent circuit. To do so, it is necessary to calculate the total inductance  $L_{tot}$  of the resonator.

$$L_{tot} = L_1 + L_2 + 2M \quad A.16$$

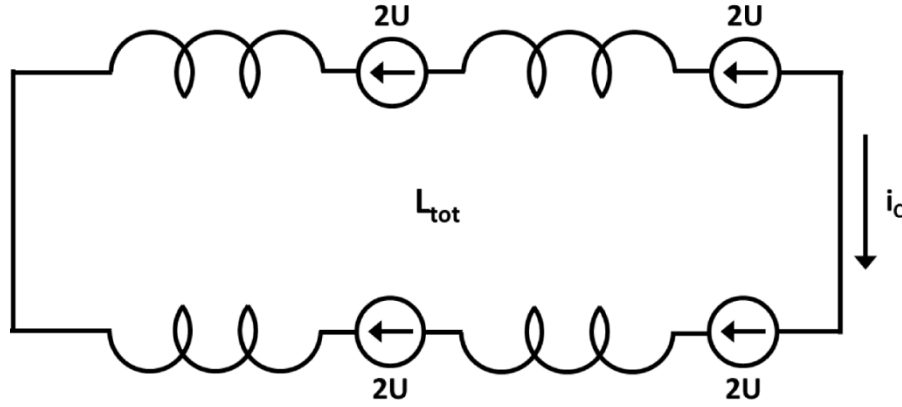


Figure A.6 TLR equivalent circuit with total inductance  $L_{tot}$

Figure A.6 shows the closed equivalent circuit for a single-turn double-gap TLR, which can be easily extended to an arbitrary number of gaps. According to Kirchoff's voltage law, for a closed circuit composed of  $N_g$  sections, where  $N_g$  is the number of gaps per conductor, the following expression containing the angular resonance frequency  $\omega_0$  holds true:

$$jL_{tot}\omega_0 i_C + 4N_g U = 0 \quad A.17$$

### ***The resonance condition***

Combing the equations for differential and common mode (Equations A.14 and A.17), one obtains an implicit expression for the angular resonance frequency.

$$jL_{tot}\omega_0 i_C - j4N_g Z_0 i_C \cot\left(\frac{\beta d}{2}\right) = 0 \quad A.18$$

$$L_{tot}\omega_0 - 4N_g Z_0 \cot\left(\frac{\beta d}{2}\right) = 0, \text{ for } i_C \neq 0 \quad A.19$$

$$\frac{L_{\text{tot}}\omega_0}{4N_g Z_0} \tan\left(\frac{\beta d}{2}\right) = 1 \quad \text{A.20}$$

With the total length of the transmission line  $l_f = 2dN_g$  this becomes

$$\frac{L_{\text{tot}}\omega_0}{4N_g Z_0} \tan\left(\frac{\beta l_f}{4N_g}\right) = 1 \quad \text{A.21}$$

With the propagation constant

$$\beta = \frac{2\pi}{\lambda} = \frac{2\pi f \sqrt{\epsilon}}{c} \quad \text{A.22}$$

equation A.21 can be written in the form of equation II.29:

$$\frac{L_{\text{tot}}\omega_0}{4N_g Z_0} \tan\left(\frac{\omega_0 \sqrt{\epsilon} l_f}{4N_g c}\right) = 1 \quad \text{A.23}$$

The characteristic impedance of the transmission line  $Z_0$  and the total inductance can be calculated using equations II.30 - II.38.

## **A.2. Automated mask generation**

Transmission line resonators can be fabricated from copper plated dielectric substrates by photolithographic etching, comparable to printed circuit boards (PCB). Several facilities are needed for the fabrication process, e.g. a UV light source and the photographic developer (chemical solution). However, even if all required equipment and materials are available, the fabrication process can be very time consuming and often results are unsatisfactory. Common problems are for instance the aging of the photo-resistive layer on the copper plated dielectrics, insufficient protection from daylight, inaccuracy of the exposure time, and problems with mask alignment for double sided structures. In order to save time and to avoid these difficulties the fabrication process can be subcontracted.

In this case, the fabrication will be performed by a so-called CAM-machine (computer-aided manufacturing). The desired designs (“layouts”) have to be drawn and provided in one of the following file formats: dxf, dwg, or gerber. The data has to be organized in separate layers. For a TLR there will be a top and a bottom layer of conducting material, and an outline layer defining the overall size of the fabricated board.

The conductor shape is indicated by drawing only the boundary (not a filled face) of the area covered by copper. A valid boundary consists of a series of straight segments forming a closed area, i.e. the first and the last vertex must be the same. The inside of the closed boundary will be automatically interpreted as solid. Also the boundary should neither overlap with itself nor self-intersect, it may however, touch itself. The segments of the boundary should be formed by zero-width poly-lines, i.e. connections between two points which have by definition a width of zero. In principle, arcs and circles could be used in addition to straight lines to draw a boundary but it is not recommended, because it is not supported by some (few) CAM-interpreters. Further, a boundary must be unidirectional, i.e. the segments forming the boundary have to be put together in the right order, all following the same orientation. The top and all intermediate (for multi-layer structures) as well as the bottom layer have to be drawn from top view. It is also important to set the origin at a well-defined location, for example the center or in one of the corners of the designed board.



## Mask Drawing Software

The acceptable file formats limit the usable graphical software packages to those that can export data in at least one of these formats. There are several open source PCB drawing software packages available (e.g. KiCAD, EagleFree, etc.) but they are not well suited for the purpose of TLR design, since they focus on the circuit components to be integrated on the board rather than on the conductor geometry. The need for quite complex conductor shapes and the limitation in output formats suggests the use of a *full* CAD software. The commercial software AutoCAD is widely used to draw masks for microelectronic circuits. However, AutoCAD licenses are quite expensive. Alternatively, several Open Source CAD tools exist. The one that appeared most suitable for the task is called FreeCAD ([www.freecadweb.org](http://www.freecadweb.org)). It is 100% Open Source and runs on Windows, Mac OSX and Linux platforms. FreeCAD can be operated via a graphical user interface (GUI), or alternatively via python scripts ([www.python.org](http://www.python.org)).

In the scope of this thesis, two different FreeCAD macros for TLR mask design have been written in python: one to draw single TLR coils with user-defined number of turns and gaps (*DraftMTLR\_2.FCmacro*), and the other to draw TLR arrays with overlapping annexes for mutual decoupling (*DraftArrayMTLR\_2.FCmacro*).

```
8
9 dext = float(100e-3)
10 w = float(3e-3)
11 esp = float(6.9e-3)
12 N = int(4)
13 Ng = int(3)
14 g = w
15
16 #circles are approximated by segments, maximum length of one segment:
17 b = float(1e-3)
18
19 #set parameters for outline
20 s = float(dext/10) #spacing between structure and outline
21 th = float(s) #width of outline
22
```

Figure A.7 Input parameters of the single coil macro

The macros produce a top and a bottom layer containing the conductor shapes and an outline layer containing the margins of the antenna board. In the first section of the script the user may define the geometric parameters of the designed TLR. After entering the geometric parameters, saving and running the macro, the produced drawing can be inspected in the FreeCAD GUI; then the data can be exported to dxf-files layer by layer.

### *Creating gerber files*

Although dxf-files are generally accepted, most companies prefer gerber data. A gerber file can be regarded as an intermediate step between a dxf-drawing and CAM-output. For each layer there is a separate gerber file; a double-layer board requires minimum three files, for example Top.gbr, Bottom.gbr and Outline.gbr – these are sufficient for a standard TLR design. In addition, a text file describing the purpose of each .gbr file has to be sent to the company together with the gerber data. The text file should include important information for the fabrication, e.g. substrate material, substrate thickness, copper thickness etc.

In this work, the professional PCB layout tool DipTrace ([www.diptrace.com](http://www.diptrace.com), Novarm Limited, USA) was used to convert the generated dxf-files to gerber data. In DipTrace it is also possible to import dxf models of several TLRs and to arrange them manually in a way to fill a complete panel for fabrication (30.5 cm x 45.7 cm in our case).

# Bibliography

- [1] F. Bloch, Nuclear Induction, *Phys. Rev.* 70 (1946) 460–474.
- [2] E.M. Haacke, R.W. Brown, M.R. Thompson, *Magnetic Resonance Imaging Physical Principles and Sequence Design*, John Wiley & Sons, Inc., New York, USA, 1999.
- [3] E.L. Hahn, Spin Echoes, *Phys. Rev.* 80 (1950) 580–594.
- [4] H.Y. Carr, E.M. Purcell, Effects of Diffusion on Free Precession in Nuclear Magnetic Resonance Experiments, *Phys. Rev.* 94 (1954) 630–638.
- [5] W.A. Edelstein, J.M.S. Hutchison, G. Johnson, T. Redpath, Spin warp NMR imaging and applications to human whole-body imaging, *Phys. Med. Biol.* 25 (1980) 751.
- [6] P.C. Lauterbur, Image Formation by Induced Local Interactions: Examples Employing Nuclear Magnetic Resonance, *Nature.* 242 (1973) 190–191.
- [7] A.N. Garroway, P.K. Grannell, P. Mansfield, Image formation in NMR by a selective irradiative process, *J. Phys. C Solid State Phys.* 7 (1974) L457.
- [8] C.J. Hardy, H.E. Cline, Spatial localization in two dimensions using NMR designer pulses, *J. Magn. Reson.* 82 (1989) 647–654.
- [9] J.M. Pauly, B.S. Hu, S.J. Wang, D.G. Nishimura, A. Macovski, A three-dimensional spin-echo or inversion pulse, *Magn. Reson. Med.* 29 (1993) 2–6.
- [10] U. Katscher, P. Börnert, C. Leussler, J.S. van den Brink, Transmit SENSE., *Magn. Reson. Med.* 49 (2003) 144–150.
- [11] A. Kumar, D. Welti, R.R. Ernst, NMR Fourier zeugmatography, *J. Magn. Reson.* 18 (1975) 69–83.
- [12] D.B. Twieg, The k-trajectory formulation of the NMR imaging process with applications in analysis and synthesis of imaging methods, *Med. Phys.* 10 (1983) 610–621.
- [13] S. Ljunggren, A simple graphical representation of Fourier-based imaging methods, *J. Magn. Reson.* 54 (1983) 338–343.
- [14] J.W. Carlson, T. Minemura, Imaging time reduction through multiple receiver coil data acquisition and image reconstruction, *Magn. Reson. Med.* 29 (1993) 681–687.

- [15] J.B. Ra, C.Y. Rim, Fast imaging using subencoding data sets from multiple detectors, *Magn. Reson. Med.* 30 (1993) 142–145.
- [16] P.B. Roemer, W.A. Edelstein, C.E. Hayes, S.P. Souza, O.M. Mueller, The NMR phased array., *Magn. Reson. Med.* 16 (1990) 192–225.
- [17] D.K. Sodickson, W.J. Manning, Simultaneous acquisition of spatial harmonics (SMASH): fast imaging with radiofrequency coil arrays, *Magn. Reson. Med.* 38 (1997) 591–603.
- [18] K.P. Pruessmann, M. Weiger, M.B. Scheidegger, P. Boesiger, SENSE: sensitivity encoding for fast MRI., *Magn. Reson. Med.* 42 (1999) 952–962.
- [19] P.M. Jakob, M.A. Griswold, R.R. Edelman, D.K. Sodickson, AUTO-SMASH: A self-calibrating technique for SMASH imaging, *Magn. Reson. Mater. Physics, Biol. Med.* 7 (1998) 42–54.
- [20] R.M. Heidemann, M.A. Griswold, A. Haase, P.M. Jakob, VD-AUTO-SMASH imaging., *Magn. Reson. Med.* 45 (2001) 1066–1074.
- [21] M.A. Griswold, P.M. Jakob, R.M. Heidemann, M. Nittka, V. Jellus, J. Wang, B. Kiefer, A. Haase, Generalized autocalibrating partially parallel acquisitions (GRAPPA)., *Magn. Reson. Med.* 47 (2002) 1202–1210.
- [22] M. Blaimer, F. Breuer, M. Mueller, R.M. Heidemann, M.A. Griswold, P.M. Jakob, Smash, Sense, Pils, Grappa, *Top. Magn. Reson. Imaging.* 15 (2004) 223–236.
- [23] M. Weiger, K.P. Pruessmann, P. Boesiger, 2D SENSE for faster 3D MRI., *Magn. Reson. Mater. Physics, Biol. Med.* 14 (2002) 10–19.
- [24] K.P. Pruessmann, M. Weiger, P. Börnert, P. Boesiger, Advances in sensitivity encoding with arbitrary k-space trajectories., *Magn. Reson. Med.* 46 (2001) 638–651.
- [25] D.I. Hoult, R.E. Richards, The Signal-to-Noise Ratio of the Nuclear Magnetic Resonance Experiment, *J. Magn. Reson.* 24 (1976) 71–85.
- [26] D.I. Hoult, The Principle of Reciprocity in Signal Strength Calculations - A Mathematical Guide, *Concepts Magn. Reson.* 12 (2000) 173–187.
- [27] C.W. Helstrom, Probability and stochastic processes for engineers, Maxwell, Macmillan, New York, USA, 1991.
- [28] H. Nyquist, Thermal Agitation of Electric Charge in Conductors, *Phys. Rev.* 32 (1928) 110–113.

- [29] C. Gabriel, S. Gabriel, E. Corthout, The dielectric properties of biological tissues: I. Literature survey., *Phys. Med. Biol.* 41 (1996) 2231–2249.
- [30] M. Decorps, P. Blondet, H. Reutenauer, J.P. Albrand, C. Remy, An inductively coupled, series-tuned NMR probe, *J. Magn. Reson.* 65 (1985) 100–109.
- [31] D.I. Hoult, N.S. Ginsberg, The quantum origins of the free induction decay signal and spin noise., *J. Magn. Reson.* 148 (2001) 182–199.
- [32] D.I. Hoult, P.C. Lauterbur, The sensitivity of the zeugmatographic experiment involving human samples, *J. Magn. Reson.* 34 (1979) 425–433.
- [33] L. Darrasse, J.-C. Ginefri, Perspectives with cryogenic RF probes in biomedical MRI, *Biochimie.* 85 (2003) 915–937.
- [34] W.A. Edelstein, G.H. Glover, C.J. Hardy, R.W. Redington, The intrinsic signal-to-noise ratio in NMR imaging., *Magn. Reson. Med.* 3 (1986) 604–618.
- [35] A. Abragam, *Principles of Nuclear Magnetism*, Oxford University Press, 1961.
- [36] C.N. Chen, D.I. Hoult, *Biomedical Magnetic Resonance Technology*, Adam Hilger, Bristol, 1989.
- [37] C.M. Collins, Z. Wang, Calculation of radiofrequency electromagnetic fields and their effects in MRI of human subjects., *Magn. Reson. Med.* 65 (2011) 1470–1482.
- [38] D.I. Hoult, Sensitivity and power deposition in a high-field imaging experiment., *J. Magn. Reson. Imaging.* 12 (2000) 46–67.
- [39] C.M. Collins, W. Liu, W. Schreiber, Q.X. Yang, M.B. Smith, Central brightening due to constructive interference with, without, and despite dielectric resonance., *J. Magn. Reson. Imaging.* 21 (2005) 192–196.
- [40] P.-F. Van de Moortele, C. Akgun, G. Adriany, S. Moeller, J. Ritter, C.M. Collins, M.B. Smith, J.T. Vaughan, K. Ugurbil, B1 destructive interferences and spatial phase patterns at 7 T with a head transceiver array coil., *Magn. Reson. Med.* 54 (2005) 1503–1518.
- [41] P.A. Bottomley, E.R. Andrew, RF magnetic field penetration, phase shift and power dissipation in biological tissue: implications for NMR imaging, *Phys. Med. Biol.* 23 (1978) 630.
- [42] A. Haase, F. Odoj, M. von Kienlin, J. Warnking, F. Fidler, A. Weisser, M. Nittka, E. Rommel, T. Lanz, B. Kalusche, M. Griswold, NMR Probeheads for In Vivo Applications, *Concepts Magn. Reson.* 12 (2000) 361–388.

- [43] F. Bloch, W.W. Hansen, M. Packard, The Nuclear Induction Experiment, *Phys. Rev.* 70 (1946) 474–485.
- [44] D.M. Ginsberg, Optimum Geometry of Saddle Shaped Coils for Generating a Uniform Magnetic Field, *Rev. Sci. Instrum.* 41 (1970) 122.
- [45] A.G. Webb, Radiofrequency microcoils in magnetic resonance, *Prog. Nucl. Magn. Reson. Spectrosc.* 31 (1997) 1–42.
- [46] E. Laistler, B. Dymerska, J. Sieg, E. Moser, A homogeneity-optimized solenoid coil for 7T microimaging, in: *Proc. ESMRMB, Lisbon, Portugal, 2012*: p. 433.
- [47] C.E. Hayes, W.A. Edelstein, J.F. Schenck, O.M. Mueller, M. Eash, An efficient, highly homogeneous radiofrequency coil for whole-body NMR imaging at 1.5 T, *J. Magn. Reson.* 63 (1985) 622–628.
- [48] J.J.H. Ackerman, T.H. Grove, G.G. Wong, D.G. Gadian, G.K. Radda, Mapping of metabolites in whole animals by  $^{31}\text{P}$  NMR using surface coils, *Nature.* 283 (1980) 167–170.
- [49] O. Beuf, F. Jaillon, H. Saint-Jalmes, Small-animal MRI: signal-to-noise ratio comparison at 7 and 1.5 T with multiple-animal acquisition strategies, *Magn Reson Mater Phy.* 19 (2006) 202–208.
- [50] T. Neuberger, A. Webb, Radiofrequency coils for magnetic resonance microscopy, *NMR Biomed.* 22 (2009) 975–981.
- [51] H. Kovacs, D. Moskau, M. Spraul, Cryogenically cooled probes—a leap in NMR technology, *Prog. Nucl. Magn. Reson. Spectrosc.* 46 (2005) 131–155.
- [52] P. Gonord, S. Kan, A. Leroy-Willig, Parallel-plate split-conductor surface coil: analysis and design, *Magn. Reson. Med.* 6 (1988) 353–358.
- [53] P. Gonord, S. Kan, A. Leroy-Willig, C. Wary, Multigap parallel-plate bracelet resonator frequency determination and applications, *Rev. Sci. Instrum.* 65 (1994) 3363–3366.
- [54] S. Serfaty, N. Haziza, L. Darrasse, S. Kan, Multi-turn split-conductor transmission-line resonators., *Magn. Reson. Med.* 38 (1997) 687–689.
- [55] DiClad Series® data sheet, (2008). <http://www.arlon-med.com/>.
- [56] S. Clare, M. Alecci, P. Jezzard, Compensating for B1 inhomogeneity using active transmit power modulation, *Magn. Reson. Imaging.* 19 (2001) 1349–1352.

- [57] W. Mao, M.B. Smith, C.M. Collins, Exploring the limits of RF shimming for high-field MRI of the human head., *Magn. Reson. Med.* 56 (2006) 918–922.
- [58] Y. Zhu, Parallel excitation with an array of transmit coils., *Magn. Reson. Med.* 51 (2004) 775–784.
- [59] C. Hayes, P. Roemer, Noise correlations in data simultaneously acquired from multiple surface coil arrays, *Magn. Reson. Med.* 16 (1990) 181–191.
- [60] A. Reykowski, S.M. Wright, J.R. Porter, Design of matching networks for low noise preamplifiers, *Magn. Reson. Med.* 33 (1995) 848–852.
- [61] W. Lee, E. Boskamp, T. Grist, K. Kurpad, Radiofrequency current source (RFCS) drive and decoupling technique for parallel transmit arrays using a high-power metal oxide semiconductor field-effect transistor (MOSFET), *Magn. Reson. Med.* 62 (2009) 218–228.
- [62] X. Chu, X. Yang, Y. Liu, J. Sabate, Y. Zhu, Ultra-low output impedance RF power amplifier for parallel excitation, *Magn. Reson. Med.* 61 (2009) 952–961.
- [63] J. Wang, A novel method to reduce the signal coupling of surface coils for MRI, in: *Proc. ISMRM*, 1996: p. 1434.
- [64] J. Jevtic, Ladder Networks for Capacitive Decoupling in Phased-Array Coils, in: *Proc. ISMRM*, 2001: p. 17.
- [65] B. Wu, P. Qu, C. Wang, J. Yuan, G.X. Shen, Interconnecting L / C Components for Decoupling and Its Application to Low-Field Open MRI Array, *Concepts Magn. Reson. Part B.* 31B(2) (2007) 116–126.
- [66] R.F. Lee, R.O. Giaquinto, C.J. Hardy, Coupling and decoupling theory and its application to the MRI phased array., *Magn. Reson. Med.* 48 (2002) 203–213.
- [67] K.M. Gilbert, A.T. Curtis, J.S. Gati, L.M. Klassen, L.E. Villemaire, R.S. Menon, Transmit/receive radiofrequency coil with individually shielded elements., *Magn. Reson. Med.* 64 (2010) 1640–1651.
- [68] H.T. Friis, Noise Figures of Radio Receivers, *Proc. IRE.* 32 (1944) 419–422.
- [69] H. Fukui, Available Power Gain, Noise Figure, and Noise Measure of Two-Ports and Their Graphical Representations, *Circuit Theory, IEEE Trans.* 13 (1966) 137–142.
- [70] J. Mispelter, M. Lupu, A. Briguet, *NMR Probeheads for Biophysical and Biomedical Experiments: Theoretical Principles and Practical Guidelines*, Imperial College Press, London, 2006.

- [71] P.L. Kuhns, M.J. Lizak, S.-H. Lee, M.S. Conradi, Inductive coupling and tuning in NMR probes; Applications, *J. Magn. Reson.* 78 (1988) 69–76.
- [72] D.I. Hoult, B. Tomanek, Use of mutually inductive coupling in probe design, *Concepts Magn. Reson.* 15 (2002) 262–285.
- [73] A. Raad, L. Darrasse, Optimization of NMR receiver bandwidth by inductive coupling., *Magn. Reson. Imaging.* 10 (1992) 55–65.
- [74] B.M. Schaller, A.W. Magill, R. Gruetter, Common modes and cable traps, in: *Proc. 11th Annu. Meet. ISMRM*, 2011: p. 4660.
- [75] E.B. Boskamp, Improved surface coil imaging in MR: decoupling of the excitation and receiver coils., *Radiology.* 157 (1985) 449–452.
- [76] M.R. Bendall, Portable NMR sample localization method using inhomogeneous RF irradiation coils, *Chem. Phys. Lett.* 99 (1983) 310–315.
- [77] anon., *The PIN Diode Circuit Designers' Handbook*, Microsemi Corporation, Watertown, MA, USA, 1998.
- [78] K.S. Yee, Numerical Solution of Initial Boundary Value Problems Involving Maxwell's Equations in Isotropic Media, *IEEE Trans. Antennas Propag.* 14 (1966) 302–307.
- [79] M.J. Turner, R.W. Clough, H.C. Martin, L.J. Topp, Stiffness and Deflection Analysis of Complex Structures, *J. Aeronaut. Sci.* 23 (1956) 805–823.
- [80] J.H. Coggon, Electromagnetic and electrical modeling by the finite element method, *Geophysics.* 36 (1971) 132–155.
- [81] R.F. Harrington, Matrix Methods for Field Problems, *Proc. IEEE.* 55 (1967) 136–149.
- [82] B.K. Li, F. Liu, E. Weber, S. Crozier, Hybrid numerical techniques for the modelling of radiofrequency coils in MRI., *NMR Biomed.* 22 (2009) 937–951.
- [83] Q. Wei, F. Liu, L. Xia, S. Crozier, An object-oriented designed finite-difference time-domain simulator for electromagnetic analysis and design in MRI - applications to high field analyses., *J. Magn. Reson.* 172 (2005) 222–230.
- [84] J.-P. Berenger, A perfectly matched layer for the absorption of electromagnetic waves, *J. Comput. Phys.* 114 (1994) 185–200.
- [85] J. Paska, J. Froehlich, D.O. Brunner, K.P. Pruessmann, R. Vahldieck, Field Superposition Method for RF coil design, in: *Proc. ISMRM*, 2009: p. 3038.



- [86] R. Zhang, Y. Xing, J. Nistler, J. Wang, Field and S-Parameter Simulation of Arbitrary Antenna Structure with Variable Lumped Elements, in: Proc. ISMRM, 2009: p. 3040.
- [87] M. Kozlov, R. Turner, Fast MRI coil analysis based on 3-D electromagnetic and RF circuit co-simulation., *J. Magn. Reson.* 200 (2009) 147–152.
- [88] S. Lambert, Modélisation, réalisation et caractérisation d'antennes supraconductrices pour la micro-IRM du cerveau de souris à 4.7 T, PhD Thesis, Université Paris-Sud 11, Orsay, France, 2011.
- [89] F.W. Grover, The Calculation of the Mutual Inductance of Circular Filaments in Any Desired Positions, *Proc. IRE.* 32 (1944) 620–629.
- [90] C. Akyel, S.I. Babic, M.-M. Mahmoudi, Mutual Inductance Calculation for Non-Coaxial Circular Air Coils With Parallel Axes, *Prog. Electromagn. Res.* 91 (2009) 287–301.
- [91] H.A. Wheeler, Transmission-Line Properties of Parallel Strips Separated by a Dielectric Sheet, *IEEE Trans. Microw. Theory Tech.* 13 (1965) 172–185.
- [92] E. Laistler, Magnetic resonance micro-imaging of the human skin in vivo using miniature radio frequency coils, PhD Thesis, Vienna University of Technology, Vienna, Austria, 2011.
- [93] S.D. Gedney, Introduction to the Finite-Difference-Time-Domain (FDTD) Method for Electromagnetics, Morgan & Claypool, USA, 2011.
- [94] L. Darrasse, G. Kassab, Quick measurement of NMR-coil sensitivity with a dual-loop probe, *Rev. Sci. Instrum.* 64 (1993) 1841–1844.
- [95] J.-C. Ginefri, E. Durand, L. Darrasse, Quick measurement of nuclear magnetic resonance coil sensitivity with a single-loop probe, *Rev. Sci. Instrum.* 70 (1999) 4730–4731.
- [96] T.S. Ibrahim, A.M. Abduljalil, B.A. Baertlein, R. Lee, P.M. Robitaille, Analysis of B1 field profiles and SAR values for multi-strut transverse electromagnetic RF coils in high field MRI applications, *Phys. Med. Biol.* 46 (2001) 2545.
- [97] R. Pohmann, K. Scheffler, A theoretical and experimental comparison of different techniques for B1 mapping at very high fields., *NMR Biomed.* 26 (2013) 265–275.
- [98] E. Insko, L. Bolinger, Mapping of the radiofrequency field, *J. Magn. Reson. A.* 103 (1993) 82–85.

- [99] G.R. Morrell, M.C. Schabel, An analysis of the accuracy of magnetic resonance flip angle measurement methods, *Phys. Med. Biol.* 55 (2010) 6157–6174.
- [100] V.L. Yarnykh, Actual flip-angle imaging in the pulsed steady state: a method for rapid three-dimensional mapping of the transmitted radiofrequency field, *Magn. Reson. Med.* 57 (2007) 192–200.
- [101] S. Chung, D. Kim, E. Breton, L. Axel, Rapid B1+ mapping using a preconditioning RF pulse with TurboFLASH readout., *Magn. Reson. Med.* 64 (2010) 439–446.
- [102] G.R. Morrell, A phase-sensitive method of flip angle mapping., *Magn. Reson. Med.* 60 (2008) 889–894.
- [103] F. Hennel, S. Koehler, M. Janich, Phase-Sensitive B1 Mapping with Adiabatic Excitation, in: *Proc. ISMRM, 2009*: p. 2610.
- [104] Y. V Chang, Rapid B1 mapping using orthogonal, equal-amplitude radio-frequency pulses., *Magn. Reson. Med.* 67 (2012) 718–723.
- [105] L.I. Sacolick, F. Wiesinger, I. Hancu, M.W. Vogel, B1 mapping by Bloch-Siegert shift., *Magn. Reson. Med.* 63 (2010) 1315–1322.
- [106] R. Kriegl, J.-C. Ginefri, M. Poirier-Quinot, L. Darrasse, S. Goluch, A. Kuehne, E. Moser, E. Laistler, Novel inductive decoupling technique for flexible transceiver arrays of monolithic transmission line resonators, *Magn. Reson. Med.* Epub (2014). doi:10.1002/mrm.25260.
- [107] R.R. Ernst, G. Bodenhausen, A. Wokaun, *Principles of Nuclear Magnetic Resonance in One and Two Dimensions*, Clarendon Press, Oxford, 1987.
- [108] E. Moser, F. Stahlberg, M.E. Ladd, S. Trattnig, 7-T MR--from research to clinical applications?, *NMR Biomed.* 25 (2012) 695–716.
- [109] E. Moser, Ultra-high-field magnetic resonance: Why and when?, *World J. Radiol.* 2 (2010) 37–40.
- [110] J.B. Kneeland, J.S. Hyde, High-resolution MR imaging with local coils., *Radiology.* 171 (1989) 1–7.
- [111] M. Woytasik, J.-C. Ginefri, J.-S. Raynaud, M. Poirier-Quinot, E. Dufour-Gergam, J.-P. Grandchamp, O. Girard, P. Robert, J.-P. Gilles, E. Martincic, L. Darrasse, Characterization of flexible RF microcoils dedicated to local MRI, *Microsyst. Technol.* 13 (2006) 1575–1580.

- [112] M. Poirier-Quinot, J.-C. Ginefri, L. Darrasse, A.-L. Coutrot, E. Dufour-Gergam, J.-P. Grandchamp, Evaluation of a Multiturn Transmission Line Resonator for Localized MR Microscopy at 1.5T, in: Proc. ISMRM, 2003: p. 2389.
- [113] N.I. Avdievich, H.P. Hetherington, 4 T Actively-Detuneable Double-Tuned  $^1\text{H}/^{31}\text{P}$  Head Volume Coil and Four-Channel  $^{31}\text{P}$  Phased Array for Human Brain Spectroscopy, *J. Magn. Reson.* 186 (2007) 341–346.
- [114] C. Constantinides, S. Angeli, Elimination of mutual inductance in NMR phased arrays: The paddle design revisited, *J. Magn. Reson.* 222 (2012) 59–67.
- [115] R. Kriegl, J.-C. Ginefri, M. Poirier-Quinot, L. Darrasse, E. Moser, E. Laistler, Inductive Decoupling of Monolithic Transmission Line Resonators, in: Proc. ESMRMB, Lisbon, Portugal, 2012: p. 348.
- [116] R. Kriegl, J.-C. Ginefri, M. Poirier-Quinot, L. Darrasse, E. Moser, E. Laistler, Mutual Decoupling for Monolithic 2D Coil Arrays – A Simulation Study, in: Proc. ESMRMB, Toulouse, France, 2013: p. 84.
- [117] I. Graesslin, H. Homann, S. Biederer, P. Börnert, K. Nehrke, P. Vernickel, G. Mens, P. Harvey, U. Katscher, A specific absorption rate prediction concept for parallel transmission MR., *Magn. Reson. Med.* 68 (2012) 1664–1674.
- [118] A. Kuehne, F. Seifert, B. Ittermann, GPU-accelerated SAR computation with arbitrary averaging shapes, in: Proc. ISMRM, Melbourne, Victoria, Australia, 2012: p. 2735.
- [119] T.G. Jurgens, A. Taflove, K. Umashankar, T.G. Moore, Finite-Difference Time-Domain Modeling of Curved Surfaces, *IEEE Trans. Antennas Propag.* 40 (1992) 357–366.
- [120] P.M. Robson, A.K. Grant, A.J. Madhuranthakam, R. Lattanzi, D.K. Sodickson, C.A. McKenzie, Comprehensive quantification of signal-to-noise ratio and g-factor for image-based and k-space-based parallel imaging reconstructions., *Magn. Reson. Med.* 60 (2008) 895–907.
- [121] F.A. Breuer, S.A.R. Kannengiesser, M. Blaimer, N. Seiberlich, P.M. Jakob, M.A. Griswold, General formulation for quantitative g-factor calculation in GRAPPA reconstructions., *Magn. Reson. Med.* 62 (2009) 739–746.
- [122] M. Weiger, K.P. Pruessmann, C. Leussler, P. Röschmann, P. Boesiger, Specific coil design for SENSE: a six-element cardiac array., *Magn. Reson. Med.* 45 (2001) 495–504.

- [123] J.A. de Zwart, P.J. Ledden, P. Kellman, P. van Gelderen, J.H. Duyn, Design of a SENSE-optimized high-sensitivity MRI receive coil for brain imaging., *Magn. Reson. Med.* 47 (2002) 1218–1227.
- [124] J. Fang, G.G. Shen, K.C. Chan, E. Gao, Q.Y. Ma, E.S. Yang, New Decoupling Method for Spiral Phased Array HTS coil, in: *Proc. ISMRM*, 2001: p. 1133.
- [125] J. Bittoun, H. Saint-Jalmes, B.G. Querleux, L. Darrasse, O. Jolivet, I.I. Peretti, M. Wartski, S.B. Richard, J.L. Leveque, In vivo high-resolution MR imaging of the skin in a whole-body system at 1.5 T, *Radiology.* 176 (1990) 457–460.
- [126] E. Laistler, M. Poirier-Quinot, S. Lambert, R.-M. Dubuisson, O.M. Girard, E. Moser, L. Darrasse, J.-C. Ginefri, In vivo MR imaging of the human skin at sub-nanoliter resolution using a superconducting surface coil at 1.5 T, *J. Magn. Reson. Imaging.* EPub (2013). doi:10.1002/jmri.24549.
- [127] J.-S. Hong, M.J. Lancaster, *Microstrip Filters for RF / Microwave Applications*, John Wiley & Sons, Inc., New York, USA, 2001.
- [128] T.S. Ibrahim, R. Lee, B.A. Baertlein, A.M. Abduljalil, H. Zhu, P.M. Robitaille, Effect of RF coil excitation on field inhomogeneity at ultra high fields: a field optimized TEM resonator., *Magn. Reson. Imaging.* 19 (2001) 1339–1347.
- [129] J.P. Mugler, J.R. Brookeman, Rapid three-dimensional T1-weighted MR imaging with the MP-RAGE sequence, *J. Magn. Reson. Imaging.* 1 (1991) 561–567.
- [130] A. Kocharian, P.J. Rossman, T.C. Hulshizer, J.P. Felmlee, S.J. Riederer, Determination of appropriate RF blocking impedance for MRI surface coils and arrays., *Magn. Reson. Mater. Physics, Biol. Med.* 10 (2000) 80–83.
- [131] R. Kriegl, M. Poirier-Quinot, L. Darrasse, E. Moser, E. Laistler, J.-C. Ginefri, Multi-turn Multi-gap Transmission Line Resonators, in: *Proc. ESMRMB*, Toulouse, France, 2013: p. 441.
- [132] D.J. Pennell, Cardiovascular magnetic resonance., *Circulation.* 121 (2010) 692–705.

# List of Figures

Figure I.1 Energy difference between spin states as function of the magnetic field strength	19
Figure I.2 $T_1$ relaxation	24
Figure I.3 $T_2$ relaxation	25
Figure I.4 Free induction decay	26
Figure I.5 Generation of a spin echo	27
Figure I.6 Spin echo train	28
Figure I.7 Generation of a gradient echo	28
Figure I.8 Slice selection	30
Figure I.9 Frequency encoding	31
Figure I.10 Image formation by phase and frequency encoding	32
Figure I.11 Spin warp sequence, pulse sequence diagram and k-space trajectory	33
Figure II.1 Basic RF coil and corresponding equivalent circuit	42
Figure II.2 Commonly used volume coils, a) solenoid, b) birdcage	47
Figure II.3 Single- and multi-turn TLR design	50
Figure II.4 Mutual decoupling by geometrical overlap	52
Figure II.5 Basic capacitive tuning and matching network	55
Figure II.7 Equivalent circuits for an inductively matched RF coil	56
Figure II.8 Inductive matching with a tuned pick-up loop	58
Figure II.10 $\lambda/2$ balun	59
Figure II.11 Three different cable trap designs	60
Figure II.12 Quarter-wavelength T/R switch	62
Figure II.13 Two-way lumped element Wilkinson power divider	63
Figure II.14 Yee cell, illustrating the offset between E- and H-field	65

Figure II.15 Two-port network.....	73
Figure III.1 Single- and double-gap TLR designs..	83
Figure III.2 Impedance matching schemes for TLRs..	85
Figure III.3 Typical $S_{11}$ response of the over-coupled system of TLR and pickup loop .....	86
Figure III.4 Annex size optimization..	94
Figure III.5 Pickup loop selection.....	95
Figure III.6 Choice of the array configuration.....	96
Figure III.7 Unaveraged SAR distributions derived from 3D EMS .....	98
Figure III.8 Coronal MR images acquired in flat array configuration.....	99
Figure III.9 Influence of mechanical flexibility on the performance of the novel TLR array	100
Figure III.10 High-resolution images of a kiwano fruit ( <i>Cucumis metuliferus</i> ).....	101
Figure IV.1 Calculated mutual inductance over distance between TLR centers .....	108
Figure IV.2 Measuring the coupling coefficient of two neighboring TLRs.....	109
Figure IV.3 Mutual inductance over distance between TLR centers-theory and experiment	111
Figure IV.4 Measured resonance frequencies $f_1$ and $f_2$ over distance between TLR centers .	112
Figure III.13 TSE image of the pepper fruit, 100 $\mu\text{m}$ in-plane resolution .....	115
Figure III.14 Photo of the sheep knee without (a) and with (b) the flexible TLR array.....	116
Figure III.15 $T_1$ weighted image of the sheep knee, 300 $\mu\text{m}$ isotropic resolution.....	117
Figure III.16 GRE image of the sheep knee, 120 $\mu\text{m}$ isotropic resolution .....	117
Figure IV.1 Capacitive network connected at the center of one conductor .....	120
Figure IV.2 Alternative feed point with capacitive matching for double-gap TLRs.....	121
Figure IV.3 Decoupling efficiency with inductive and center capacitive matching .....	121
Figure IV.4 Capacitive matching scheme for TLRs with active detuning circuit.....	123
Figure IV.5 GRE images acquired with the body coil and the TLR at 3 T.....	125

Figure IV.6 Multi-turn multi-gap TLR.....	126
Figure IV.7 Design of the MTMG TLR prototype for <sup>1</sup> H imaging at 4.7 T .....	127
Figure IV.8 Measurement conditions for the MTMG TLR prototype at 4.7 T.....	128
Figure IV.9 GRE and SNR maps obtained with the MTMG TLR prototype at 4.7 T .....	129
Figure IV.10 MTMG TLR designs (only front conductors shown) for <sup>1</sup> H imaging at 7 T...	130
Figure IV.11 Simulated current density, B <sub>1</sub> and SAR distribution for MTMG TLRs.....	133
Figure IV.12 Flip angle maps acquired with the selected MTMG TLRs.....	134
Figure V.1 Conception of a capacitively matched flexible TLR array .....	137
Figure V.2 Schematic drawing of a hexagonally arranged TLR array.....	138
Figure V.3 Concept for a MTMG TLR array .....	141
Figure A.1 Segmentation of the transmission line .....	144
Figure A.2 Index planes along the TLR.....	146
Figure A.3 Voltages and currents along the transmission line .....	147
Figure A.4 TLR seen from an external point of view .....	148
Figure A.5 Pseudo-equivalent circuit for a TLR.....	148
Figure A.6 TLR equivalent circuit with total inductance $L_{tot}$ .....	149
Figure A.7 Input parameters of the single coil macro.....	152

# List of Tables

Table I.1 Nuclei relevant for NMR and their properties .....	18
Table I.2 Representative values for $T_1$ and $T_2$ relaxation times of various tissues at 1.5 T ....	25
Table III.1 Coil Geometries, Resonance Frequencies, and Quality Factors .....	93
Table IV.1 Analytical modeling of single- and double-gap TLRs .....	113
Table V.1 Geometric parameters of the MTMG TLR prototype for $^1\text{H}$ imaging at 4.7 T ....	127
Table V.2 MTMG TLR designs for 7 T and predicted resonance frequencies .....	131
Table V.3 Measured resonance frequencies and Q-factors for the 7 T MTMG TLRs .....	132



# Publication List

## *Peer reviewed journal articles*

Kriegl, R., Ginefri, J.C., Poirier-Quinot, M., Darrasse, L., Goluch, S., Kuehne, A., Moser, E., Laistler, E., Novel inductive decoupling technique for flexible transceiver arrays of monolithic transmission line resonators. *Magn Reson Med*, 2014, doi: 10.1002/mrm.25260

Goluch, S., Kuehne, A., Meyerspeer M., Kriegl, R., Schmid A.I., Herrmann, T., Mallow, J., Hong, S.-M., Cho, Z.H., Bernading, J., Moser, E., Laistler, E., A form-fitted three channel  $^{31}\text{P}$ , two channel  $^1\text{H}$  transceive coil array for calf muscle studies at 7 T. *Magn Reson Med*, doi: 10.1002/mrm.25339

## *Conference proceedings*

Kriegl, R., Ginefri, J.C., Poirier-Quinot, M., Darrasse, L., Moser, E., Laistler, E., A flexible transceiver array of monolithic transmission line resonators. *Proc. ISMRM, Milan, Italy, 2014*, p. 1156

Kriegl, R., Ginefri, J.C., Poirier-Quinot, M., Darrasse, L., Moser, E., Laistler, E., Mutual Decoupling for Monolithic 2D Coil Arrays – A Simulation Study. *Proc. ESMRMB, Toulouse, France, 2013*, p. 84

Kriegl, R., Poirier-Quinot, M., Darrasse, L., Moser, E., Laistler, E., Ginefri, J.C., Multi-turn Multi-gap Transmission Line Resonators. *Proc. ESMRMB, Toulouse, France, 2013*, p. 441

Kriegl, R., Ginefri, J.C., Poirier-Quinot, M., Darrasse, L., Moser, E., Laistler, E., Inductive Decoupling of Monolithic Transmission Line Resonators. *Proc. ESMRMB, Lisbon, Portugal, 2012*, p. 348

Goluch, S., Kriegl, R., Moser, E., Herrmann, T., Mallow, J., Bernading, J., Kim, K.-N., Hong, S.-M., Jeong, H.-B., Cho, Z.H., Laistler, E., A multichannel  $^1\text{H}/^{31}\text{P}$  transmit-receive coil for spectroscopy in the human calf at 7T. *Proc. ESMRMB, Lisbon, Portugal, 2012*, p. 671

Kriegl R., Andreas M., Wolzt M., Moser E., Schmid A.I., Independent Component Analysis and Artefact Removal in Human Calf Muscle fMRI. *Proc. ESMRMB, Leipzig, 2011*, p. 500

Kriegl R., Andreas M., Wolzt M., Moser E., Schmid A.I. Statistische Methoden und Artefakterkennung in fMRT-Daten der menschlichen Wadenmuskulatur. Dreiländertagung Medizinische Physik, Vienna, 2011

Meyerspeer M., Kriegl R., Moser E. Creatine Methylene Group and PCr Observed by Interleaved  $^1\text{H}/^{31}\text{P}$  MRS During Muscle Exercise. *Proc. ISMRM, Stockholm, Sweden, 2010*, p. 858

# Curriculum Vitae

Roberta Kriegl, born August 5<sup>th</sup> 1988 in Mödling, Austria

## *Education*

- 10/2011 – present      Université Paris Sud, Orsay, France  
Medical University, Vienna, Austria  
PhD candidate in Medical Physics
- PhD thesis              “A flexible coil array for high resolution magnetic resonance  
imaging at 7 Tesla“
- 10/2009 – 08/2011    Technische Universität München, Munich, Germany  
Master of Science in Engineering Physics
- Master thesis            “Analysing muscle functional imaging using statistical methods”  
MR Center of Excellence, Medical University, Vienna, Austria
- 10/2006 – 07/2009    University of Technology, Vienna, Austria  
Bachelor of Science in Technical Physics
- Bachelor thesis        “Archaeometry – Thermoluminescence Dating”  
Institute of Atomic and Subatomic Physics, Vienna, Austria
- 09/1998 – 06/2006    BG/ BRG Franz Keimgasse, Mödling, Austria  
Qualification for university entrance

## *Scientific work and internships*

- 10/2014 – 12/2014    Medical University, Vienna, Austria  
Center for Medical Physics and Biomedical Engineering  
Research position related to PhD studies
- 10/2011 – 09/2014    Université Paris Sud, Orsay, France  
Research position related to PhD studies
- 07/2009 – 09/2009    Healthcare Sector, Siemens AG, Austria  
Internship at the technical department
- 07/2004                Healthcare Sector, Siemens AG, Austria  
Internship at the trading department